STUDYING CATALYSIS OF METAL NANOSTRUCTURES USING SINGLE MOLECULE FLUORESCENCE MICROSCOPY

A Dissertation

Presented to the Faculty of the Graduate School

of Cornell University

In Partial Fulfillment of the Requirements for the Degree of

Doctor of Philosophy

by

Ningmu Zou

December 2017

© 2017 Ningmu Zou

STUDYING CATALYSIS OF METAL NANOSTRUCTURES USING SINGLE MOLECULE FLUORESCENCE MICROSCOPY

Ningmu Zou, Ph. D.

Cornell University 2017

Metal nanoparticles, such as those made of Au and Ag, exhibit localized surface plasmon (SP) resonance upon excitation with visible light. These metal nanoparticles can often also act as catalysts, and many studies have shown that their SP excitation can enhance their catalytic activity. Here, by using both single-molecule super-resolution imaging and corresponding ex-situ scanning electron microscope (SEM) imaging approach, I studied the SP enhanced catalysis at sub-particle sub-diffraction level, for both linked Au-Au nanorod-nanorod and Au-Ag nanorod-nanoparticle structures. I also calculated the electric field enhancement distribution on the linked nanostructures using standard FDTD simulation packages, with geometric information of plasmonic nanocatalysts. I further quantitatively demonstrated the mechanism of catalysis hotspots is related to SP generated hot electrons.

Meanwhile, by using spatiotemporally resolved single-molecule catalysis imaging, I find that catalytic reactions on a single Pd or Au nanocatalyst can communicate with each other, similar as catalytic allostery of enzymes in which reactions occurring at different sites communicate over a distance up to a few nanometers. Presumably via hopping of positively-charged holes on the catalyst surface, over ~10^2 nanometers and with a temporal memory of ~10^1 to 10^2 seconds, this phenomenon gives rise to positive

cooperativity among its surface active sites. Catalytic communication is also present between individual nanocatalysts, but operates via a molecular diffusion mechanism involving negatively-charged product molecules, and its communication distance is many microns. Generalization of these long-range intraparticle and interparticle catalytic communications may introduce a novel conceptual framework in understanding nanoscale catalysis.

BIOGRAPHICAL SKETCH

Ningmu Zou was born on June 7th, 1989 in Zhenjiang, Jiangsu Province, China. He graduated from Wuxi No.1 High School and then obtained his Bachelor of Science degree at Nanjing University in 2011.

Ningmu came to Cornell University in July 2011 to pursue his PhD degree under the guidance of Professor Peng Chen in the area of physical chemistry, single-molecule catalysis and super-resolution imaging. There he learned how to apply single-molecule fluorescence microscopy to study catalytic behaviors on noble metal particles.

Ningmu met his wife, Zhijie Dong (Ph.D. ’15), on July 10, 2007 at Nanjing University, and they were married on July 10, 2014 at Cornell University.

ACKNOWLEDGMENTS

First and foremost, I would like to thank my advisor, Dr. Peng Chen, for his continuous guidance and encouragement throughout my doctoral program. He is the one who led me into the world of single-molecule chemistry. He has taught me how to be a good thinker, starting from exploring new research problems to determining appropriate solution methodologies, from organizing research ideas and results to presenting scientific discoveries effectively. He is always patient and rigorous to details in scientific research and this attitude has inspired me for the past six years.

My greatest appreciation also goes to my committee members, Dr. Melissa A. Hines and Dr. Richard D. Robinson, for their valuable suggestions and extensive knowledge about nanoscience. It was great to get comments and suggestions on my work from different perspectives. Meanwhile, I would also like to thank the other members of the Chen group. They have helped me many times by sharing their expertise with me. Because of them, I learned how to carefully set up and conduct single-molecule microscopy experiments and analyze vast amounts of data from them.

Special thanks go to my Ph.D. fellows and friends at Cornell University, including Guanqun Chen, Feng Yang, Hao Shen, Steven Tang, Anqi Song, Yang Gao, Lujie Huang. I will miss the times we spend together working on projects, discussing research problems, preparing for job interviews and hanging out. They have made my Ph.D. life more enjoyable and unforgettable.

Finally, I want to thank my parents, parents in law, my wife Zhijie and my son Ethan. Nothing would have been possible without the unconditional love and support from you. Thank you very much for being there forever no matter what.

TABLE OF CONTENTS

LIST OF FIGURES

LIST OF TABLES

1. INTRODUCTION

1.1. Previous studies in super-resolution fluorescence microscopy

In the study and research of biological systems and processes, microscopy plays an important role as an imaging technique. Among these microscopy techniques, fluorescence microscopy is one of the most popular tools because of its compatibility with living cells or other materials in real time. People use specific fluorescent probe molecules to label different cellular components to make them distinguishable under a fluorescence microscope. However, compared with other nanocharacterization methods such as electron microscopy, spatial resolution of conventional fluorescence microscopy is limited by the diffraction limit, which is about 200-300 nm and larger than many cellular or subcellular structures. Since Ernst Abbe discovered the spatial resolution of light microscopy is limited by diffraction in 1873, people have developed a lot of techniques to overcome this limitation during the past years. Until now, some high resolution fluorescence microscopy methods have been realized, such as I^5M and 4Pi-microscopy[1], ground-state depletion (GSD) microscopy[2-3], saturated structured-illumination microscopy (SSIM)[4-5], stimulated emission depletion (STED) microscopy[6-7], photoactivated localization microscopy (PALM)[8-12], stochastic optical reconstruction microscopy (STORM)[13-14], scanning near-field optical microscopy (SNOM)[15-16], etc.

In general, the resolution of optical microscopy is limited since light is a wave and is subject to diffraction. In an optical microscope, light rays from a point object converge to a focus at the focal plane and the rays do not converge to an exact single point. So, any sharp point on the object would blur into a finite sized spot and the three-dimensional intensity

distribution of this spot is called point spread function (PSF). The resolution of a microscope is determined by the full width at half-maximum (FWHM) of the PSF because any two points that are closer than this distance would not be resolved easily since their images overlap with each other. Figure 1.1 shows the PSF of a focused light spot using a common oil immersion objective[17].

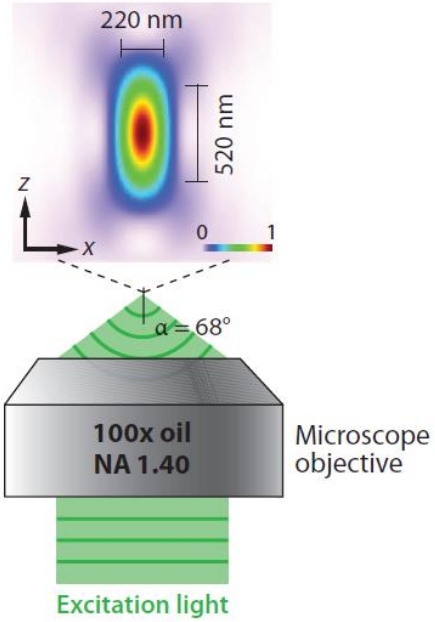

Figure 1.1. The point spread function of a common oil immersion objective with numerical aperture (NA) = 1.40, showing the focal spot of 550 nm light in a medium with a refractive index n = 1.515. The intensity distribution in the x-z plane of the focus spot is computed numerically and shown in the upper panel and the FWHM in the lateral and axial directions are 220 nm and 520 nm, respectively. Figures adapted from Huang et al.[14] Copy right 2009 Annual Reviews.

The FWHM of the PSF in the lateral directions (the x-y directions perpendicular to the optical axis) can be approximately expressed by the Rayleigh criterion:

$$\Delta xy \approx 0.61\lambda/NA \qquad \text{Eq. 1.1}$$

where λ is the wavelength of light, and NA is the numerical aperture of the objective defined

as NA = n·sin α, with n being the refractive index of the medium and α being the half-cone angle of the focused light produced by the objective. The axial width of the PSF is about 2–3 times as large as the lateral width for ordinary high NA objectives.

When we characterize or visualize some samples at the nanoscale level, the diffraction limit would substantially affect the imaging quality and become a main obstacle for characterization. Hence, improvement of the spatial resolution of light microscopy without compromising its noninvasiveness to samples is necessary. In one of super-resolution fluorescence microscopy methods, fluorescent probe molecules with two switchable states would be used. These marker fluorophores can be optically driven between the two states and one of the states is bright which can generate signals while the other state is dark. Super-resolution fluorescence microscopy is a so called "functional" super-resolution technique since it generates reconstructed images from position information of fluorophores instead of true images of sample. There are two major categories of super-resolution fluorescence microscopy: deterministic super-resolution and stochastic super-resolution microscopy. In the research of this dissertation, I mainly utilized stochastic super-resolution microscopy technique base on photoactivated localization microscopy (PALM) and stochastic optical reconstruction microscopy (STORM).

In principle, the position of a molecule is determined by its coordinates in 2D or 3D space. If we achieve coordinates for every single molecule, we could reconstruct an image of sample with very high precision. Since the mid-1990s, people have started to research single-molecule microscopy.[18-20] Now, fluorescent probe molecules are commercially available and a set of single-molecule methods have been well developed.[21] For typical fluorescent microscopy, fluorescence emission from all fluorophores will overlap severely

so that the overall image appears as a completely featureless blur. However, the single-molecule super-resolution microscopy controls the emission from fluorophores such that only one molecule is emitting at a time within a diffraction-limited area. Then, individual molecules can then be imaged and localized. This method is applied by all of stochastic single-molecule super-resolution microscopy, such as PALM[8-12], and STORM[13].

PALM and FPALM were developed through fluorescent proteins (photoactivatable GFP, YFP or tandem dimer Eos) as the switchable probes. To control the number of emissive fluorophores, the activation light of a sufficiently low intensity is applied to the sample so that only a sparse, random subset of fluorophores is activated to the bright state at any time, allowing these molecules to be imaged individually, localized, and then deactivated by switching to a reversible dark state or permanent photobleached state. By doing this iteration for many times, a reconstructed image can be obtained and lateral resolution can reach ~10nm[11].

In STORM, fluorescence image is reconstructed from high-accuracy localizations of individual fluorescent molecules which are switched between on and off states using light of different colors. The imaging process consists of a series of imaging cycles (Figure 1.2A). In each cycle, only a fraction of the fluorophores in the field of view are switched on, such that each of the active fluorophores is optically resolvable from the rest, that is, their images are not overlapping[13]. Different from PALM, STORM method needs a pair of conjugated fluorophores, such as Cy3 and Cy5, and the distance between which would affect the switching time as well as time resolution. By labeling different proteins with different fluorophore pairs, people can spatially localize all of proteins in one experiment and the lateral axial resolution can reach ~20-30 nm (Figure 1.2 B)[22] . The disadvantage of STORM

is that it cannot be used to quantify the number of proteins since every protein is multi-labeled with fluorophore pairs.

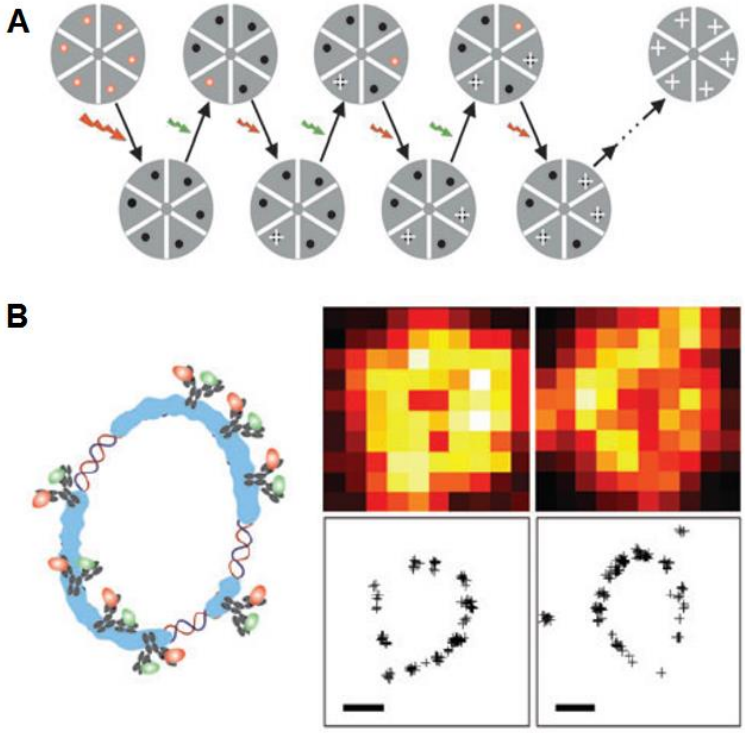

Figure 1.2. Scheme of STORM. (a) STORM imaging sequence using an object labeled with red fluorophores that can be switched between a fluorescent and a dark state by a red and green laser, respectively. (b) STORM images of a DNA. Images with switch-labeled antibody taken by a total internal reflection microscope (top); the reconstructed STORM images of the same filaments (bottom). Figures adapted from Bates et al.[22] Copy right 2007 American Association for the Advancement of Science. Similar with PALM, in 2D plane, the PSF can be fit as a 2D Gaussian function,

$$I(x,y) = A\exp\left(-\frac{(x-x_0)^2}{2\sigma_x^2}-\frac{(y-y_0)^2}{2\sigma_y^2}\right)+Bx+Cy+D \qquad \text{Eq. 1.2}$$

here I(x,y) is the fluorescence intensity counts, x_0, y_0 is the center position, σ_x, σ_y is the standard deviation in x and y direction. Also, the background linear tilt needs to be taken

into consideration. This 2D Gaussian function would be utilized in this dissertation for many times.

The last decade has witnessed the rapid pace of development of all kinds of super-resolution imaging techniques. Images and videos obtained from these new methods would provide us with unprecedented knowledge about molecular interactions and dynamic processes in chemistry, material science and biology. Besides the improvements of microscopy techniques, new fluorescent probes and labeling chemistry are also important for increasing resolution. These efforts would allow the truly molecular scale resolution by optical microscopy. Due to limited space of this dissertation, I just made a brief introduction on this topic by choosing the most relevant super-resolution imaging techniques.

1.2. Super-resolution fluorescence microscopy for nanoparticle catalysis

Measurement of single nanoparticle catalytic activity requires ultrasensitive detection of the product molecules, as only a few product molecules may be generated by a single nanoparticle during a limited time. To achieve the detection and localization of single-molecule reactions, some fluorogenic catalytic reactions are studied, in which a nonfluorescent reactant molecule is converted to a highly fluorescent product molecule on a nanoparticle catalyst. Each product molecule can emit thousands of photons under illumination, enabling the single-molecule detection with an electron-multiplying CCD camera. By fitting the fluorescence point spread function with a 2D Gaussian function and localizing the fluorescent product molecules one at a time, people can image product generation with a spatial resolution of tens of nanometers.

One of the first studies in spatially resolved catalytic activity was done by Hofkens

and his coworkers on the micrometer-sized layered double hydroxide (LDH) catalyst.[23] In this study, non-fluorescent 5-carboxyfluoresce in diacetate (C-FDA) was catalyzed by LDH to generate a fluorescent molecule. By examining the catalytic activity on different facets of the microcatalysts, they demonstrated the catalysis mechanism on each facet (Figure 1.3A). Majima et al. also studied photocatalysis reactions on TiO_2 nanocrystals by imaging reactive oxygen species generated on TiO_2 nanocrystals at the single-molecule level (Figure 1.3C).[24] They studied the facet-specific charge carrier generation by only exciting some specific facets (such as (001) facet), which can illustrate the relationship between facet-specific electron trapping and transport.[25] Chen et al. used super-resolution technique to observe the localized reaction sites on carbon nanotubes,[26] and the activity distribution on metal[27-28] and semiconductor nanocatalysts.[29] In pseudo-1D material such as Au nanorods, a linear gradient catalytic activity along the length of its side facets was observed. The catalytic activity gradually decays from the middle of the nanorod towards its two ends (Figure 1.3B). In pseudo-2D material such as Au nanoplates, the catalytic activity was observed to gradually decay from the center of the nanoparticle towards its periphery. In photocatalysts such as TiO_2 nanorods, they mapped both the electron- and hole-driven photoelectrocatalytic activities on single nanoparticles and associated the localized photocurrent with water oxidation. They found that the most active sites for water oxidation are also the most important sites for charge-carrier recombination.

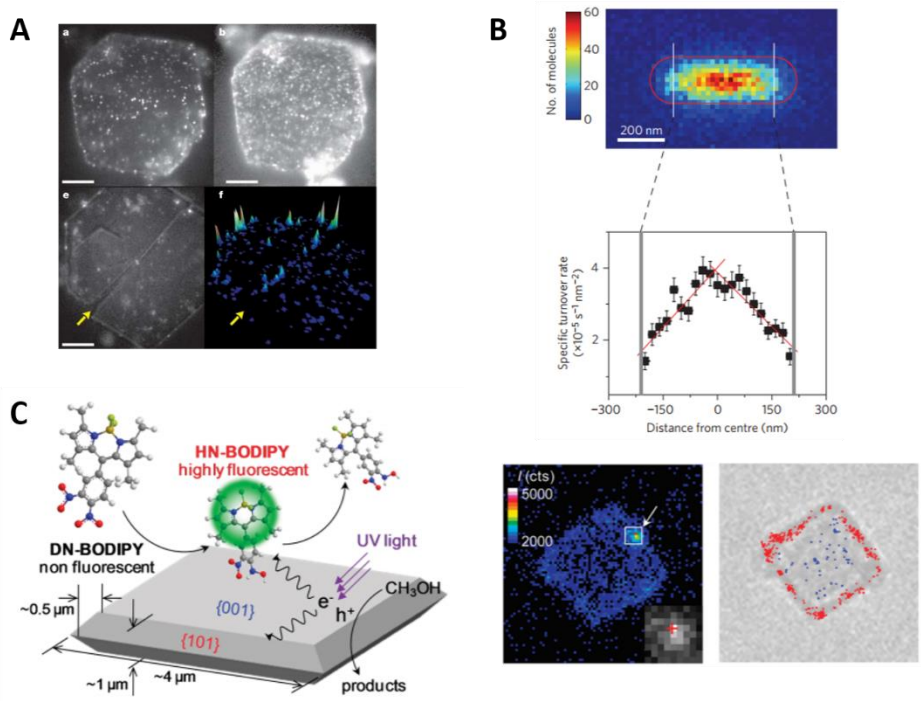

Figure 1.3. Spatially resolved activity distribution. (**A**) Single LDH catalyzed transesterification of C-FDA with 700 nM 1-butanol, adapted from Roeffaers.[23] Copy right 2006 Nature Publishing Group. (**B**) 2-D histogram of catalytic product locations on a single Au@mSiO2 nanorod in catalyzing a N-deacetylation reaction and dependence of the specific turnover rate on location at every ~20 nm segment along the length of the same nanorod.[27] The red line is the SEM structural contour of the nanorod. The write lines separate out the two ends. Copy right 2012 Nature Publishing Group. (**C**) Photocatalytic generation of fluorescent HN-BODIPY from nonfluorescent DN-BODIPY over a TiO_2 crystal and corresponding fluorescence and transmission images of a TiO_2 crystal immobilized on a cover glass in Ar-saturated methanol solution containing DN-BODIPY (2.0 μM) under a 488 nm laser and UV irradiation.[24] Copy right 2011 American Chemical Society.

Super-resolution fluorescence microscopy allows for real-time, single-turnover observations of catalytic reactions on a wide range of catalyst materials under ambient conditions. Using single molecule super-resolution imaging, one can localize the position of a fluorescent molecule down to even sub-nanometer precision.[30] This technique also allows

3-D localization of single molecules with precision down to nanometer.[31] Meanwhile, it also can be integrated into other nano-characterization methods, such as electron microscopy,[27-28] atomic force microscopy,[32] Raman spectroscopy,[33-34] electrochemistry,[29, 35] etc. Meanwhile, catalytic reactions without involving fluorescent molecules, such as those in fuel cells, batteries, cannot be studied directly by single molecule fluorescence microscopy. To overcome this challenge, one can use fluorogenic reactions to study chemical reactions.[36] People can also use indirect detection, which employs a subsequent fluorogenic reaction to detect non-fluorescent products in an initial reaction of interest.[37] Moreover, we discovered the activity correlations between different reactions occurring on the same catalysts; therefore, results from fluorogenic reactions can be extrapolated to more general, non-fluorogenic reactions.[38]

1.3. Scope of this dissertation

This dissertation focuses on studying the heterogeneous catalysis using single molecule fluorescence microscopy. We utilize its advantages in high-temporal, high-spatial resolution and correlate the catalytic activity with surface plasmon and catalytic communication.

In Chapter 2 and 3 of this thesis, I report a direct visualization of the activity enhancement at nanoscale gaps between two plasmonic nanoparticles (Au nanorod or Ag nanoparticle), using single-molecule super-resolution catalysis imaging in correlation with electron microscopy. Surface plasmon enhanced catalysis is promising in harvesting light to drive chemical reactions that were otherwise inefficient or to bias the reaction pathways toward more desirable products. Catalytic hotspots at plasmonic hotspots is long predicted,

but experimentally observing it has been challenging, even though it is crucial for understanding the enhancement mechanism. Here, I define the correlations of the enhancement with the nanostructure geometry and local electric field enhancement, and show that the enhancement scales quadratically with the local actual light intensity, reflecting the involvement of plasmon-excitation induced hot electrons in the catalytic enhancement mechanism. This study demonstrates a methodology of applying correlated super-resolution microscopy and electron microscopy to study plasmonic nanocatalysts at the sub-particle level. The results reveal the intimate relation between the activity increase of metal nanocatalysts and local surface plasmon enhancement, demonstrating a long-predicted but hard-to-observe phenomenon in plasmon-enhanced catalysis.

In Chapter 4 and 5 of this thesis, I report both intraparticle and interparticle catalytic communication by analyzing the correlation between temporally subsequent reactions occurring at different locations within and among single nanocatalysts, resolved spatiotemporally using single-molecule fluorescence localization microscopy. This catalytic communication phenomenon, a first-of-its-kind discovery, occurs in three Pd or Au based nanocatalysts and in three distinct catalytic reactions including a photo-induced disproportionation reaction, an oxidative deacetylation reaction, and a reductive deoxygenation reaction. As the catalytic communications are phenomenologically similar and conceptually analogous to synergism in enzymes, which are nature's most efficient catalysts, I envision that exploration of their generality and utility may bring new theoretical framework in understanding nanocatalysis.

This catalytic communication project was completed by team work: I, Xiaochun Zhou, Guanqun Chen, and Nesha May Andoy performed the research and analyzed the data

with my advisor. Won Jung and Guokun Liu contributed to the research as well. I sincerely appreciate their professional knowledge and contribution.

REFERENCES

1. Bewersdorf, J.; Schmidt, R.; Hell, S. W., *Journal of Microscopy* **2006,** *222*, 105-117.

2. Hell, S. W.; Kroug, M., *Appl. Phys. B* **1995,** *60*, 495-497.

3. Bretschneider, S.; Eggeling, C.; Hell, S. W., *Physical Review Letters* **2007,** *98*, 218103.

4. Gustafsson, M. G. L., *Proceedings of the National Academy of Sciences of the United States of America* **2005,** *102*, 13081-13086.

5. Heintzmann, R.; Jovin, T. M.; Cremer, C., *Journal of the Optical Society of America a-Optics Image Science and Vision* **2002,** *19*, 1599-1609.

6. Hell, S. W.; Wichmann, J., *Optics Letters* **1994,** *19*, 780-782.

7. Willig, K. I.; Rizzoli, S. O.; Westphal, V.; Jahn, R.; Hell, S. W., *Nature* **2006,** *440*, 935-939.

8. Fernandez-Suarez, M.; Ting, A. Y., *Nature Reviews Molecular Cell Biology* **2008,** *9*, 929-943.

9. Manley, S.; Gillette, J. M.; Patterson, G. H.; Shroff, H.; Hess, H. F.; Betzig, E.; Lippincott-Schwartz, J., *Nature Methods* **2008,** *5*, 155-157.

10. Betzig, E.; Patterson, G. H.; Sougrat, R.; Lindwasser, O. W.; Olenych, S.; Bonifacino, J. S.; Davidson, M. W.; Lippincott-Schwartz, J.; Hess, H. F., *Science* **2006,** *313*, 1642-1645.

11. Shroff, H.; Galbraith, C. G.; Galbraith, J. A.; Betzig, E., *Nature Methods* **2008,** *5*, 417-423.

12. Hess, S. T.; Girirajan, T. P. K.; Mason, M. D., *Biophysical Journal* **2006,** *91*, 4258-4272.

13. Rust, M. J.; Bates, M.; Zhuang, X., *Nature Methods* **2006,** *3*, 793-795.

14. Huang, B.; Wang, W.; Bates, M.; Zhuang, X., *Science* **2008,** *319*, 810-813.

15. Betzig, E.; Trautman, J. K.; Harris, T. D.; Weiner, J. S.; Kostelak, R. L., *Science* **1991,** *251*, 1468-1470.

16. Betzig, E.; Trautman, J. K., *Science* **1992,** *257*, 189-195.

17. Huang, B.; Bates, M.; Zhuang, X., Super-Resolution Fluorescence Microscopy. In *Annual Review of Biochemistry*, 2009; Vol. 78, pp 993-1016.

18. Betzig, E.; Chichester, R. J., *Science* **1993,** *262*, 1422-1425.

19. Xie, X. S., *Accounts of Chemical Research* **1996,** *29*, 598-606.

20. Nie, S.; Chiu, D.; Zare, R., *Science* **1994,** *266*, 1018-1021.

21. Moerner, W. E., *Proceedings of the National Academy of Sciences* **2007,** *104*, 12596-12602.

22. Bates, M.; Huang, B.; Dempsey, G. T.; Zhuang, X., *Science* **2007,** *317*, 1749-1753.

23. Roeffaers, M. B. J.; Sels, B. F.; Uji-i, H.; De Schryver, F. C.; Jacobs, P. A.; De Vos, D. E.; Hofkens, J., *Nature* **2006,** *439*, 572-575.

24. Tachikawa, T.; Yamashita, S.; Majima, T., *Journal of the American Chemical Society* **2011,** *133*, 7197-7204.

25. Wang, N.; Tachikawa, T.; Majima, T., *Chemical Science* **2011,** *2*, 891-900.

26. Xu, W.; Shen, H.; Kim, Y. J.; Zhou, X.; Liu, G.; Park, J.; Chen, P., *Nano Letters* **2009,** *9*, 3968-3973.

27. Zhou, X.; Andoy, N. M.; Liu, G.; Choudhary, E.; Han, K.-S.; Shen, H.; Chen, P., *Nat Nano* **2012,** *7*, 237-241.

28. Andoy, N. M.; Zhou, X.; Choudhary, E.; Shen, H.; Liu, G.; Chen, P., *Journal of the American Chemical Society* **2013,** *135*, 1845-1852.

29. Sambur, J. B.; Chen, T.-Y.; Choudhary, E.; Chen, G.; Nissen, E. J.; Thomas, E. M.; Zou, N.; Chen, P., *Nature* **2016,** *530*, 77-80.

30. Pertsinidis, A.; Zhang, Y.; Chu, S., *Nature* **2010,** *466*, 647-651.

31. Huang, B.; Wang, W.; Bates, M.; Zhuang, X., *Science* **2008,** *319*, 810.

32. Harvey, C. E.; van Schrojenstein Lantman, E. M.; Mank, A. J. G.; Weckhuysen, B. M., *Chemical Communications* **2012,** *48*, 1742-1744.

33. Zhang, R.; Zhang, Y.; Dong, Z. C.; Jiang, S.; Zhang, C.; Chen, L. G.; Zhang, L.; Liao, Y.; Aizpurua, J.; Luo, Y.; Yang, J. L.; Hou, J. G., *Nature* **2013,** *498*, 82-86.

34. Willets, K. A.; Stranahan, S. M.; Weber, M. L., *The Journal of Physical Chemistry Letters* **2012,** *3*, 1286-1294.

35. Guerrette, J. P.; Percival, S. J.; Zhang, B., *Journal of the American Chemical Society* **2013,** *135*, 855-861.

36. Tachikawa, T.; Wang , N.; Yamashita, S.; Cui, S.-C.; Majima, T., *Angewandte Chemie International Edition* **2010,** *49*, 8593-8597.

37. Naito, K.; Tachikawa, T.; Fujitsuka, M.; Majima, T., *The Journal of Physical Chemistry B* **2005,** *109*, 23138-23140.

38. Zhou, X.; Choudhary, E.; Andoy, N. M.; Zou, N.; Chen, P., *ACS Catalysis* **2013,** *3*, 1448-1453.

2. IMAGING CATALYTIC HOTSPOTS ON SINGLE PLASMONIC NANOSTRUCTURES VIA CORRELATED SUPER-RESOLUTION AND ELECTRON MICROSCOPY

2.1. INTRODUCTION

Metal nanoparticles, such as those made of Au and Ag, exhibit localized surface plasmon (SP) resonance upon excitation with visible light, in which the collective oscillations of the metal valence electrons generate an intense oscillating electric field within a few nanometers to the nanoparticle surface.[1-5] These metal nanoparticles can often also act as catalysts,[6-12] and many studies have shown that their SP excitation can enhance their catalytic activity, for example in Ag nanoparticle catalyzed CO oxidation,[10] decomposition of organic molecules,[11] and catalytic coupling reactions.[12] This SP-enhanced catalysis opens new opportunities to harvest light to drive catalytic reactions that are otherwise inefficient or to bias the reaction pathways toward more desirable products.[6,7]

The promise of SP-enhanced catalysis motivated many studies into understanding the underlying mechanisms of catalytic enhancement. Several mechanisms can operate on plasmonic metal nanoparticles. One obvious possible mechanism is the thermal effect, in which the enhanced light absorption by plasmonic nanoparticles converts into heat to drive thermally activated reactions on the nanoparticle surface.[13-15] A second mechanism is enhanced photoexcitation of the reactant molecules, if they are able to absorb light in the wavelength range where the SP resonance occurs; the intense local electric field on the plasmonic nanoparticle surfaces can thus enhance the photoexcitation of the reactant molecules, leading to more efficient photochemical reactions.[16] A third mechanism involves

hot electrons generated from SP excitation; these hot electrons could be injected into the surface adsorbed molecules, driving subsequent chemical transformations.[8,10,17-19]

In probing the mechanisms of SP-enhanced catalysis, ensemble-level measurements have been instrumental,[10,20-23] in which the collective catalytic behaviors of a large number of plasmonic nanoparticles are measured, for example, as a function of light intensity,[10] light wavelength,[20] or temperature.[21,22] Photoluminescence spectroscopy of the metal nanoparticles has also been used to probe indirectly SP-enhanced catalysis, even down to the single-particle level, but the catalytic activity there was still measured at the ensemble level.[23] Although powerful, these ensemble measurements have limitations imposed by the intrinsic heterogeneity of plasmonic nanostructures. First, the electric field enhancement is spatially heterogeneous across a plasmonic particle. Depending on the particle shape, the enhancement could be much larger at particular locations of nanometers in dimension, so-called plasmonic "hotspots" (e.g., corners or crevices), than other locations[3]—even for a pseudospherical particle, the electric field enhancement distribution is dependent on the polarization of the excitation light. Second, plasmonic hotspots often exist at nanoscale gaps between plasmonic particles;[24] these gaps are few and occur irregularly within a cluster of particles, but they could be dominant contributors to the enhanced catalytic activity measured at the ensemble level.

The spatial heterogeneity of plasmonic enhancements also predicts different spatial patterns of catalytic enhancements on plasmonic nanostructures, depending on the underlying mechanism. For the thermal effect, as plasmonic metals have large thermal conductivity, the heat generated from SP excitation would quickly dissipate, resulting in a spatial uniformity of the corresponding catalytic enhancement over any single nanostructure.

On the other hand, both the enhanced photoexcitation effect and the hot electron effect depend on the local electric field intensity; a spatially heterogeneous electric field enhancement would lead to spatial heterogeneity in the corresponding catalytic enhancement, forming nanoscale catalytic hotspots at plasmonic hotspots.

A number of spatially selective approaches have been used to exploit this spatial heterogeneity to observe catalytic reactions at plasmonic hotspots.[25-34] Single-molecule surface-enhanced Raman spectroscopy (SERS) and tip-enhanced Raman spectroscopy (TERS) have been used to image redox reactions on single gold and silver colloidal particles,[25,27] on bulk metal surfaces,[26] and on particle aggregates[28-30] down to sub-diffraction-limited resolution. However, the colloidal aggregates are hard to control geometrically; the approaches only apply to SERS-active molecules; and the extent of local catalytic enhancements is not directly quantifiable because the reaction rates at plasmonic hotspots cannot be compared with those at non-plasmonic hotspots, where the SERS signals are undetectable. Atomic force microscopy (AFM)[31] and scanning electron microscope (SEM)[32,33] have been used to image polymerization reaction products on plasmonic nanostructures, but the measurements are ex situ, on dry samples, and do not provide quantitative reaction kinetics.

Single-molecule super-resolution fluorescence microscopy has been shown to be a complementary and powerful approach to study catalysis on nanoscale particles.[35-47] With its single-molecule sensitivity and nanometer spatial resolution, catalytic and (photo)(electro)catalytic reactions on individual metal nanoparticles,[5,35,38,45,48-50] zeolite particles,[37] semiconductor particles,[39-42,51] and carbon nanomaterials[43,44] can be imaged and quantified under operando conditions in real time with singe-turnover resolution. Here we

use single-molecule super-resolution fluorescence imaging combined with electron microscopy to study SP-enhanced catalysis on two linked nanostructures that present plasmonic hotspots at nanoscale gaps. We directly observe and quantify the catalytic enhancements at these nanoscale plasmonic hotspots (a first-of-its-kind experimental achievement), define their correlations with the nanostructure geometry and local electric field enhancement, and show that the enhancement scales quadratically with the local actual light intensity, reflecting the involvement of plasmon-excitation induced hot electrons in the catalytic enhancement mechanism.

2.2. MATERIALS AND METHODS

Details of materials and methods are described in the Supporting Information (SI; Chapter 3). Au nanorod synthesis was based on previous work with some modification.[38] Ag nanoparticles were purchased from Ted Pella. The linked Au-Au nanorod-nanorod and Au-Ag nanorod-nanoparticle nanostructures were prepared using a biotin-streptavidin linkage strategy,[52] and then coated with mesoporous silica shell as previously reported,[38,48] after which the organic ligands were removed via UV-ozone treatment.[48] SEM was done on a LEO 1550VP FESEM operated at 10~15 keV. EDX was done using a Bruker Quantax x-ray detector attached to the SEM. Catalysis on plasmonic nanostructures was imaged using single-molecule total internal reflection fluorescence (TIRF) microscopy based on an Olympus IX71 microscope as previously described.[38,48,53] All single-molecule image processing was done via home-written MATLAB codes.[38] FDTD simulations were done using FDTD Solutions from Lumerical Solutions, Inc.

2.3. RESULTS AND ANALYSIS

2.3.1. Au-Au and Au-Ag nanostructures with plasmonic hotspots.

We chose to make two Au- and Ag-based nanostructures with nanoscale gaps where high plasmonic enhancement is expected. One such plasmonic nanostructure is linked Au-Au nanorods with ~8 nm long spacers of biotin-streptavidin linkages, following the method of Murphy et al[52] (SI Section 3.1). We chose these Au nanorods for their high structural anisotropy (~21 nm in diameter and hundreds of nm in length; SI Figure 3.1) as well as for their visible wavelength localized SP resonance (the transverse mode peaks at ~515 nm;[54,55] SI Figure 3.2J). We further coated these linked Au-Au nanorods with a ~70 nm thick mesoporous silica shell (i.e., mSiO2) to stabilize the linked geometry. This shell also allowed for subsequent UV-ozone treatment to remove the organic components while preventing aggregation; the mesopores still allow the reactants to access the metal surface for catalysis without mass transport limitation, as we previous showed[38,48,49]. SEM images of such linked Au-Au nanorods reveal variations of linkage geometries: V-shaped (e.g., Figure 2.1A, C) and T-shaped (e.g., Figure 2.1B) with variable angles in between. The nanoscale gaps are clearly visible; their sizes are readily determined via line profile analysis of the SEM images and are about 8.8 ± 2.2 nm (Figure 2.1D, E), consistent with the expected dimension of the original biotin-streptavidin linkages used in the synthesis (SI Section 3.1.4).

The second plasmonic nanostructure is Au nanorods linked to ~50 nm Ag nanoparticles with nanoscale gaps, using the same biotin-streptavidin linkage method and also encapsulated in a $mSiO_2$ shell (Figure 2.1F-H; SI Section 2.1.2). Ag nanoparticles here provide localized SP resonance at a different visible wavelength region (~415 nm;[56] SI

Figure 3.2I). The Ag nanoparticle could be located on the side of a Au nanorod (e.g., Figure 2.1F, G) or near its end (e.g., Figure 2.1H). The gaps are about 8.2 ± 2.1 nm in size (Figure 2.1I, J).

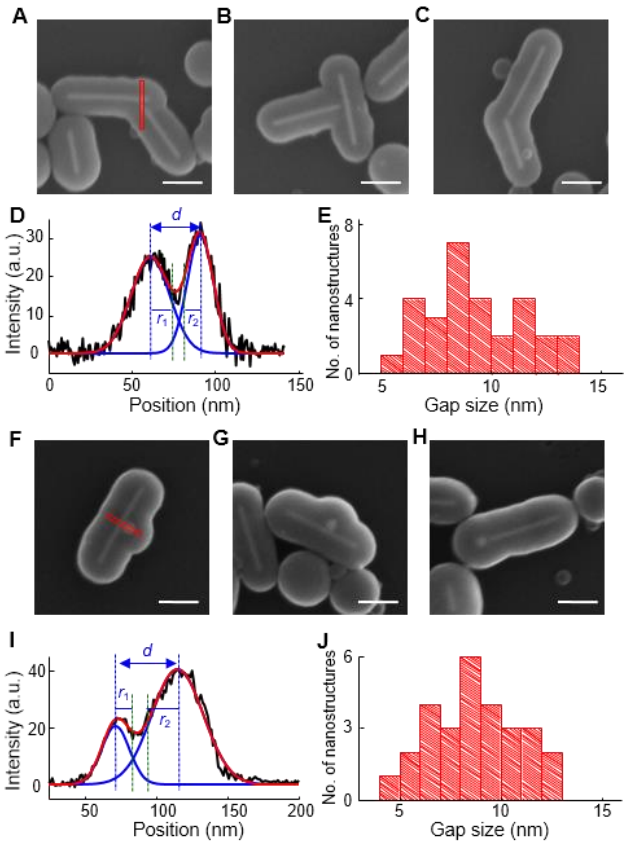

Figure 2.1. Linked plasmonic nanostructures. (**A-C**) SEM images of exemplary linked Au-Au nanorods encapsulated in $mSiO_2$. All scale bars are 200 nm. (**D**) Line profile analysis of the red box on the linked Au-Au nanorods in A. Gap size is defined as $d - r_1 - r_2$, where r is the radius of the nanorod/nanoparticle, determined from the FWHM of the Gaussian fit of the line profile, and d is the center-to-center distance between the nanorods/nanoparticles. Blue lines: Gaussian deconvolution; red line: overall fit. (**E**) Gap size distribution of linked Au-Au nanorods; average is 8.8 ± 2.2 nm. (**F-J**) Same as A-E, but for linked Au-Ag nanorod-nanoparticle encapsulated in $mSiO_2$. Average gap size is 8.2 ± 2.1 nm.

2.3.2. Super-resolution imaging of catalytic hotspots on linked Au-Au nanorods in correlation with SEM.

Using single-molecule super-resolution fluorescence microscopy[38,48] (SI Section 3.2.1), we imaged and localized individual fluorescent catalytic product molecules on single Au-Au nanorod structures with ~40 nm precision (Figure 2.2A). These nanostructures were immobilized on a quartz slide in a microfluidic reactor cell, into which the reactants were supplied continuously to achieve steady state kinetics (SI Section 3.2.1). The catalytic reaction here is a fluorogenic reaction in buffered pH 7.1 aqueous solution: the reductive deoxygenation of resazurin by NH_2OH to generate resorufin, a highly fluorescent molecule. We have previously shown[53] that: (1) this Au particle catalyzed reaction follows the classic Langmuir–Hinshelwood kinetics; (2) at a large excess of NH_2OH (e.g., 20 mM), the catalytic rate is initially first order to the resazurin concentration and then saturates to zeroth order when the resazurin concentration reaches ~0.2 μM (also Figure 2.7B later); and (3) the fluorescence of the product resorufin is imaged while it is temporarily adsorbed within the mesopores of the $mSiO_2$ shell rather than on the metal surface (as its desorption off the Au nanorod surface is fast), before it desorbs and disappears into the surrounding solution. Moreover, during our experimental imaging time of ~6 hours, the catalytic activities of these linked Au-Au nanorods stayed stable (SI Figure 3.9).

We further performed ex situ SEM on the same nanostructures, subsequent to our fluorescence imaging experiment (Figure 2.2B). Correlating the SEM image with the fluorescence images allowed us to map the positions of fluorescent catalytic products onto the structural contours of individual linked Au-Au nanorod structures with nanometer

precision (Figure 2.2A; SI Section 3.4). The correlated images immediately reveal an enhanced catalytic activity at the gap region of linked Au-Au nanorod nanostructures, where the plasmonic enhancement is high. For the linked nanostructure in Figure 2.2A-B with a ~9 nm gap (Figure 2.2E), the detected number of catalytic products at the gap region (red circle) is ~2.5 times more than those detected at the non-gap regions of the two linked nanorods (two black circles) (Figure 2.2A), representing a first-of-its-kind, quantitative, visualization of SP-enhanced catalysis at the nanoscale.

Control measurements indicated that: (1) The higher detection rate of catalytic products at the gap region is not due to their enhanced fluorescence intensities there, because their fluorescence intensities do not show significant differences at the gap vs. non-gap regions (Figure 2.2C and SI Figure 3.11). The absence of fluorescence enhancement at the gap region is consistent with that the product is detected while trapped in the $mSiO_2$ shell rather than directly on the Au surface, where the electric field enhancement is localized. (2) It is not because the products stay adsorbed longer at the gap region, as the average residence time of individual products are the same at gap vs. non-gap regions (Figure 2.2D and SI Figure 3.11). (3) It is not due to higher reactant access at the gap region because our reaction condition is pseudo-zeroth order to reactant concentration and resorufin re-binding control shows similar adsorption frequencies at gap vs. non-gap regions (SI Section 3.5.2). Furthermore, FDTD simulations showed that possible coupling between the product fluorescence and the nanostructure plasmon only shifts the apparent product position by less than ~20 nm, smaller than our localization precision of ~40 nm (SI Section 3.6.3).

To quantify the catalytic enhancement, we computed the specific turnover rate (i.e., catalytic activity) within a circular region centered at the gap in comparison with that at non-gap regions (red vs. black circles, Figure 2.2A, B; and SI Section 3.7). The typical circle radius is 70 nm, significantly larger than our spatial resolution of ~40 nm. We also varied the circle radius to 40 and 100 nm; the conclusions presented below stay the same (SI Figure 3.11D, J). Pooling results from 31 linked Au-Au nanorods illuminated by an average power density of 1.27 kW cm^{-2} at 532 nm, we observed that the catalytic activity at the gap regions are always higher than the non-gap regions, by ~1.9 times on average and up to ~3.1 times at the single nanostructure level (Figure 2.2F and H). These localized catalytic activity enhancements clearly demonstrate the catalytic hotspots on these linked plasmonic nanostructures.

To quantitatively connect the catalytic enhancement with the local plasmonic enhancement at the gap region, we performed 2-dimensional FDTD simulations to calculate the local electric field enhancement patterns (SI Section 3.6.1). For each linked Au-Au nanorod structure, we used its experimentally determined geometry, nanorod dimension, and gap size, as well as the excitation light wavelength (532 nm), polarization, and *k*-vector direction. Figure 2.2G shows the simulated electric field intensity pattern for the nanostructure in Figure 2.2A. A strong electric field enhancement is clear at the gap region, as expected. We further determined the average electric field enhancement (i.e., $|E|^2/|E_0|^2$) within the same circles at the gap vs. non-gap regions, as we did in calculating their catalytic activities. We only considered the electric field enhancement within 3 nm of the Au surface, as the catalytic reactions occur at the surface and the reactant molecules are ~1 nm in size (SI Section 3.6.1). For the gap vs. non-gap regions of the 31 linked Au-Au nanostructures,

their electric field enhancement ratios are directly correlated with their catalytic activity ratios (Pearson's correlation coefficient $\rho = 0.76 \pm 0.05$, Figure 2.2H), directly supporting that the catalytic enhancement at the gap region arises from local electric field enhancement.

Taken altogether, the above results demonstrate the direct visualization of catalytic hotspots at plasmonic hotspots on these linked Au-Au nanorod structures. These localized catalytic hotspots within a single nanostructure also immediately rules out thermal effect as an underlying cause for the catalytic enhancement, as the high thermal conductivity of Au would give a homogeneous temperature distribution within a single nanostructure without temperature hotspots (SI Section 3.5.3).

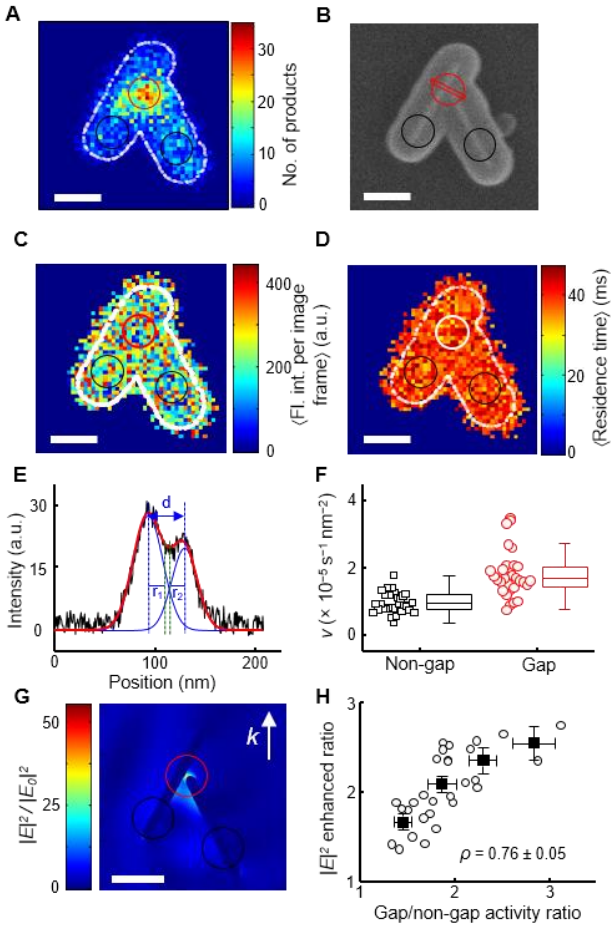

Figure 2.2. Catalytic hotspots on linked Au-Au nanorod nanostructure. (**A**) Quantitative super-

resolution mapping of catalytic products on a nanostructure. White line: structural contour of the nanostructure from its SEM image in B. (**B**) SEM image of linked Au-Au nanorod encapsulated in $mSiO_2$ in A. The red and black circles (70 nm radius) define the gap and non-gap regions. (**C**) Spatial distribution of the average single-molecule fluorescence intensity of the catalytic product resorufin per image frame (30 ms) on the nanostructure in A. ⟨ ⟩ denotes averaging. (**D**) Spatial distribution of the average residence time of the catalytic product on the nanostructure in A. (**E**) Gap size determination via line profiling of the SEM image in B (red box). The gap here is 5.8 ± 0.9 nm. (**F**) Box plot of specific turnover rate v of gap vs. non-gap regions on 31 linked Au-Au nanorods, showing the median, first and third quantile, and interquartile range. (**G**) FDTD simulation of electric field enhancement pattern on the nanostructure in A at 532 nm. (**H**) Correlation between electric field enhancement ratios of gap vs. non-gap regions and their catalytic activity ratios. Each black open circle is one nanostructure. Solid black squares: binned and averaged results. All scale bars represent 200 nm. x, y error bars are s.d.

2.3.3. Super-resolution imaging of catalytic hotspots on linked Au-Ag nanostructures in correlation with SEM.

Using correlated single-molecule super-resolution fluorescence microscopy and SEM, we also studied linked Au-Ag nanorod-nanoparticle nanostructures in catalyzing the same reductive deoxygenation reaction of resazurin. Here, the Ag nanoparticles are not catalytically active, as shown by ensemble activity measurements; they only act as SP enhancers. We also added a second laser excitation at 405 nm, which would preferentially excite the SP of the Ag nanoparticle (the SP of Au nanorod would also be excited to a certain extent by the 405 nm laser due to plasmon energy transfer[57]).

The distinct SP properties of Au and Ag allowed us to differentiate the isolated and the linked Au-Ag nanostructures readily using scattering and photoluminescence (PL)

microscopy at 405 nm vs. 532 nm excitations. For Au nanorods, their transverse mode of localized SP resonance peaks at ~515 nm; they thus scatter the 532 nm light more strongly than the 405 nm light (Figure 2.3B vs. A). On the other hand, Ag nanoparticles have localized SP resonance peaked at ~415 nm and thus scatter the 405 nm light more strongly (Figure 2.3E vs. F). Moreover, both Au nanorods and Ag nanoparticles exhibit some PL. The PL intensity of Au nanorods are much stronger under 532 nm excitation (Figure 2.3D vs. C), whereas Ag nanoparticles show stronger PL under 405 nm excitation (Figure 2.3G vs. H). For linked Au-Ag nanostructures, they have appreciable scattering and PL intensities under both 405 nm and 532 nm excitations (Figure 2.3I-L). (Note the fluorescence signal of the catalytic product resorufin is detected on top of the PL signal of the nanoparticle, which is stable under continuous wave laser excitation, as we showed previously.[38])

Because of these optical properties, when we examined individual nanostructures in both scattering and PL images under 405 nm or 532 nm excitation, Au nanorods, Ag nanoparticles, and linked Au-Ag nanostructures cluster into distinct populations (Figure 2.3M), in which the linked Au-Ag nanostructures are readily identified. This optical identification can be further confirmed by subsequent SEM imaging (Figure 2.3M inset) as well as elemental analysis via energy-dispersive x-ray (EDX) spectroscopy (Figure 2.3N).

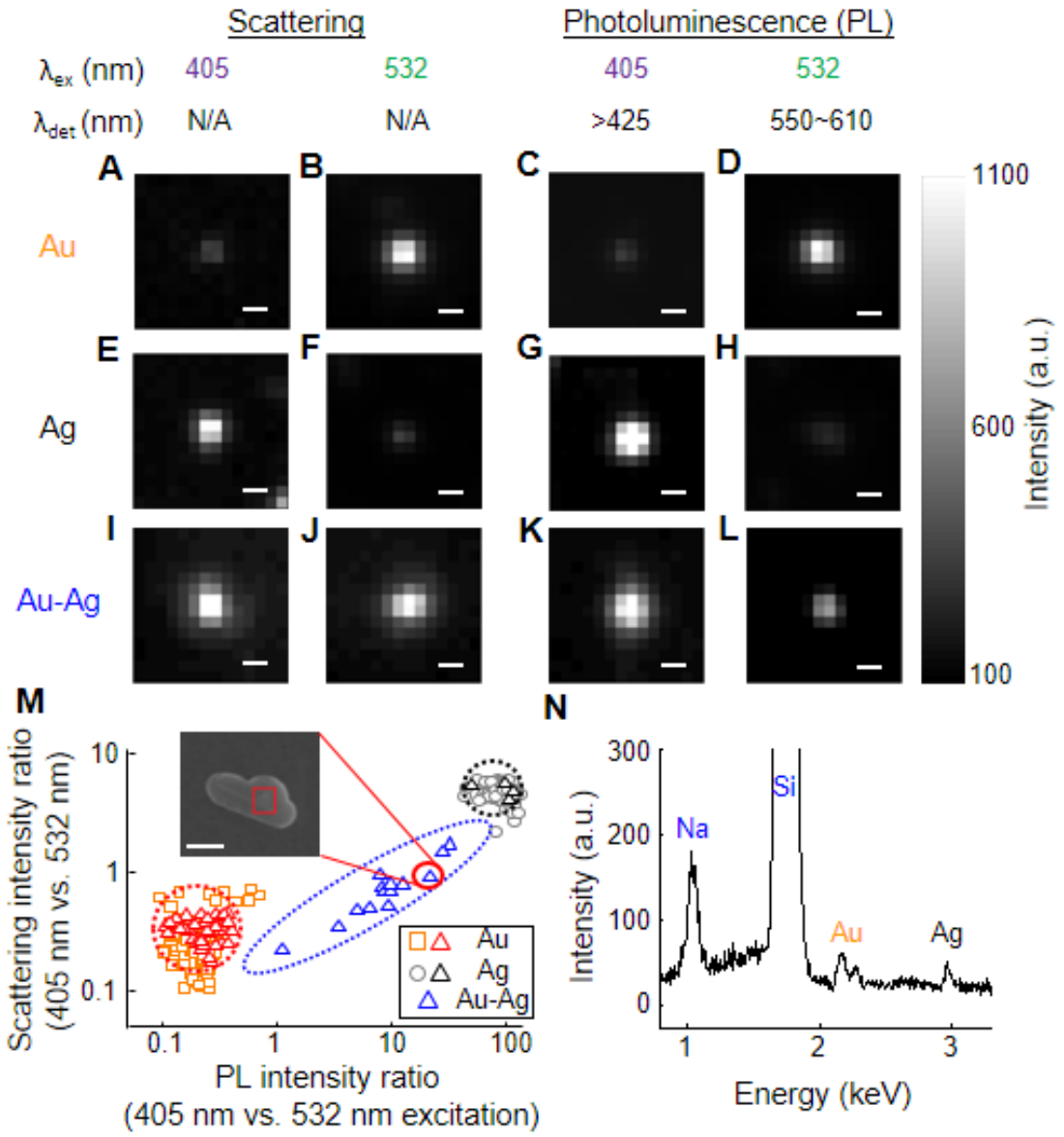

Figure 2.3. Differentiation of isolated Au and Ag, and linked Au-Ag nanostructures via optical microscopy. (**A-B**) Scattering images of a single Au nanorod under 405 nm (A) or 532 nm (B) light excitation. (**C-D**) Photoluminescence image of a single Au nanorod in the >425 nm wavelength range under 405 nm light excitation (C) or in the 550 to 610 nm wavelength range under 532 nm light excitation (D). (**E-H**) Same as A-D, but for a single Ag nanoparticle. (**I-L**) Same as A-D, but for a linked Au-Ag nanostructure. All scale bars in A-L represent 500 nm. (**M**) Scattering intensity ratio at 405 or 532 nm excitation vs. the photoluminescence intensity ratio at 405 or 532 nm excitation for

individual particles of Au nanorods (open orange squares), Ag nanoparticles (open black circles), or the sample of linked Au-Ag nanostructures (open triangles), which is a mixture of linked and unlinked nanoparticles. Au nanorods, Ag nanoparticles, and linked Au-Ag nanostructures appear as distinct populations (areas circled by red-, black-, and blue-dashed lines, respectively). Inset: SEM image of a linked Au-Ag nanostructure encapsulated in $mSiO_2$; scale bar = 200 nm. (**N**) Elemental analysis on the Au-Ag nanostructure in the inset in M via EDX spectroscopy (red box). The peaks are annotated by the elemental origin. Both Au and Ag are seen. Na and Si came from the residual cations in the experimental buffer solution and the mesoporous silica shell.

We then mapped super-resolution catalysis images of individual linked Au-Ag nanostructures onto their SEM images, as we did on linked Au-Au nanorods (Figure 2.4A-B). Catalytic hotspots are clearly observed at the Au-Ag gap, which is a few nanometers in size (Figure 2.4E) (no significant reaction products are detectable on isolated Ag nanoparticles, which are catalytically inactive). Again, this enhanced catalytic activity at the gap regions are not due to enhanced fluorescence intensity of the product molecules (Figure 2.4C), longer product residence time (Figure 2.4D), or more reactant access there (SI Section 3.5.2).

Similarly, we quantified the specific turnover rate at the gap vs. non-gap regions on these linked Au-Ag nanostructures; here only the surface area of Au nanorods was considered because Ag nanoparticles are catalytically inactive (SI Section 3.7). Pooling results from 29 linked Au-Ag nanostructures, the catalytic activities of gap regions are ~2.1 times higher on average than non-gap regions, and can be ~3.9 times higher for individual nanostructures (Figure 2.4F, H, J), clearly demonstrating the catalytic enhancements at plasmonic hotspots on these nanostructures.

We performed FDTD simulations on each linked Au-Ag nanostructure that we

experimentally studied. Both the 405 nm and 532 nm laser sources were included in the simulations, and their intensity ratios were taken from the experimental local power densities at each nanostructure. At both the 532 nm and 405 nm wavelength, the electric field intensity patterns always show localized enhancements at the gap region (Figure 2.4G, I), as expected. More important, the observed catalytic enhancement at the gap vs. non-gap regions shows a direct correlation with the relative electric field intensity enhancement (Figure 2.4H, J), clearly demonstrating that the catalytic enhancements came from local plasmonic enhancements and ruling out thermal effect as the underlying cause.

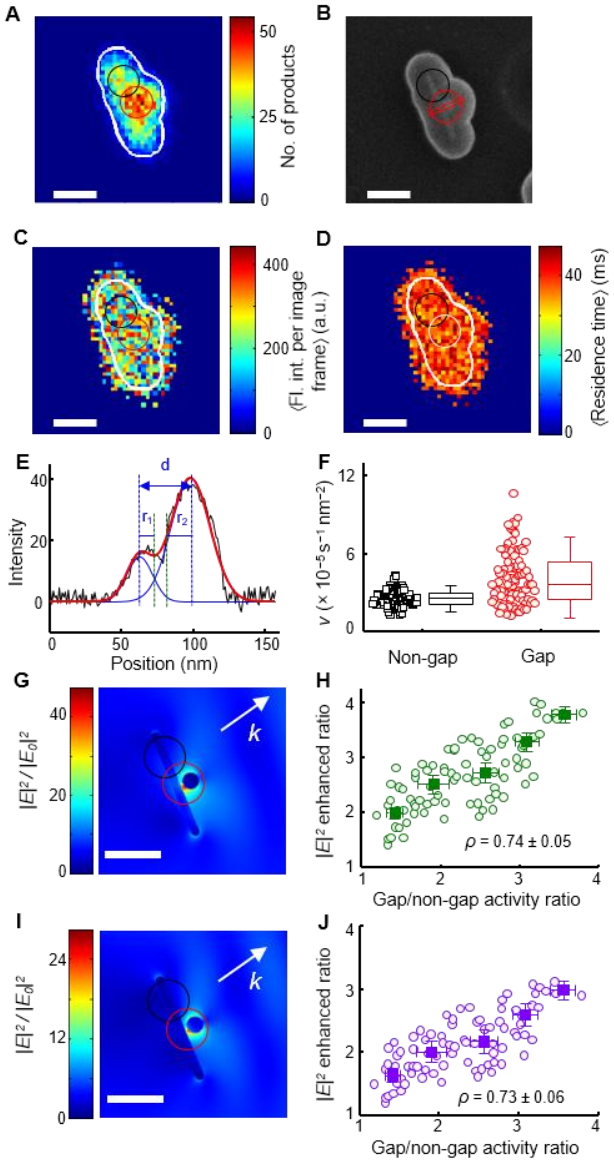

Figure 2.4. Catalytic hotspots on linked Au-Ag nanorod-nanoparticle nanostructures. (**A**) Quantitative super-resolution mapping of catalytic products on the Au-Ag nanostructure in B. White line: structure contour of the nanostructure from B. (**B**) SEM image of the linked Au-Ag nanostructure encapsulated in $mSiO_2$ in A. The red and black circles (70 nm radius) define the gap and non-gap regions. (**C**) Spatial distribution of the average single-molecule fluorescence intensity of the catalytic product resorufin per image frame (30 ms) on the nanostructure in A. (**D**) Spatial distribution of the average residence time of the catalytic product on the nanostructure in A. (**E**) Gap

size determination via line profiling of the SEM image in B (red box). The gap here is 8.2 ± 1.1 nm. (**F**) Box plot of specific turnover rate *v* of gap vs. non-gap regions on 29 linked Au-Ag nanostructures. (**G**) FDTD simulation of electric field enhancement pattern on the nanostructure in A at 532 nm. (**H**) Correlation between electric field enhancement ratios of gap vs. non-gap regions and their catalytic activity ratios. Each open circle is one nanostructure. Solid squares are binned and averaged results. All error bars represent s.d. All scale bars represent 200 nm. (**I-J**) Same as G-H, but using electric field enhancement pattern at 405 nm.

2.3.4. Catalytic enhancement decreases with larger gap.

For plasmonic nanostructures with nanoscale gaps, the local electric field enhancement at the gap region is known to depend sensitively on the gap size; the larger the gap, the smaller the enhancement. The ability to determine the gap sizes of individual linked Au-Au and Au-Ag nanostructures from SEM allowed us to evaluate how the catalytic enhancement at the gap regions depends on the gap size at the single nanostructure level.

For the linked Au-Au nanorods, there is no clear dependence on the gap size for the gap vs. non-gap activity ratio (Figure 2.5A, open black squares). This is not surprising, as for these linked nanorods, the local electric field enhancement depends not only on the gap size, but also on the relative orientation of two nanorods; the latter differs greatly from one nanostructure to another (e.g., Figure 2.1A-C). (It also depends on the incident light propagation direction, but this dependence is much smaller, contributing to ~15% difference and thus less significant here, as shown by FDTD simulations; SI Section 3.6.2.) We thus performed FDTD simulations to evaluate the effect of relative nanorod orientation on the local electric field enhancement (Figure 2.5C). With a fixed 5 nm gap and keeping all other conditions constant, the electric field enhancement could differ by as much as ~55%, when

the angle between the two nanorods is varied from 0 to 90° (Figure 2.5D). Using this angle dependence, we normalized all experimental data of individual Au-Au nanorod structure to the case of 70° angle to factor out the orientation effect. Expectedly, after this normalization, the gap vs. non-gap activity ratios of these linked Au-Au nanorods show a clear exponential[24,58] decay with increasing gap size, with a decay constant of 7.8 ± 1.6 nm (Figure 2.5A, open red circles). This decay behavior is also reproduced in FDTD simulations, where the gap size is increased while the orientations of the two nanorods are kept constant; and the decay constant there is 7.6 ± 0.3 nm (Figure 2.5B).

For the linked Au-Ag nanorod-nanoparticle structures, the gap vs. non-gap activity ratio shows a clear exponential dependence on increasing gap sizes (Figure 2.5E); here, because of the pseudospherical shape of the Ag nanoparticle, the relative orientation of the Au nanorod is less important. This exponential dependence has a decay constant of 7.1 ± 0.8 nm (Figure 2.5E), in agreement with the FDTD simulations of electric field enhancement at either 405 nm or 532 nm (Figure 2.5F).

Altogether, the gap size dependences of the catalytic activity enhancement at gap regions further support that the local plasmonic enhancement is the cause of the catalytic hotspots, in which the catalytic enhancement depends not only on the gap size but also on the geometries of the linked nanostructures.

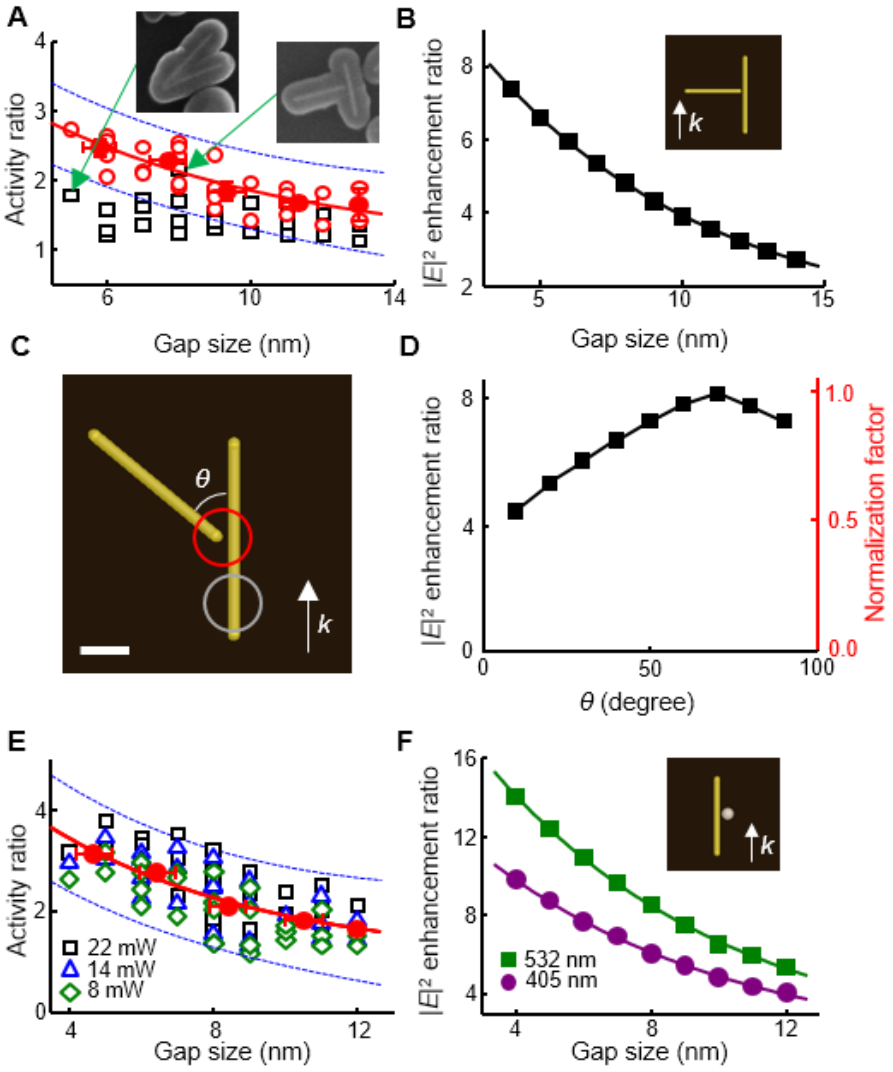

Figure 2.5. Gap size dependence of catalytic enhancement. (**A**) Activity ratios of gap vs. non-gap regions of individual linked Au-Au nanorods as a function of their gap sizes (open black squares), as well as those after normalization by the orientation effect in D (open red circles). Solid red circles are binned and averaged results of open red circles. Solid red line and dashed blue lines: exponential fit and 95% confidence bounds; exponential decay constant is 7.8 ± 1.6 nm. (**B**) Electric field enhancement ratio at 532 nm of gap vs. non-gap regions from FDTD simulation of Au-Au nanorods as a function of gap size, where the two nanorods are oriented at 90° (inset). Solid line: exponential fit with a decay constant of 7.6 ± 0.3 nm. (**C**) Model geometry for orientation effect FDTD

simulations with a fixed gap size at 5 nm of Au-Au nanostructures. (**D**) Electric field enhancement ratio at gap vs. non-gap regions as a function of the angle θ in C (left y-axis), and after normalization to that at θ = 70°. (**E**) Activity ratios of gap vs. non-gap regions of individual linked Au-Ag nanostructures as a function of their gap sizes at different 405 nm laser powers (open symbols). Solid red circles are binned and averaged results. Fitted exponential decay constant: 7.1 ± 0.8 nm. (**F**) Electric field enhancement ratios of gap vs. non-gap regions detected at 532 and 405 nm from FDTD simulations of a model Au-Ag nanostructure as a function of gap size (inset). Solid lines: exponential fits with decay constants of 6.9 ± 0.2 nm (green) and 7.2 ± 0.1 nm (purple).

2.3.5. Activity of catalytic hotspots shows quadratic dependence on light intensity.

We further examined the excitation light intensity dependence of the specific turnover rate at the gap regions of the linked Au-Au and Au-Ag nanostructures, where catalytic enhancement is observed. We determined the local incident light power density by mapping out the laser beam profile on the sample and also taking into account the evanescent field illumination geometry (SI Section 3.2.4). Strikingly, for both types of nanostructures, the specific turnover rates of the gap regions increase quadratically with increasing local incident power density of 532 or 405 nm laser (Figure 2.6A-C, open circles; linear fits to the data clearly failed; SI Figure 3.19A-C and Table 2.4). This quadratic dependence indicates that the underlying mechanism for the catalytic enhancements at these catalytic hotspots must involve two photo-excited species, such as SP-induced hot electrons or photoexcited resazurin molecules, which absorb near the excitation wavelengths (λ_{abs} ~ 570 nm). Consistently, at any local incident power density, the specific turnover rates at the gap regions, where SP enhancement is large, are always higher than those at non-gap regions,

where SP enhancement is negligible and for which the dependence on the local incident power density cannot be reliably differentiated between 1st and 2nd orders (Figure 2.6A-C, open squares).

Because of the large electric field enhancement at the gap regions, the actual light power density there is much larger than the incident light power density. Using our earlier FDTD simulations, which gave the local electric field enhancement pattern around each nanostructure, we corrected for these enhancements to obtain the actual light power density at both gap and non-gap regions. Consequently, the specific turnover rates of the gap regions now fall on the same curve as that for the non-gap regions as a function of increasing actual local power density for both the linked Au-Au and Au-Ag nanostructures at 532 or 405 nm (Figure 2.6D-F). In the range of smaller than ~1.5 kW cm^{-2}, the specific turnover rates show little dependence on the light power density, consistent with our earlier studies[48,53] on individual Au nanoparticles at an illumination power density of 0.5 to 0.75 kW cm^{-2}. In the higher range of >1.5 kW cm^{-2}, the specific turnover rates increase rapidly. Overall, the specific turnover rate v follows a second order dependence on the actual local power density I in all cases, sufficiently described by the following relation (SI Section 3.8):

$$v = A + CI^2 \qquad \text{Eq. 2.1}$$

Here A (about 2×10^{-5} s^{-1} nm^{-2}) is a light independent term, consistent with what we determined earlier[48,49] that under low light conditions, Au-particle catalyzed reduction of resazurin by NH_2OH follows the classic Langmuir-Hinshelwood mechanism, in which the excitation light plays no significant roles. C is the coefficient for the second-order dependence, and it gives the catalytic enhancement at plasmonic hotspots (i.e., gaps) where the local actual light power density is large. This second-order term again indicates that the

underlying mechanism of enhancement involves two photoexcited species.

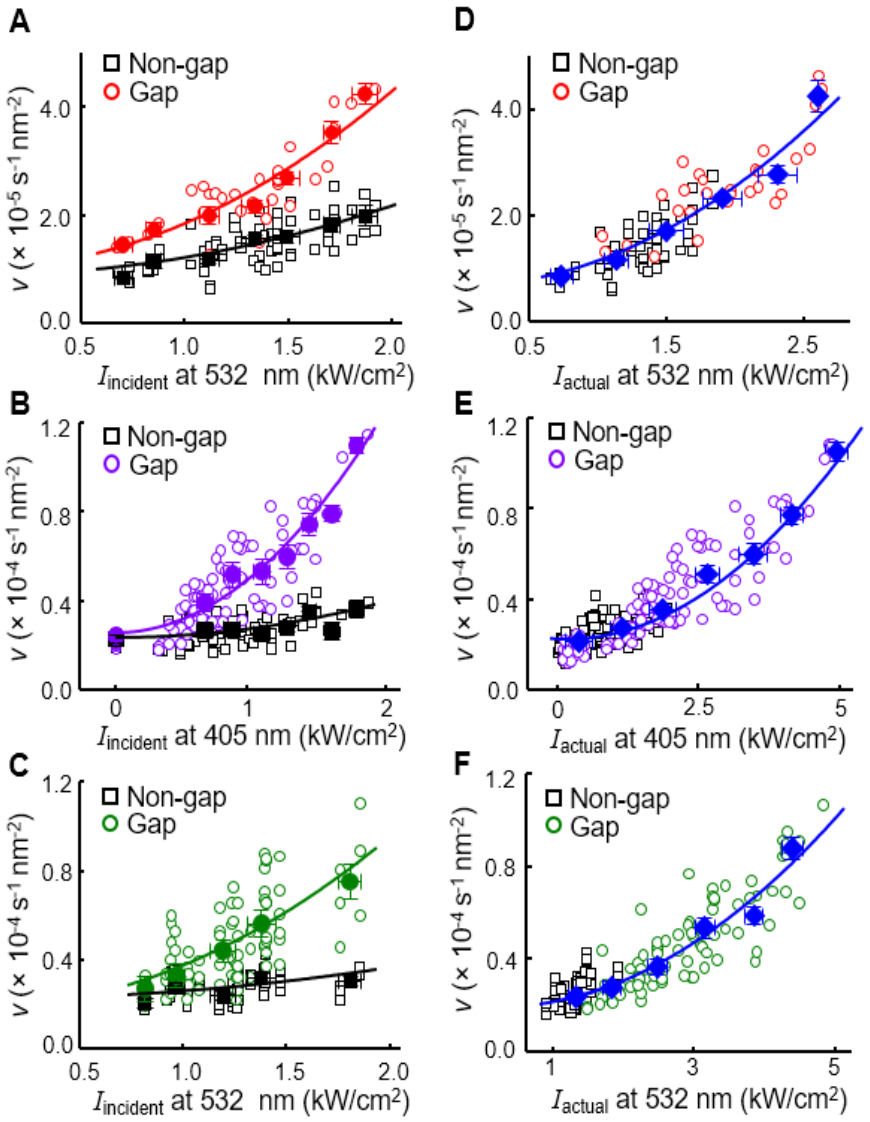

Figure 2.6. Quadratic dependence of specific activity on light intensity at catalytic hotspots. (**A**) Specific turnover rates v of individual linked Au-Au nanorods at gap and non-gap regions vs. their local incident light power density $I_{incident}$ at 532 nm. Each open symbol represents a single nanostructure. Solid symbols are binned and averaged data to obtain general trends. Lines are quadratic fits. (**B**) Same as A, but for linked Au-Ag nanorod-nanoparticle structures and for 405 nm light. (**C**) Same as B, but for 532 nm light. (**D-F**) Corresponding to A-C, respectively, in which the incident local light power density has been converted to the actual local power density using the

electric field enhancement factor obtained from FDTD simulations. *x* error bars are s.d.; *y* error bars are s.e.m.

2.4. DISCUSSION

Using correlated single-molecule super-resolution fluorescence microscopy and scanning electron microscopy, we have visualized and quantified the catalytic hotspots at nanoscale gaps on two types of linked plasmonic nanostructures. These spatially localized enhancements directly rule out the thermal effect as the enhancement mechanism, and they are also correlated with the local electric field enhancement, tunable by the gap size.

Moreover, the specific catalytic activities at these gap regions, along with those at the non-gap regions, follow an overall 2nd order dependence on the local actual light power density. This 2nd order dependence suggests that the rate-limiting step in the enhancement mechanism involves two photoexcited species. One possibility is that both of these photoexcited species are the hot electrons (e^-_{hot}) from the SP excitation, which are injected into a surface adsorbed resazurin to reduce it to the product resorufin (Figure 2.7A, mechanism ①).[10] In this mechanism, the reaction rate *v* would scale as $v \propto [e^-_{\mathrm{hot}}]^2[\mathrm{S_{ad}}] \propto I^2[\mathrm{S_{ad}}]$, where $[\mathrm{S_{ad}}]$ is the concentration of surface adsorbed resazurin. A second possibility is that one hot electron is involved and the other photoexcited species is a photoexcited resazurin ($\mathrm{S^*_{ad}}$) adsorbed on the catalyst surface, as resazurin's absorption band overlaps significantly with the SP resonance of Au (Figure 2.7A, mechanism ②). This mechanism would also predict a 2nd order light dependence of the reactant rate: $v \propto [e^-_{\mathrm{hot}}][\mathrm{S^*_{ad}}] \propto I^2[\mathrm{S_{ad}}]$. A third possibility is that both the photoexcited species are photoexcited resazurin molecules on the surface, and no hot electrons are involved; in this case, $v \propto [\mathrm{S^*_{ad}}]^2 \propto$

$I^2[S_{ad}]^2$ (Figure 2.7A, mechanism ③).

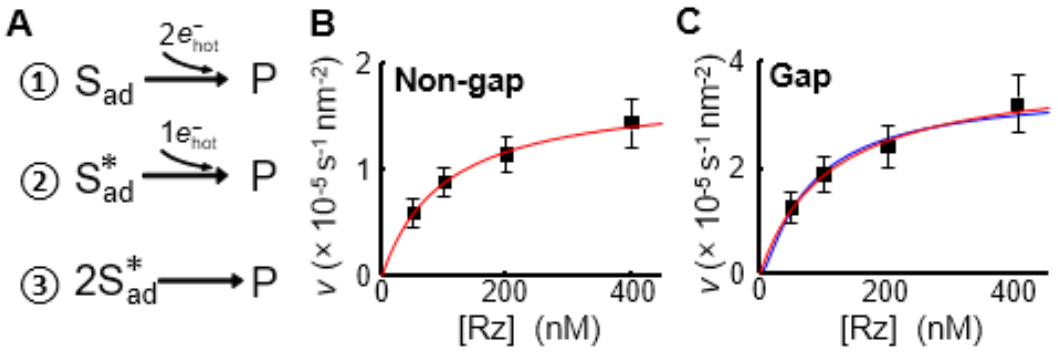

Figure 2.7. Possible mechanisms of SP-enhanced catalysis. (**A**) Three possible mechanisms of SP-enhanced catalysis, with or without involving hot electrons, all giving rise to 2nd order dependence on light power. S: resazurin; P: resorufin. (**B**) Resazurin concentration [Rz] dependence of the specific turnover rate at non-gap regions for single linked Au-Au nanorod structures. Red line: fit with equations (2), with $k_{eff} = (1.78 \pm 0.07) \times 10^{-5}$ s^{-1} nm^{-2} and $K_S = (1.01 \pm 0.09) \times 10^{-2}$ nM^{-1}. (**C**) Same as B, but for the gap regions. Red line: fit with equations (2), with $k_{eff} = (4.26 \pm 0.34) \times 10^{-5}$ s^{-1} nm^{-2} and $K_S = (0.94 \pm 0.12) \times 10^{-2}$ nM^{-1}. Blue line: fit with equation (3) with $k_{eff} = (3.96 \pm 0.32) \times 10^{-5}$ s^{-1} nm^{-2} and $K_S = (2.93 \pm 0.49) \times 10^{-2}$ nM^{-1}. Error bars are s.d.

All three mechanisms in Figure 2.7A would result in a 2nd order dependence on the light power density, but they predict different dependences on the concentration of the reactant resazurin. The reaction rates of the first two mechanisms scale linearly with $[S_{ad}]$, while that of the third mechanism scales with $[S_{ad}]^2$. Previously we have shown that resazurin adsorption on these Au nanocatalysts follows effectively the Langmuir-adsorption behavior:[48,53] $[S_{ad}] \propto K_S[S]/(1 + K_S[S])$, where [S] is the concentration of resazurin in the surrounding solution, and K_S is the equilibrium constant of resazurin adsorption on the

catalyst surface. Consequently, mechanisms ① and ② would give:

$$v = k_{\text{eff}} K_S[S]/(1 + K_S[S]) \quad \text{Eq. 2.2}$$

in which k_{eff} is an effective rate constant that can contain the light power density dependence. In contrast, mechanism ③ would give:

$$v = k_{\text{eff}} K_S^2[S]^2/(1 + K_S[S])^2 \quad \text{Eq. 2.3}$$

We thus examined the resazurin concentration dependence of the specific turnover rate to differentiate these mechanisms, using the linked Au-Au nanorods as an example. For non-gap regions where there is little catalytic enhancement and for which our previous studies[48,53] showed that the kinetics follows a Langmuir saturation kinetics, the specific turnover rate follows Eq. (1) satisfactorily, giving K_s = (1.01 ± 0.09) × 10^{-2} nM^{-1} (Figure 2.7B). For the gap regions where the catalytic enhancement is prominent, Eq. (2) also fits the data satisfactorily, giving K_s = (0.94 ± 0.12) × 10^{-2} nM^{-1} (Figure 2.7C, red line), effectively the same as that for the non-gap regions and supporting that mechanisms ① and ② are likely. Alternatively, fitting the results from the gap regions with Eq (3) gives K_s = (2.93 ± 0.49) × 10^{-2} nM^{-1} (Figure 2.7C, blue line), almost three times larger than that of the non-gap regions. As SP enhancement is not expected to affect significantly the reactant adsorption affinity to the surface, this three times larger magnitude of K_s argues against mechanism ③ that involves two photoexcited resazurin to account for the 2nd order light power dependence. Therefore, mechanisms ① and ② are more likely, and both of them involve hot electrons from the SP excitation, in which the plasmonic hotspots are the catalytic hotspots.

In conclusion, we have used single-molecule super-resolution fluorescence

microscopy, in combination with electron microscopy, to visualize directly catalytic hotspots on plasmonic nanostructures at nanometer resolution. The spatially resolved, quantitative activity information also allowed for gaining insights into the underlying enhancement mechanism, demonstrating the power of this correlative approach in interrogating nanoscale catalytic properties.

ACKNOWLEDGMENT

This research was primarily supported by the U.S. Army Research Office under Grant No. W911NF-14-1-0377. It was in part supported by the U.S. Department of Energy, Office of Science, Basic Energy Sciences, Catalysis Science Program, under Award DE-FG02-10ER16199; Army Research Office under Grant No. W911NF-14-1-0620; and National Science Foundation under Grant No. CBET-1263736. This work made use of the Cornell Center for Materials Research Shared Facilities which are supported through the NSF MRSEC program (Grant No. DMR-1120296).

REFERENCES

(1) Ditlbacher, H.; Hohenau, A.; Wagner, D.; Kreibig, U.; Rogers, M.; Hofer, F.; Aussenegg, F. R.; Krenn, J. R. *Phys. Rev. Lett.* **2005**, *95*, 257403.

(2) Liz-Marzán, L. M. *Langmuir* **2006**, *22*, 32.

(3) Wustholz, K. L.; Henry, A.-I.; McMahon, J. M.; Freeman, R. G.; Valley, N.; Piotti, M. E.; Natan, M. J.; Schatz, G. C.; Duyne, R. P. V. *J. Am. Chem. Soc.* **2010**, *132*, 10903.

(4) Link, S.; El-Sayed, M. A. *J. Phys. Chem. B* **1999**, *103*, 8410.

(5) Han, K. S.; Liu, G.; Zhou, X.; Medina, R. E.; Chen, P. *Nano Lett.* **2012**, *12*, 1253.

(6) Linic, S.; Christopher, P.; Xin, H.; Marimuthu, A. *Acc. Chem. Res.* **2013**, *46*, 1890.

(7) Linic, S.; Aslam, U.; Boerigter, C.; Morabito, M. *Nat. Mater.* **2015**, *14*, 567.

(8) Kale, M. J.; Avanesian, T.; Christopher, P. *ACS Catalysis* **2014**, *4*, 116.

(9) Brongersma, M. L.; Halas, N. J.; Nordlander, P. *Nat. Nanotechnol.* **2015**, *10*, 25.

(10) Christopher, P.; Xin, H.; Linic, S. *Nat. Chem.* **2011**, *3*, 467.

(11) Zhou, X.; Liu, G.; Yu, J.; Fan, W. *J. Mater. Chem.* **2012**, *22*, 21337.

(12) Sun, M.; Xu, H. *Small* **2012**, *8*, 2777.

(13) Kim, C.; Suh, B. L.; Yun, H.; Kim, J.; Lee, H. *ACS Catalysis* **2017**, 2294.

(14) Hung, W. H.; Aykol, M.; Valley, D.; Hou, W.; Cronin, S. B. *Nano Lett.* **2010**, *10*, 1314.

(15) Agarwal, D.; Aspetti, C. O.; Cargnello, M.; Ren, M.; Yoo, J.; Murray, C. B.; Agarwal, R. *Nano Lett.* **2017**, *17*, 1839.

(16) Alejo, C. J. B.; Fasciani, C.; Grenier, M.; Netto-Ferreira, J. C.; Scaiano, J. C. *Catal. Sci. Tech.* **2011**, *1*, 1506.

(17) Wu, X.; Thrall, E. S.; Liu, H.; Steigerwald, M.; Brus, L. *J. Phys. Chem. C* **2010**, *114*, 12896.

(18) Mukherjee, S.; Libisch, F.; Large, N.; Neumann, O.; Brown, L. V.; Cheng, J.; Lassiter, J. B.; Carter, E. A.; Nordlander, P.; Halas, N. J. *Nano Lett.* **2013**, *13*, 240.

(19) Thrall, E. S.; Preska Steinberg, A.; Wu, X.; Brus, L. E. *J. Phys. Chem. C* **2013**, *117*, 26238.

(20) Cushing, S. K.; Li, J.; Meng, F.; Senty, T. R.; Suri, S.; Zhi, M.; Li, M.; Bristow, A. D.; Wu, N. *J. Am. Chem. Soc.* **2012**, *134*, 15033.

(21) Yen, C.-W.; El-Sayed, M. A. *J. Phys. Chem. C* **2009**, *113*, 19585.

(22) Robert, H. M. L.; Kundrat, F.; Bermúdez-Ureña, E.; Rigneault, H.; Monneret, S.; Quidant, R.; Polleux, J.; Baffou, G. *ACS Omega* **2016**, *1*, 2.

(23) Zheng, Z.; Tachikawa, T.; Majima, T. *J. Am. Chem. Soc.* **2014**, *136*, 6870.

(24) Futamata, M.; Maruyama, Y.; Ishikawa, M. *J. Phys. Chem. B* **2003**, *107*, 7607.

(25) van Schrojenstein Lantman, E. M.; Deckert-Gaudig, T.; Mank, A. J. G.; Deckert, V.; Weckhuysen, B. M. *Nat. Nanotechnol.* **2012**, *7*, 583.

(26) Kurouski, D.; Mattei, M.; Van Duyne, R. P. *Nano Lett.* **2015**, *15*, 7956.

(27) Kang, L.; Xu, P.; Zhang, B.; Tsai, H.; Han, X.; Wang, H.-L. *Chem. Commun.* **2013**, *49*, 3389.

(28) Weber, M. L.; Wilson, A. J.; Willets, K. A. *J. Phys. Chem. C* **2015**, *119*, 18591.

(29) Wilson, A. J.; Willets, K. A. *Nano Lett.* **2014**, *14*, 939.

(30) Zaleski, S.; Cardinal, M. F.; Chulhai, D. V.; Wilson, A. J.; Willets, K. A.; Jensen, L.; Van Duyne, R. P. *J. Phys. Chem. C* **2016**, *120*, 24982.

(31) Stamplecoskie, K. G.; Pacioni, N. L.; Larson, D.; Scaiano, J. C. *J. Am. Chem. Soc.* **2011**, *133*, 9160.

(32) Cortés, E.; Xie, W.; Cambiasso, J.; Jermyn, A. S.; Sundararaman, R.; Narang, P.; Schlücker, S.; Maier, S. A. *Nat. Commun.* **2017**, *8*, 14880.

(33) Minamimoto, H.; Toda, T.; Futashima, R.; Li, X.; Suzuki, K.; Yasuda, S.; Murakoshi, K. *J. Phys. Chem. C* **2016**, *120*, 16051.

(34) Willets, K. A.; Wilson, A. J.; Sundaresan, V.; Joshi, P. B. *Chem. Rev.* **2017**, *117*, 7538.

(35) Chen, P.; Zhou, X.; Andoy, N. M.; Han, K.-S.; Choudhary, E.; Zou, N.; Chen, G.; Shen, H. *Chem. Soc. Rev.* **2014**, *43*, 1107.

(36) Roeffaers, M. B. J.; De Cremer, G.; Libeert, J.; Ameloot, R.; Dedecker, P.; Bons, A.-J.; Bückins, M.; Martens, J. A.; Sels, B. F.; De Vos, D. E.; Hofkens, J. *Angew. Chem. Int. Ed.* **2009**, *48*, 9285.

(37) Ristanović, Z.; Kubarev, A. V.; Hofkens, J.; Roeffaers, M. B. J.; Weckhuysen, B. M. *J. Am. Chem. Soc.* **2016**, *138*, 13586.

(38) Zhou, X.; Andoy, N. M.; Liu, G.; Choudhary, E.; Han, K.-S.; Shen, H.; Chen, P. *Nat.*

Nanotechnol. **2012**, *7*, 237.

(39) Sambur, J. B.; Chen, T.-Y.; Choudhary, E.; Chen, G.; Nissen, E. J.; Thomas, E. M.; Zou, N.; Chen, P. *Nature* **2016**, *530*, 77.

(40) Zhang, Y.; Lucas, J. M.; Song, P.; Beberwyck, B.; Fu, Q.; Xu, W.; Alivisatos, A. P. *Proc. Natl. Acad. Sci. U.S.A.* **2015**, *112*, 8959.

(41) Tachikawa, T.; Yonezawa, T.; Majima, T. *ACS Nano* **2013**, *7*, 263.

(42) Ha, J. W.; Ruberu, T. P. A.; Han, R.; Dong, B.; Vela, J.; Fang, N. *J. Am. Chem. Soc.* **2014**, *136*, 1398.

(43) Xu, W.; Shen, H.; Kim, Y. J.; Zhou, X.; Liu, G.; Park, J.; Chen, P. *Nano Lett.* **2009**, *9*, 3968.

(44) Shen, H.; Xu, W.; Chen, P. *Phys. Chem. Chem. Phys.* **2010**, *12*, 6555.

(45) Scaiano, J. C.; Lanterna, A. E. *J. Org. Chem.* **2017**, *82*, 5011.

(46) Chen, P.; Zhou, X.; Shen, H.; Andoy, N. M.; Choudhary, E.; Han, K.-S.; Liu, G.; Meng, W. *Chem. Soc. Rev.* **2010**, *39*, 4560.

(47) Chen, P.; Xu, W.; Zhou, X.; Panda, D.; Kalininskiy, A. *Chem. Phys. Lett.* **2009**, *470*, 151.

(48) Andoy, N. M.; Zhou, X.; Choudhary, E.; Shen, H.; Liu, G.; Chen, P. *J. Am. Chem. Soc.* **2013**, *135*, 1845.

(49) Zhou, X.; Choudhary, E.; Andoy, N. M.; Zou, N.; Chen, P. *ACS Catal.* **2013**, *3*, 1448.

(50) Xu, W.; Kong, J. S.; Chen, P. *Phys. Chem. Chem. Phys.* **2009**, *11*, 2767.

(51) Sambur, J. B.; Chen, P. *J Phys Chem C* **2016**, *120*, 20668.

(52) Caswell, K. K.; Wilson, J. N.; Bunz, U. H. F.; Murphy, C. J. *J. Am. Chem. Soc.* **2003**, *125*, 13914.

(53) Xu, W.; Kong, J. S.; Yeh, Y.-T. E.; Chen, P. *Nat. Mater.* **2008**, *7*, 992.

(54) Pérez-Juste, J.; Pastoriza-Santos, I.; Liz-Marzán, L. M.; Mulvaney, P. *Coord. Chem. Rev.* **2005**, *249*, 1870.

(55) Nikoobakht, B.; El-Sayed, M. A. *Chem. Mater.* **2003**, *15*, 1957.

(56) Haynes, C. L.; Van Duyne, R. P. *J. Phys. Chem. B* **2001**, *105*, 5599.

(57) Wei, W.; Li, S.; Qin, L.; Xue, C.; Millstone, J. E.; Xu, X.; Schatz, G. C.; Mirkin, C. A. *Nano Lett.* **2008**, *8*, 3446.

(58) Eric, X. J.; Xianfan, X. *Jpn. J. Appl. Phys.* **2004**, *43*, 407.

3. SUPPORTING INFORMATION OF CHAPTER TWO

3.1. Catalysts preparation and characterization

3.1.1. Synthesis of Au nanorods.

All commercial materials were used as received unless specified otherwise. All experiments were done at room temperature under ambient conditions, unless specified otherwise.

Au nanorod synthesis was based on previous work with some modification[1-3]. First, Au nanoparticle seed solution was prepared in a 20 mL aqueous solution containing 2.5×10^{-4} M $HAuCl_4$ (Aldrich) and 2.5×10^{-4} M tri-sodium citrate (Aldrich). After adding 0.6 mL of ice cold 0.1 M $NaBH_4$ solution, the solution turned into wine-red color, indicating the formation of Au nanoparticles of 3-5 nm in diameter. Within 1 h from their formation, these nanoparticles were used as seeds for further growth. Then, Au nanorods were made through a three-step growth procedure: we first prepared a solution with 2.5×10^{-4} M $HAuCl_4$, 0.1 M cetyl-trimethylammonium bromide (CTAB) (Aldrich) and 5.6×10^{-4} M ascorbic acid (Aldrich) in water, and separated the solution into three growth solutions of 9, 18, and 180 mL (labeled as Solution A, B and C, respectively). Then we added 1.0 mL of the seed solution into Solution A. After 20 seconds, 2 mL Solution A was transferred into Solution B. After another 30 seconds, all of Solution B was added into Solution C, which was then shaken and mixed for 10 seconds. Then, Solution C was kept still at 30 °C for 12 hours. The final Solution C contained both gold nanorods, pseudospherical nanoparticles and nanoplates. Solution C was further centrifuged at 600 g-force for 10 minutes. After removing most of the supernatant, the residual solution contained most nanorods. Figure 3.1 shows the TEM images of as-synthesized Au nanorods.

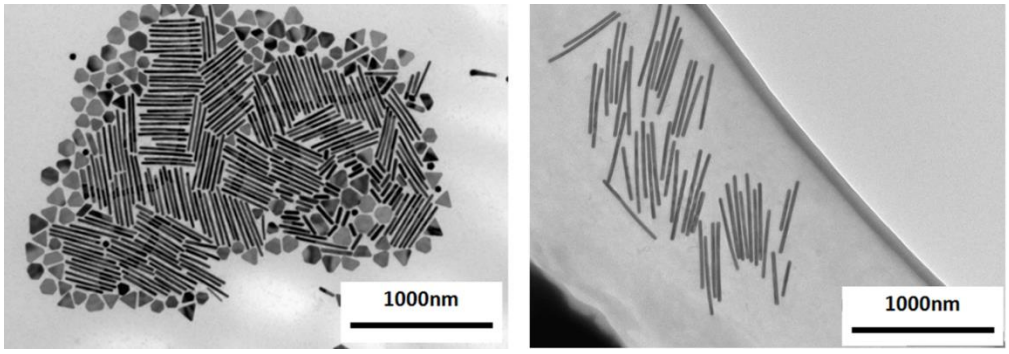

Figure 3.1. TEM images of as-synthesized gold nanorods.

3.1.2. Synthesis of linked Au-Au nanorod-nanorod and Au-Ag nanorod-nanoparticle nanostructures.

The linked Au-Au nanorod-nanorod and Au-Ag nanorod-nanoparticle nanostructures were prepared using biotin-streptavidin linkage, following Murphy et al (Figure 3.2A)[4]. First, 25 mL Au nanorod solution was mixed with 0.5 mL of 1×10^{-4} M aqueous solution of EZ-Link™ Biotin-HPDP (Thermo Scientific, Catalog No. 21341). After two rounds of stirring, sonication, centrifugation (1000 g-force for 10~15 minutes) and removing the supernatant, most unbound biotin-HPDP and spherical gold nanoparticles were removed. Pure water was added, diluting the precipitate until the volume was 25 mL. Then, this solution was equally separated to two 12.5 mL batches. After 8 to 12 hours, 0.5 mL 2×10^{-4} M streptavidin (Sigma-Aldrich, Catalog No. S4762) aqueous solution was added into one batch of the solution. After 10 minutes, this solution was centrifuged (1000 g-force for 5 minutes) and most unbound streptavidin could be removed by discarding the supernatant. Then, pure water was added into the streptavidin-coated gold nanorod precipitate until the volume was 2 mL. This streptavidin coated Au nanorod solution was

then added dropwise into the other batch of 12.5 mL Biotin-HPDP coated Au nanorod solution. Finally, unlinked gold nanorods could be preferentially removed by centrifugation (1000 g-force for 10 minutes). Figure 3.2B-E shows some TEM images of linked Au-Au nanorods.

To prepare the linked Au-Ag nanorod-nanoparticle nanostructure, we used PELCO® NanoXact™ (Ted Pella, Catalog No. 82150-50) 50 nm Ag nanoparticle as the Ag particle precursor. 1 mL Ag nanoparticle solution was diluted by water to a total volume of 12.5 mL and mixed with 0.5 mL of 1×10^{-4} M aqueous solution of EZ-Link™ Biotin-HPDP. After one round of stirring, sonication, centrifugation (1000 g-force for 10 minutes) and removing the supernatant, most unbound Biotin-HPDP was removed. Then, 12.5 mL of previously made streptavidin coated Au nanorod solution was added dropwise into this Biotin-HPDP coated Ag nanoparticle solution. Finally, another centrifugation (1000 g-force for 10 minutes) was applied to remove the unlinked nanorods and nanoparticles in the supernatant. Figure 3.2C-D shows some TEM images of linked Au-Ag nanorod-nanoparticle structures.

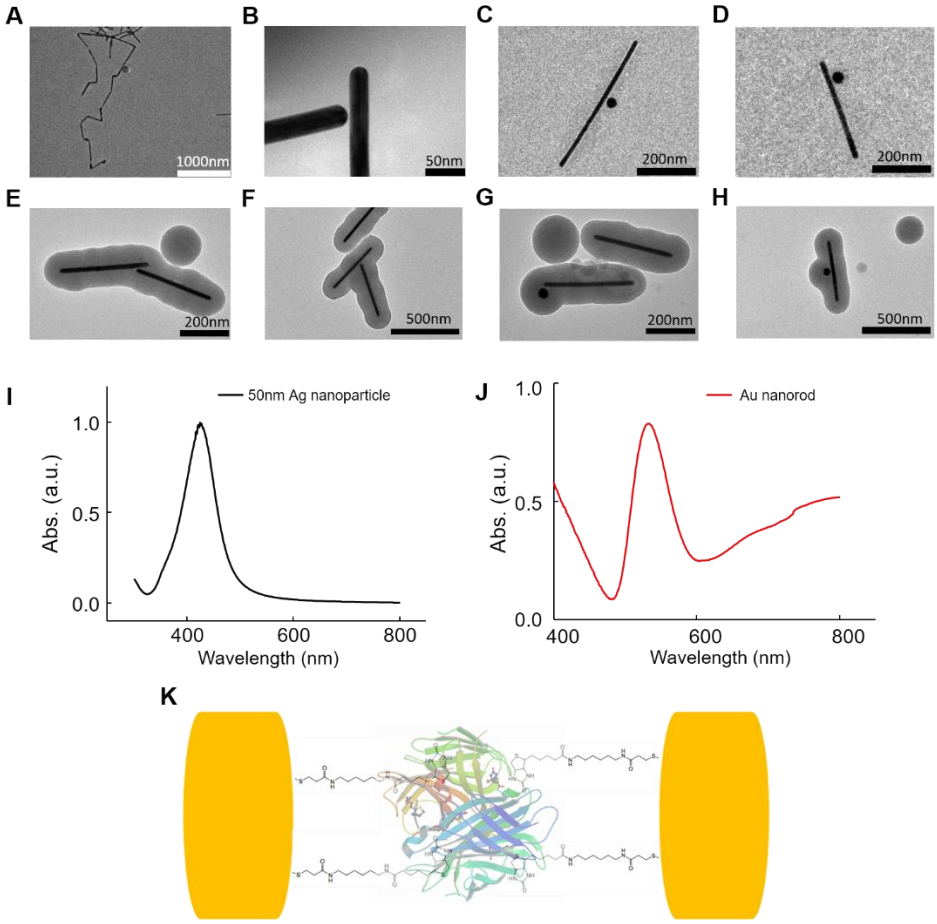

Figure 3.2. Characterization of plasmonic linked nanostructures. (**A-D**) TEM images of linked Au-Au nanorod-nanorod structures (A-B) and linked Au-Ag nanorod-nanoparticle structures (C-D). (**E-H**) TEM images of linked Au-Au (E, F) and Au-Ag nanostructures (G, H) in mesoporous silica shell. (**I**) Absorption spectrum of 50 nm Ag nanoparticles in aqueous solution, peaking at ~415 nm. (**J**) Absorption spectrum of Au nanorods in aqueous solution peaking at ~515 nm due to the transverse localized surface plasmon resonance mode. (**K**) Scheme of biotin-streptavidin linked metal nanoparticles.

3.1.3. Encapsulation of linked nanostructures with mesoporous silica and subsequent UV-ozone treatment.

Both linked plasmonic nanostructures were coated with mesoporous silica shell

through the established Ströber method[5], as we previously described in coating individual nanoparticles[3, 6]. In a typical experiment, linked nanostructures were first coated with a thin layer of amorphous silica. 1 mL of linked Au-Au or Au-Ag nanostructure solution was diluted to 25 mL aqueous solution. 5 μL of freshly prepared 20 mM 3-mercaptopropyltrimethoxysilane (MPTMS) in acetone was added while stirring vigorously. After 20 minutes, 1 mL of freshly prepared aqueous solution of 0.54% w/v Na_2SiO_3 (pH 10-11) was added drop wise and left at room temperature for 24 hours under stirring. Then, the reaction solution was centrifuged at 800 g-force for 15 min to precipitate the linked nanostructures, with a thin layer of silica of 2-4 nm in thickness. In order to grow a thicker silica shell, the precipitate was suspended in 25 mL ethanol/water (20 mL:5 mL) solution. Then, 25 μL of tetraethylorthosilicate (TEOS) and 300 μL of 0.1 M NaOH solution were added into the solution. After 24 hours continuously stirring at room temperature, a homogenous silica shell with 80-90 nm thickness could grow on the surface of metal nanostructures. Then, the silica-coated nanostructures were further centrifuged and washed at 1000 g-force for 10 min, to remove the extra NaOH and TEOS.

In order to make silica shell mesoporous, an etching process was used. First, the silica-coated nanostructures were re-suspended in 11 mL ethanol/water (10 mL:1 mL) solution. 70 μL 0.1 M NaOH and 140 μL 0.1 M CTAB were added and the solution was stirred at room temperature for 15 minutes. The solution was put in an oil bath, unstirred, at 90 °C for 2 hours. The mesoporous silica coated metal nanostructures were recovered as precipitate after centrifugation at 1000 g-force for 10 min and were then washed thoroughly, first with ethanol, then with deionized water.

After mesoporous silica shell coating, we used UV-ozone treatment to remove the

residue CTAB and other organic species on the nanostructures to activate them for catalysts, as we did previously[6-7]. First, washed nanostructures were dispersed on a glass slide and dried. Then, the sample was placed 10 cm below a 22 W Hg-UV lamp (357 nm, Atlantic Ultraviolet, Catalog No. GPH357T5VH) for 12 hours. The Au nanorods stay stable un this treatment, as we showed previously[3, 6, 8], but for Ag nanoparticles, some Ag_2O is formed during this treatment, which is reduced by ascorbic acid[9]. Here the mesoporous silica coated Au-Ag nanorod-nanoparticle structures were treated by 0.5 M fresh ascorbic acid aqueous solution for 8 hours. Then, the solution was centrifuged at 1000 g-force for 5 min to remove the supernatant containing the excess ascorbic acid. The nanostructures after this treatment could be stored in water for weeks.

3.1.4. SEM imaging and nanostructure gap size measurement

SEM was done by using LEO 1550VP FESEM operated at 10~15 keV at Cornell Center for Materials Research (CCMR). In order to differentiate the metal cores and mesoporous silica shell, both in-lens secondary electron detector and side-angle detector were used. To be able to see the gap between the two metal nanoparticles within a linked nanostructure, we reduced the noise of SEM images using line averaging. A typical imaging time is about 2 minutes.

To confirm that our SEM imaging condition can indeed reliably determine nanoparticle size, we used TEM as a calibration, by measuring the same batch of as-synthesized Au nanorods. The much higher resolution of TEM allowed us to directly measure the diameter of each Au nanorod through line profiling analysis (Figure 3.3A, B). In SEM, diameters of Au nanorods were measured by the full width at half maximum (FWHM) of Gaussian fitting the line profiles (Figure 3.3D, E). Both results from SEM and

TEM showed similar mean value and standard deviation (Figure 3.3C vs. F), indicating the accuracy of diameter measurement in SEM.

Then, we plotted line profiles of gap regions from SEM images by the same method. After subtracting a linear background (Figure 3.3G, H, upper), we fitted the line profiles of the two particles using Gaussian functions. The Gap size is defined as $d - r_1 - r_2$, where r is the radius of the nanorod/nanoparticle, determined from the FWHM of the Gaussian fit of the line profile, and d is the center-to-center distance between the nanorods/nanoparticles (Figure 3.3G, H, lower). The measured gap size distribution agrees with the expected dimension of the biotin-streptavidin linkages.[10]

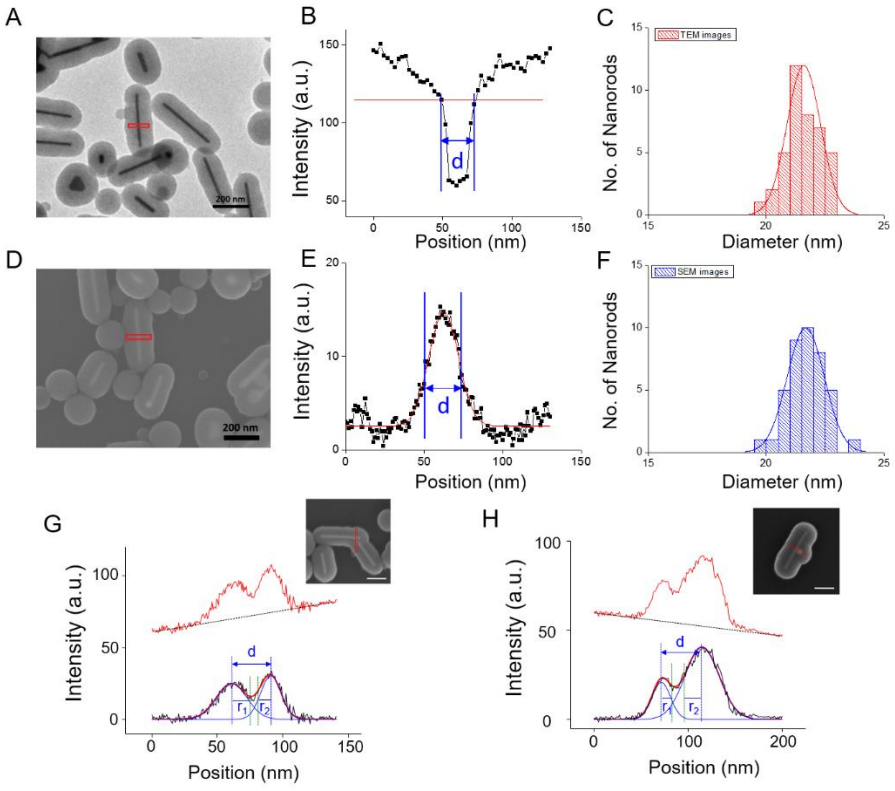

Figure 3.3. The measured diameter distribution of same batch of as-synthesized Au nanorods. (**A**) TEM image of mesoporous silica coated Au nanorods. (**B**) Line profile and diameter

measurement of the Au nanorod in the red box in A. (**C**) Distribution of Au nanorod diameters from analyzing TEM images; mean diameter is 22.3 ± 0.9 nm. (**D**) SEM image of mesoporous silica coated Au nanorods. (**E**) Line profile and diameter measurement of the Au nanorod in the red box in D. (**F**) Distribution of Au nanorod diameter from analyzing SEM images; mean diameter is 21.6 ± 0.8 nm. (**G**) The linear background subtraction from the SEM line profile for a linked Au-Au nanorods; same as main text Figure 1A. (**H**) Same as G, but for a linked Au-Ag nanorod-nanoparticle; same as main text Figure 1F. Inset in H and G are corresponding SEM images of linked nanocatalysts with line profile analysis red box. All scale bars are 200 nm.

3.1.5. EDX elemental analysis

To further confirm the identity of linked Au-Ag nanorod-nanoparticle structures, we used EDX elemental analysis. The EDX was done using a Bruker Quantax x-ray Detector attached to the SEM. Besides those peaks from carbon, oxygen, sodium, silicon, which were introduced from the carbon coating, and mesoporous silica shell and buffer solution residue, we can clearly see the presence of both Au (M line at 2.12 keV) and Ag (Lα line at 2.98 keV) (Figure 3.4). The EDX elemental analysis results also agree with the optical microscopy analysis of scattering vs. emission intensities (Figure 2.3), further proving the composition of linked nanostructures.

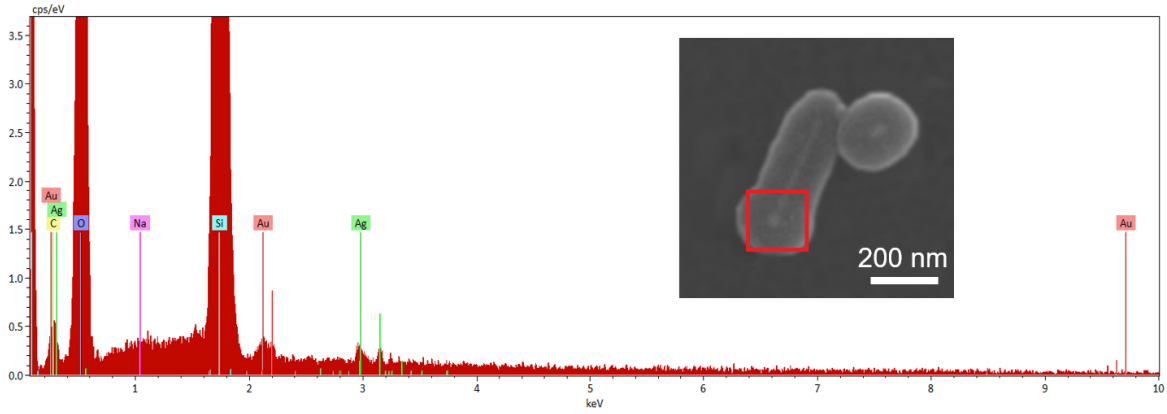

Figure 3.4. An EDX spectrum of a linked Au-Ag nanorod-nanoparticle structure. The red box of the inset shows the area where the EDX spectrum was measured.

3.1.6. Biotin-streptavidin linkage increases the yield of linked nanostructures by ~7 times.

We compared the yield of linked Au-Au nanorods with and without using the biotin-streptavidin linkage. Without the biotin-streptavidin linkage, the linked nanorods could also form by chance. Figure 3.5 shows the SEM images of mesoporous silica coated Au nanorods with and without biotin-streptavidin linkage procedure. The linkage efficiency increases by about 7 times with the biotin-streptavidin linkage method.

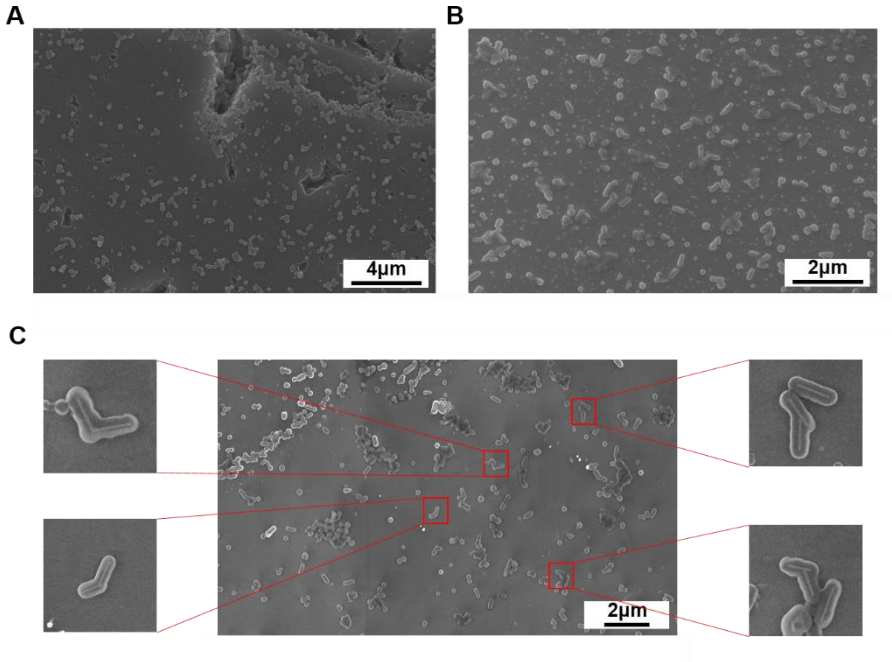

Figure 3.5. SEM images shows the linkage efficiency. (**A-B**) SEM images of mesoporous silica coated Au nanorods without using biotin-streptavidin linkage procedure. The linkage efficiency is ~4% (3 linked nanorods out of 82 nanorods). (**C**) SEM images of mesoporous silica coated linked Au-Au nanorods after biotin-streptavidin linkage procedure. The linkage efficiency is ~27% (21 linked nanorods out of 79 nanorods), 7 time larger than in A and B.

3.1.7. Ascorbic acid treatment can reduce surface Ag_2O formed during UV-ozone treatment.

To probe if ascorbic acid can indeed reduce the Ag_2O layer formed during UV-ozone treatment, we used pure Ag nanoparticles and measured their emission signal brightness excited by 405 nm laser before and after UV-zone treatment.

Ag nanoparticle emission intensity was examined under an optical microscope with 20 mW 405nm laser excitation. To detect the emission signal, a 425 nm long-pass filter was applied. The emission signal was measured for 100 Ag nanoparticles before/after UV-ozone

treatment and ascorbic acid reduction. The result shows that the emission signal intensity decreases after UV-ozone treatment, due to the partial oxidation of surface Ag atoms (Figure 3.6A-B). After ascorbic acid treatment, the emission signal intensity increases back, indicating the reduction of silver oxide (Figure 3.6C). For the linked Au-Ag nanostructures, Ag surface was protected by residual CTAB before UV-ozone treatment, which would be first oxidized by ozone. Therefore, the smaller amount of oxidized Ag atoms on the surface could be reduced more easily that bare Ag nanoparticles, and its effect on surface plasmon would be even less significant.

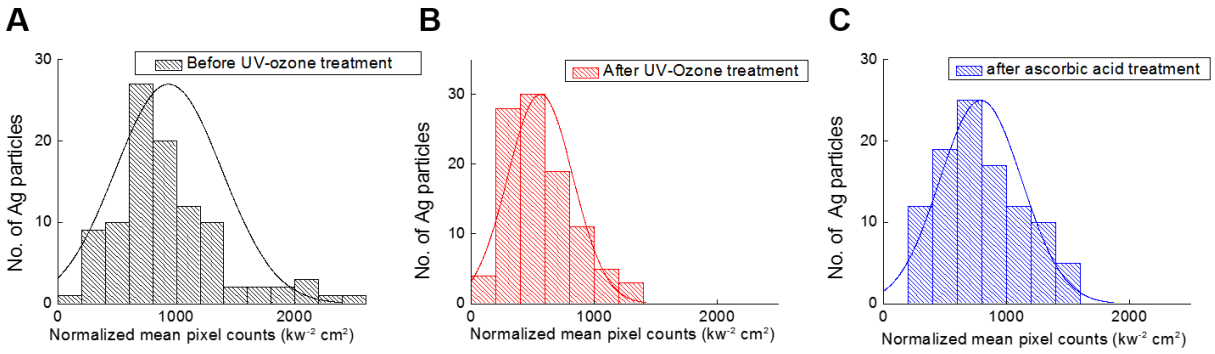

Figure 3.6. Pixel counts histograms of Ag particles during UV-Ozone treatment. (**A**) Histogram of pixel counts of emission signals from 100 Ag nanoparticles before UV-ozone treatment; the average intensity is 933.8 ± 449.1. (**B**) Histogram of pixel counts of emission signals from 100 Ag nanoparticles after UV-ozone treatment; the average intensity is 560.2 ± 264.9. (**C**) Histogram of pixel counts of emission signals from 100 Ag nanoparticles after ascorbic acid treatment; the average intensity is 788.7 ± 332.8. The pixel counts were taken from a 3×3-pixel window for averaging and normalized by the local incident 405 nm light intensity. Lines are Gaussian fits.

3.2. Single-molecule fluorescence microscopy of catalysis.

3.2.1. Single-molecule fluorescence imaging of catalysis on plasmonic nanostructures

All single-molecule fluorescence experiments were done on a homebuilt prism-type total internal reflection fluorescence (TIRF) microscope based on an Olympus IX71 microscope[3,6]. For both linked Au-Au nanorod-nanorod and Au-Ag nanorod-nanoparticle catalysts, a continuous wave circularly polarized 532 nm laser beam (CrystaLaser GCL-025-L-0.5%) of 23 mW was directed onto the sample to excite the fluorescence of the catalytic product resorufin. For linked Au-Au nanorod-nanorod catalyst, because its transverse mode of LSPR is around 520 nm,[11] no other laser was needed to excite its LSPR. For linked Au-Ag nanorod-nanoparticle catalyst, the LSPR of 50 nm Ag nanoparticle is around 400 nm[12,13], and a second CW circularly polarized 405 nm laser beam (CrystaLaser DL405-100-O) was used to excite the Ag LSPR preferentially with a power range of 0~50 mW. The fluorescence of the product resorufin was collected by a 60× NA1.2 water-immersion objective (UPLSAPO60XW, Olympus), filtered (HQ580m60, Chroma), and detected by a back illuminated ANDOR iXon EMCCD camera (DU897D-CS0-#BV) operated at 30 milliseconds frame rate.

We used reductive deoxygenation of resazurin to resorufin by NH_2OH as a probe reaction to test the catalyst activities. In single molecule fluorescence experiments, the aqueous reactant solution containing 200 nM resazurin, 6 mM NH_2OH in pH 7.2 100 mM phosphate buffer was continuously fed into a microfluidic reactor cell (~ 0.1 mm in height × 5 mm in width × 50 mm in length) with a syringe pump (Chemyx Fusion 200) at 20 μL/min. The concentration of resazurin was chosen as 200 nM at which the catalytic kinetics was approaching saturation and less sensitive to its concentration (Figure 2.7 B-C in the

main text)[14].

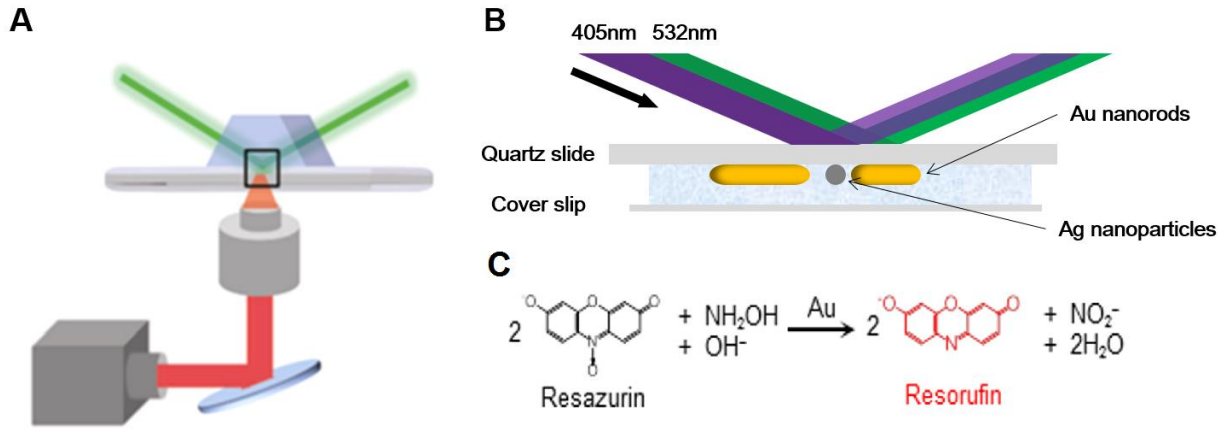

Figure 3.7. Single molecule fluorescence imaging of catalysis on plasmonic metal nanostructures. (**A, B**) Simplified scheme of the flow cell and camera set-up. The total internal reflection laser excitation illuminates an area of ≥100 × 50 μm^2. Figure A adopted from our earlier publication.[8] (**C**) Reaction schemes: the fluorogenic reductive deoxygenation of the nonfluorescent resazurin molecule (denoted as S) to the fluorescent resorufin (denoted as P) by NH_2OH, catalyzed by Au nanorods.

3.2.2. Data analysis of single-molecule super-resolution fluorescence imaging of catalytic events on individual plasmonic nanostructures.

Individual catalytic product formation events on each linked Au-Au and Au-Ag nanostructures were detected by the product fluorescence image and localized in position to nanometer precision. The general data processing methods followed our previous reports using home-written MATLAB codes[3, 6, 8].

First, we identified the individual nanocatalysts in both SEM and

scattering/fluorescence images. Both Au and Ag nanostructures scatter laser light strongly and are emissive, and are thus readily identifiable in the optical microscope. We then extracted the fluorescence intensity trajectory of each nanostructure under catalysis from the recorded fluorescence movies by integrating the EMCCD counts over a 7×7 pixels area (each pixel ~267 nm) around the nanostructure. The bursts of fluorescence intensity on top of the background emission signal of the nanostructure were due to catalytic formations of the product resorufin molecules. Then, we used intensity thresholds to select the fluorescence burst events. After cropping out an area of 13 × 13 pixels (~3.5 ×3.5 μm^2) around the product molecule, all image frames contributing to the same single burst were added together to enhance the signal to noise ratio. From this image, the background emission signal of the nanostructure was subtracted. The resulting image only contained the fluorescence signal of the catalytic product molecule resorufin. Then the image of the molecule, which behaves as a point spread function (PSF), was fitted by a two-dimensional Gaussian function (Equation Eq. 3.1) to obtain the center position (x_0, y_0) of the PSF, which reflects the position of the product molecule.

$$A\,(x,y) = \int_{x-\delta}^{x+\delta} dx \int_{y-\delta}^{y+\delta} dy\, A_0 \exp\left[-\frac{1}{2}\left(\frac{x-x_0}{\sigma_x}\right)^2 - \frac{1}{2}\left(\frac{y-y_0}{\sigma_y}\right)^2\right] + Bx + Cy + D \quad \text{Eq. 3.1}$$

In Equation Eq. 3.1, $A(x, y)$ is the intensity of a single molecule signal at position (x, y) in the corresponding image. $Bx+Cy+D$ accounts for the image background. δ is half of the pixel size. σ is the standard deviation of the two-dimensional Gaussian function along x or y direction and reflects the width of the PSF.

Due to a large number of fluorescence photons detected, the center position of each product

molecule can be localized down to a few nm accuracy[15,16], but often around 35-45 nm in this study due to the short residence time of the product on the catalyst. To reduce the contribution of noises to the selected burst events, we further filtered the selected burst events by their localization accuracies and the widths of the fitted PSF (i.e., σ_x and σ_y in Equation Eq. 3.1) as we described previously[8].

During the experiment, every movie would last for at least one hour. The flow cell could drift with sample stage. The center positions of all molecules were further corrected for microscope stage drifting, by using the intrinsic emission signal of Au nanoparticles as position markers. Similarly as described above, PSF of nanoparticle emission was fitted with a 2D Gaussian function while its center position was tracked throughout the course of the experiment. The fluorescence bursts due to product formations were excluded from this analysis. In each movie, average drifting of at least five position markers was used to correct for sample stage drift.

The positions of catalytic product molecules on a single nanostructure can be overlaid together in a scatter plot and correlated with the SEM image of the nanostructure, whose structural contour was determined from the SEM image. Their correlation with SEM image could be directly mapped using position markers, which is described below (Section 2.4). Once the structural contour of a nanostructure was mapped on top of the positions of catalytic products, the nanostructure could be dissected into gap regions and non-gap regions. Finally, product molecules were sorted to their corresponding regions, based on their positions.

3.2.3. Correcting for detection efficiency differences at different laser power densities.

In our single-molecule fluorescence imaging experiments, the detection efficiency of the fluorescent product molecules could depend on the local power density of 532 nm laser that is used to induce the product fluorescence (as well as excite the Au surface plasmon). To address potential unequal detection, we need to correct the number of detected product detection events according to their local power density of 532 nm laser. We thus performed a simulation to determine the correction for the efficiency of single-molecule detection. Figure 3.8 shows the general method of this process.

First, we obtained the distribution of σ_x, σ_y, A_0 in 2-D PSF Gaussian fitting (Equation Eq. 3.1) of the experimental single-molecule fluorescence images (Section 2.2.2). For example, Figure 3.8A-B show the σ_x and σ_y distributions of >7000 events detected on a single linked Au-Au nanorod nanostructure under 532 nm laser excitation with incident power density at 1.80 kW cm^{-2}. We could then determine the mean values and standard deviations from the distributions of σ_x and σ_y, by approximating that they follow a normal distribution (red curves in Figure 3.8A-B). Similarly, for the same nanostructure, we could obtain the distribution of A_0 and approximate that it follows a Gamma distribution (red curve in Figure 3.8D). Then, the background level of the experimental image under the same incident power density was obtained from any of the pixels that are three pixels away from the same nanostructure. The distribution of background pixel counts follows a normal distribution (Figure 3.8C).

After obtaining the information above, we could simulate single-molecule fluorescence images under the same incident power density. First, we constructed 1000 background image frames. All pixel counts in these frames are randomly sampled from the

distribution in Figure 3.8C. Second, in order to simulate a single-molecule fluorescence detection event centered at a position (x_0, y_0), we randomly sampled the values of σ_x, σ_y, and A_0 from the parameterized distributions we obtained in Figure 3.8A-B and Figure 3.8D. Third, by using the 2-D Gaussian equation Eq. 3.2, we could construct a simulated single-molecule fluorescence image centered at any position in any image frame, by adding the $A(x, y)$ value to pixels in the background frames. To simplify the simulation, the range of each simulated PSF is 7×7 pixels. Each pixel is 266 nm × 266 nm, which is the real pixel size in our experimental single-molecule fluorescence movies.

$$A\,(x, y) = A_0 \exp\left[-\frac{1}{2}\left(\frac{x - x_0}{\sigma_x}\right)^2 - \frac{1}{2}\left(\frac{y - y_0}{\sigma_y}\right)^2\right] \qquad \text{Eq. 3.2}$$

Then, we simulated a 6×6 nanostructure matrix with 100 catalytic fluorescent product events on each of them (Figure 3.8E). These 100 catalytic products were temporally distributed evenly over the 1000 movie frames (1 on-time frame with next 9 off-time frames). Finally, we had a simulated 1000-frame movie, and this movie represented the scenario under a certain local incident power density. To simulate conditions under different incident laser power densities, we chose another experimentally measured nanostructure with a different local laser power density and repeated the protocol above. Here, we performed the simulations under 4 different incident local power densities to cover our experimental range (Figure 3.8F).

Ideally, if our single-molecule fluorescence image analysis detection algorithm is selective enough, all 100 catalytic events would be detected so that detection efficiency would be 100%. However, some events would miss detection during image analysis due to limited

single-to-noise ratios. This loss is observed when we performed the same image analysis procedures on the simulated fluorescence movies, where high local laser power density is expectedly accompanied with higher detection efficiency (Figure 3.8F). In order to correct for this to be unbiased in the determination of the actual turnover rates, we normalized the detection efficiency by setting the value at the highest 532 nm laser power density as 1 and we got:

$$\eta = 0.0529\, I + 0.9048 \qquad \text{Eq. 3.3}$$

in which η represents the detection efficiency and I represents the 532 nm laser power density in unit of kW cm^{-2}. Then, Equation Eq. 3.3 was applied to all single-molecule experiments data to correct detection efficiency. Please note that even at the lowest incident power density, the detection efficiency is only ~6% less than that at the highest power density; so, this correction does not significantly change the trend of catalytic turnover rates vs. incident laser power densities.

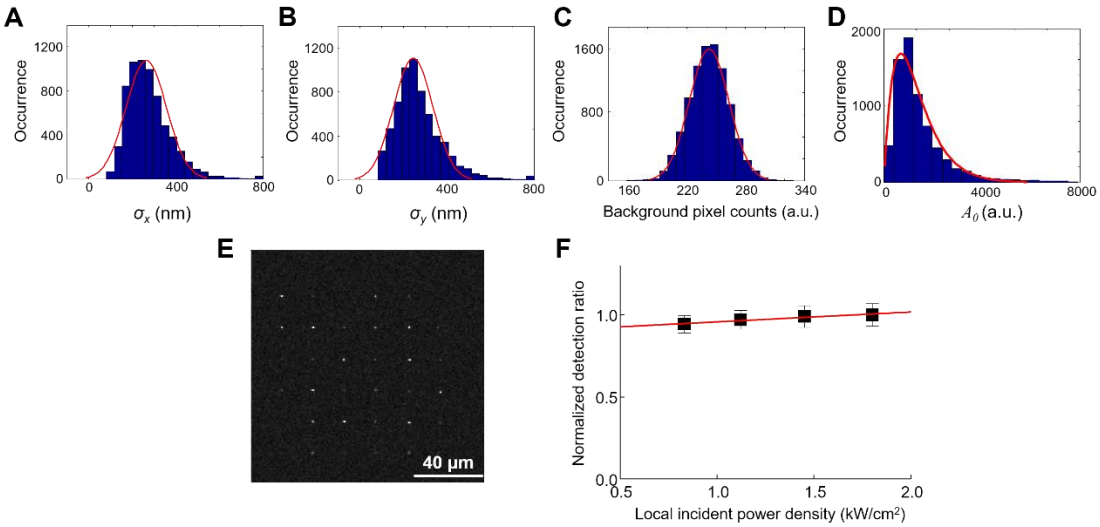

Figure 3.8. Signal detection efficiency correction for differences in local laser power densities. (**A, B**) σ_x and σ_y distributions of single-molecule fluorescence detection events from a linked Au-Au

nanorod under 532 nm laser excitation with incident power density of 1.80 kW cm^{-2}. (**C**) Distribution of the pixel count at a pixel three pixels away from the same nanostructure in A-B. Data were collected from more than 10000 experimental movie frames. The incident power density at this pixel is considered the same as the nanostructure besides it. Red curves in A-C are fits with a normal distribution. (**D**) Distribution of intensity A_0 in Eq. 3.1 from the same nanostructure in A-B. Red curve is a Gamma distribution fit. (**E**) One frame of the simulated fluorescence image in a movie on 36 nanostructures under 532 nm laser excitation with incident power density at 1.80 kW cm^{-2}, arranged in a 6×6 matrix with 20 μm distance between one another. (**H**) Fluorescence signal detection efficiencies under different 532 nm laser power densities, in which the efficiency at the highest laser power density (1.80 kW cm^{-2}) is set as one. Red line is a linear fit. Error bars represents s.d.

3.2.4. Calculating the local incident laser power from evanescent field excitation via TIR

In the single-molecule imaging experiment, the 532 nm, 405 nm, or both lasers were used to illuminate the nanocatalysts through TIR mode. In calculating the local incident power density, we also considered the evanescent field generated at the quartz-water interface, where the nanocatalysts reside. TIR excitation makes use of the exponential decay of the evanescent field generated upon total internal reflection at a high-index to low-index boundary (here is the quartz-water boundary). The intensity $I(z)$ of evanescent wave at a distance z away from the interface follows:[17]

$$I(z) = I(0)e^{-\frac{z}{d}} \qquad \text{Eq. 3.4}$$

Here $I(0)$ is the intensity at the interface, which depends upon both the incident angle and

the polarization of incident beam, and the exponential decay distance is

$$d = \frac{\lambda_0}{4\pi\sqrt{n_2^2 sin^2\theta - n_1^2}} \quad \text{Eq. 3.5}$$

where λ_0 is the wavelength of the excitation light in vacuum; n_1 is the refractive index of water; n_2 is the refractive index of quartz, and θ is the incidence angle.

For a light beam with *s*-polarization, $I(0)$ is:

$$I_s(0) = I_s \frac{4\cos^2\theta}{1 - n^2} \quad \text{Eq. 3.6}$$

where I_s is the *s*-polarized incident light intensity on the quartz slide, $n=n_1/n_2$.

For a light beam with *p*-polarization, $I(0)$ is:

$$I_p(0) = I_p \frac{4\cos^2\theta(2\sin^2\theta - n^2)}{n^4\cos^2\theta + \sin^2\theta - n^2} \quad \text{Eq. 3.7}$$

where I_p is the *p*-polarized incident light intensity on the quartz slide.

In our experiment, the incident light is circularly polarized, which means the light intensities of both the *s*- and *p*-polarized light components, I_s and I_p, are the same as half of the original light intensity I_0.[18] Therefore, $I(0)$ in Equation Eq. 3.4 should be the summation of $I_s(0)$ and $I_p(0)$ in Equations Eq. 3.6 and Eq. 3.7. To calculate the light intensity at the nanocatalyst in the TIRF excitation, z in Equation Eq. 3.4 was approximated as the average thickness of mesoporous silica shell plus half of the nanorod diameter. After applying other experiment parameters (i.e., $\theta = 67.2°$, $n_1 = 1.33$ and $n_2 = 1.46$) into equation Eq. 3.4. We obtained:

$$\begin{aligned} I_{local}^{532nm} &= 2.96\, I_0^{532nm} \\ I_{local}^{405nm} &= 2.79\, I_0^{405nm} \end{aligned} \quad \text{Eq. 3.8}$$

We have used Equation Eq. 3.8 for calculating the local incident laser power and power density.

3.3. Linked plasmonic nanostructures do not show discernible deactivation of catalytic activity over the course of our single-molecule experiments

Our catalysis imaging duration for catalytic reactions was about 3~5 hours for each experiment in which we always used freshly synthesized linked nanostructures. To evaluate if there was any significant deactivation of catalytic activity during reaction, we imaged reactions over 5 hours while keeping the reaction conditions unchanged (concentration of resazurin was at 200 nM). No significant changes in turnover rates are discernible over ~5 hours for the linked Au-Au nanorods, for example (Figure 3.9), and therefore, these linked nanostructures are stable in activity during our experimental observation time. It is worth noting that we did observe significant deactivation a week after the nanocatalysts were synthesized.

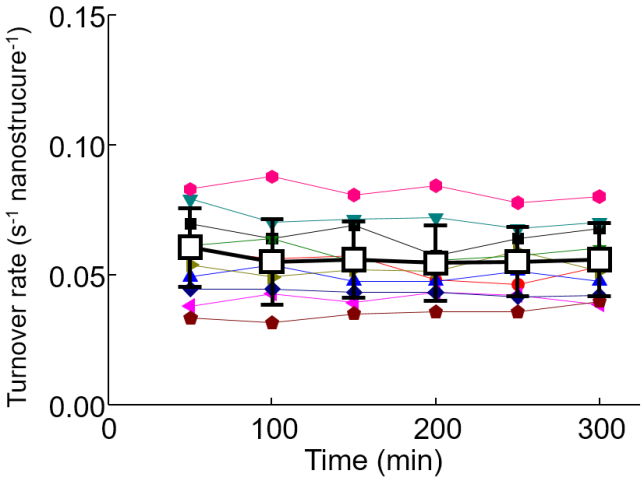

Figure 3.9. Time profiles of turnover rates of 10 individual linked Au-Au nanorods (solid symbols) and their averaged behavior (hollow squares) over 5 hours. Error bar are s.d.

3.4. Imaging correlation between super-resolution fluorescence microscopy and SEM

To correlate the structure of linked plasmonic nanostructures to the super-resolution mapping of its catalytic products, nanometer precision mapping between the fluorescence images and SEM images is needed. Direct overlaying of these two types of images is not sufficiently precise due to the slight image distortion, especially in SEM which uses line scanning to form an image, during which the sample could move slightly.

We used symmetric isolated single nanocatalysts (e.g., nanoparticle, nanorods) near the linked Au-Au or Au-Ag nanostructures as position markers to improve the accuracy of overlaying SEM and super-resolution fluorescence images. First, SEM image (Figure 3.10A) contours of individual nanostructures were extracted by using Sobel edge detection algorithm in MATLAB code (Figure 3.10B). After obtaining a binary gradient mask from edge detection, we determined the center position of each marker using the mass center of

contours (red dots in Figure 3.10B). Meanwhile, in the super-resolution image of catalytic products, the center position of every symmetric nanocatalyst was calculated by averaging all coordinates of catalytic products on top of it (white circles in Figure 3.10C). After obtaining the two sets of coordinates from the SEM image and the super-resolution catalysis image, we randomly chose a pair of nanoparticles and used them as markers to overlaying the two images together. One nanoparticle of the pair is set as the origin with coordinates (0, 0) in both images. The other nanoparticle and its coordinates were transformed by Equation Eq. 3.9 including rotation and magnification transformation.

$$\begin{bmatrix} x' \\ y' \end{bmatrix} = \boldsymbol{A} \begin{bmatrix} \cos\theta & -\sin\theta \\ \sin\theta & \cos\theta \end{bmatrix} \begin{bmatrix} x \\ y \end{bmatrix} \quad \text{Eq. 3.9}$$

After obtaining values of $\boldsymbol{A}$ and θ, we applied this transformation matrix to all other nanoparticle marker coordinates in the images. Because of the distortion, other nanoparticles may not be perfectly overlaid. Then, we calculated the summation of distance differences of these other nanoparticle markers and used this summed difference as a criterion to evaluate the overlaying procedure. We iteratively tried all combinations of pairs using the same algorithm to find the optimal $\boldsymbol{A}$ and θ, which can minimize the summation of distance differences. Figure 3.10D shows the distance error distribution from all transformation matrices in the same set of position markers. This optimization process provides overlaying error of ~7.8 nm on average, which is much smaller than the spatial resolution of our single-molecule super-resolution imaging experiments (~40 nm here).

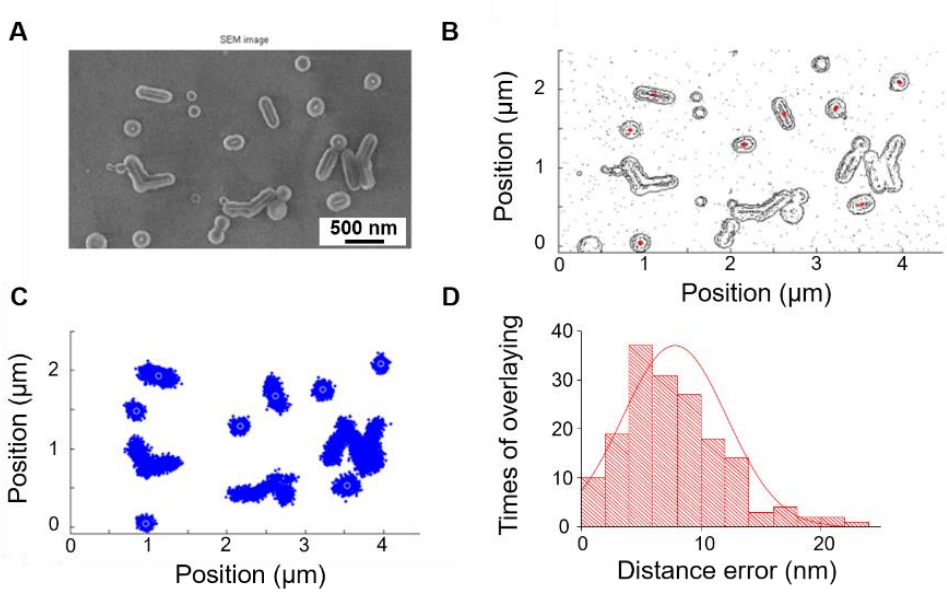

Figure 3.10. Overlaying SEM and super-resolution image of catalytic products. (**A**) SEM image of the sample. (**B**) Binary gradient mask from edge detection of image in A. Red dots represent mass centers of symmetric nanoparticles. (**C**) Locations of catalytic products from all nanoparticles in A. White circles represent mass centers of products from symmetric nanoparticles. (**D**) Distribution of overlaying distance errors of 6 nanoparticles besides the 2 chosen markers out of the 8 nanoparticles in B; the 2 markers were iterated among all possible pairs out of the 8 total.. The mean error is 7.8 ± 4.2 nm.

3.5. Other possible mechanisms of catalytic hotspots at gap regions and the rationales against them

3.5.1. Additional results to show that the observation circle size does not change the gap vs. non-gap activity ratio and there is no fluorescence intensity enhancement or increased product molecule residence time at gap regions

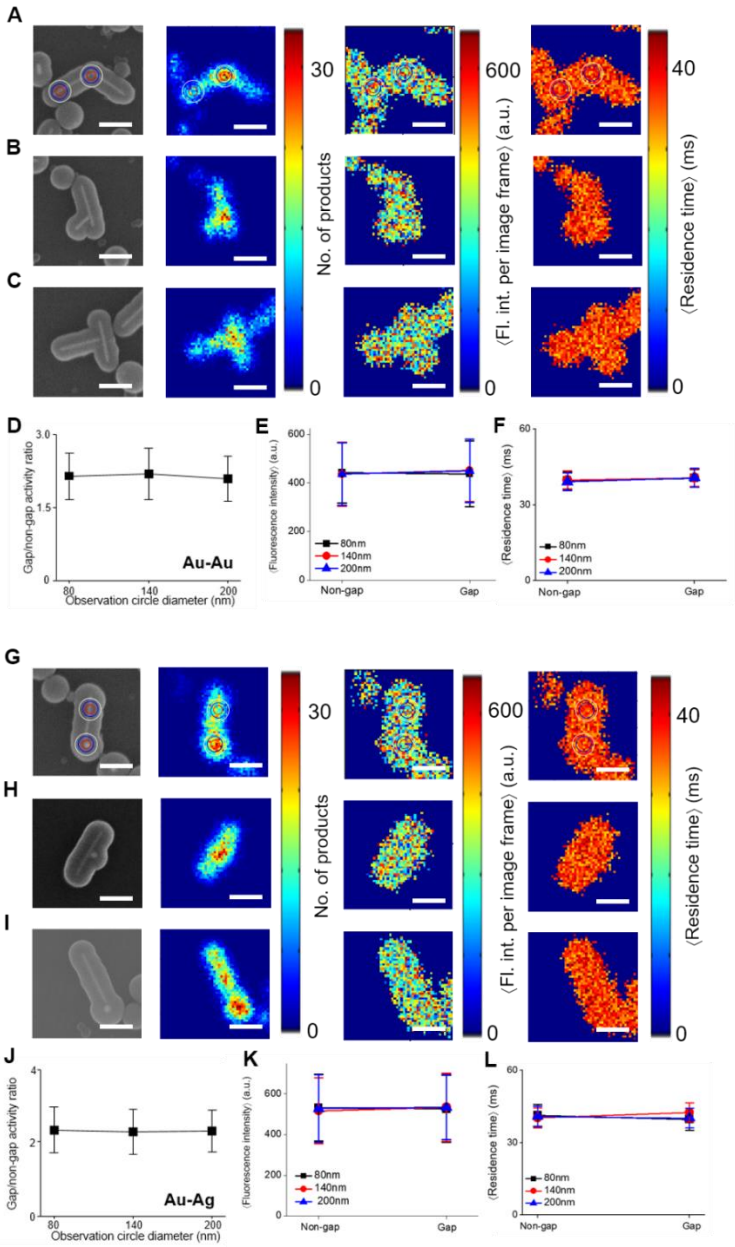

Figure 3.11. The observation circle size does not change the gap vs. non-gap activity ratio and the average fluorescence intensities of individual product molecules in each image and their average residence times at gap vs. non-gap regions do not differ significantly for both linked Au-Au and Au-Ag plasmonic nanocatalysts. (**A-C**) Three additional examples of SEM image (left), spatial pattern of the average fluorescence intensity per frame (middle), and spatial pattern of the average residence time (right) of the individual fluorescent product molecules on linked Au-Au nanocatalysts. (**D**) Gap vs. non-gap activity ratio for all 31 linked Au-Au nanorods with different observation circle diameters from 80 nm to 200 nm. (**E**) Average fluorescence intensities of the product molecules at gap and non-gap regions at different observation circle diameters, for 31 linked Au-Au nanorods. (**F**) Average residence time at gap and non-gap regions with different observation circle diameters, for 31 linked Au-Au nanorods. (**G-I**) Same as A-C, but for three additional examples of linked Au-Ag nanocatalysts. (**J-L**) Same as D-F, but for 29 linked Au-Ag nanostructures. Y-axis error bars represent standard deviation. All scale bars represent 200 nm.

3.5.2. Product rebinding experiment shows equal molecular accessibility at the gap and non-gap regions

To ensure that the detected activity differences at the gap and non-gap regions are not due to differences in the local reactant access to the metal surface through the mesopores of the $mSiO_2$ shell, we performed a control experiment in which we flowed 1 nM resorufin into the microfluidic reactor and imaged resorufin binding to the linked Au-Au nanorods encapsulated in mesoporous silica shell (Figure 3.12A-B). Here, the binding of resorufin, which is structurally similar to resazurin, probes the accessibility. Based on the background fluorescence level in the microfluidic reactor, which is proportional to the concentration of resorufin in the solution, this 1 nM concentration of resorufin is about 10 times larger than

the steady-state concentration of resorufin generated during resazurin deoxygenation reactions catalyzed by Au nanocatalysts under similar laser excitation and solution flow conditions.

Using the detected resorufin binding events on single linked Au-Au nanorods in this control experiment, we calculated the event detection rates at both the gap and non-gap regions with different observation circle diameters. The detected event is about 10 times lower than that in the catalytic reduction of resazurin, as expected. More important, there is no significant difference in the resorufin binding rate at the gap vs. non-gap regions, and the ratio is about 0.97 ± 0.11 (Figure 3.12C and D). Therefore, the observed activity differences at the gap and non-gap regions are not due to different reactant accessibility.

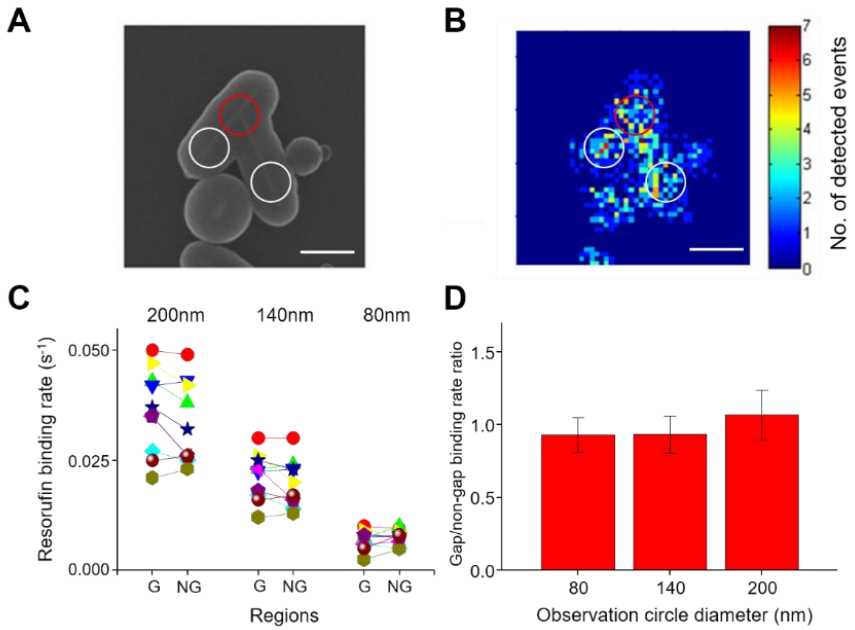

Figure 3.12. Resorufin binding to the linked Au-Au nanorods (**A**) SEM image of a linked Au-Au nanorod. Red and white circles represent the gap and non-gap regions (140 nm diameter here). (**B**) 2-D histogram of detected resorufin binding events on the nanostructure in A. All scale bars are 200

nm. (**C**) Resorufin binding rate with different observation circle diameters at gap (G) and non-gap (NG) regions of individual linked nanostructures. Each pair of linked symbols represents a single nanostructure. (**D**) Average resorufin binding rate ratio of gap vs. non-gap regions of individual linked Au-Au nanostructure with different observation circle diameters.

3.5.3. Thermal effect should not be the activity enhancement mechanism

Another potential mechanism for the catalytic hotspots at gap regions is the temperature increase caused by the plasmonic thermal effect. However, this mechanism would not generate any spatial temperature heterogeneity within a single nanostructure due to the high thermal conductivity of Au and Ag, which would make the thermal effect homogenous across a single nanostructure.

To probe the spatial and temporal profile of temperature on our nanocatalyst, we used the 1-D thermal diffusion equation to examine the heat dissipation[19]:

$$\frac{\partial T}{\partial t} = \alpha \frac{\partial^2 T}{\partial x^2} = \frac{k}{\rho c_p} \cdot \frac{\partial^2 T}{\partial x^2} \qquad \text{Eq. 3.10}$$

in which α is the thermal diffusivity of the material, k is its thermal conductivity, ρ is its density, and c_p is its specific heat.

In our experiments, the incident light power density is between $0.6 \sim 2 \times 10^3$ W/cm^2. The diameter of nanorods we used is about 20 nm. As the heat generation is only due to the excitation of the transverse SP mode of Au nanorod (~510-540 nm) by the 532 nm laser and a previous research[20] demonstrated that the Au nanoparticles with similar size only show a maximal temperature increase of 1 K, we chose a 5 K initial temperature increase at the center, which would be an overestimate of the upper bound of the temperature increase.

Moreover, we assume the dimension of material is 400 nm in length. Since all experiments were conducted in a microfluidic flow cell with continuous solution flow at room temperature, the boundary condition for solving the differential equation Eq. 3.10 is that $\frac{\partial T}{\partial t} = 0$ at x = 200 or -200 nm, i.e., there is no temperature change at the edge of material due to the thermal bath provided by the surrounding solution environment. We simulated temperature profiles using different materials, including water, silica, gold and silver. Other parameters in this simulation are shown in Table 3.1.

Table 3.1. Parameters for heat dissipation simulations. All values are from CRC Handbook of Chemistry and Physics.

Material	**Thermal Conductivity** k **(W • m^{-1} • K^{-1})**	**Density** ρ **(kg • m^{-3})**	**Specific Heat** c_p **(J • kg^{-1} • K^{-1})**
Water	0.58	1000	4180
Silica	1.30	2648	703
Gold	310	19320	129
Silver	429	10490	233

Figure 3.13A and B show the simulated time-dependent temperature profile along one dimension for water and gold. For water and silica, a local temperature jump of 5 K at the center would dissipate in ~200 ns (Figure 3.13C); for gold and silver, the same temperature jump would dissipate in 2 ns (Figure 3.13D). Therefore, a SP excitation induced local heating at the gap would dissipate quickly within a single nanostructure, at a time scale 7 to 9 orders of magnitude faster than the average catalytic product generation rate on our nanostructure (every 10 to 30 s per nanostructure). Therefore, at the timescale of catalytic

turnovers, a single nanostructure is always thermally homogeneous, with no thermal hotspots that would give rise to the observed catalytic hotspots.

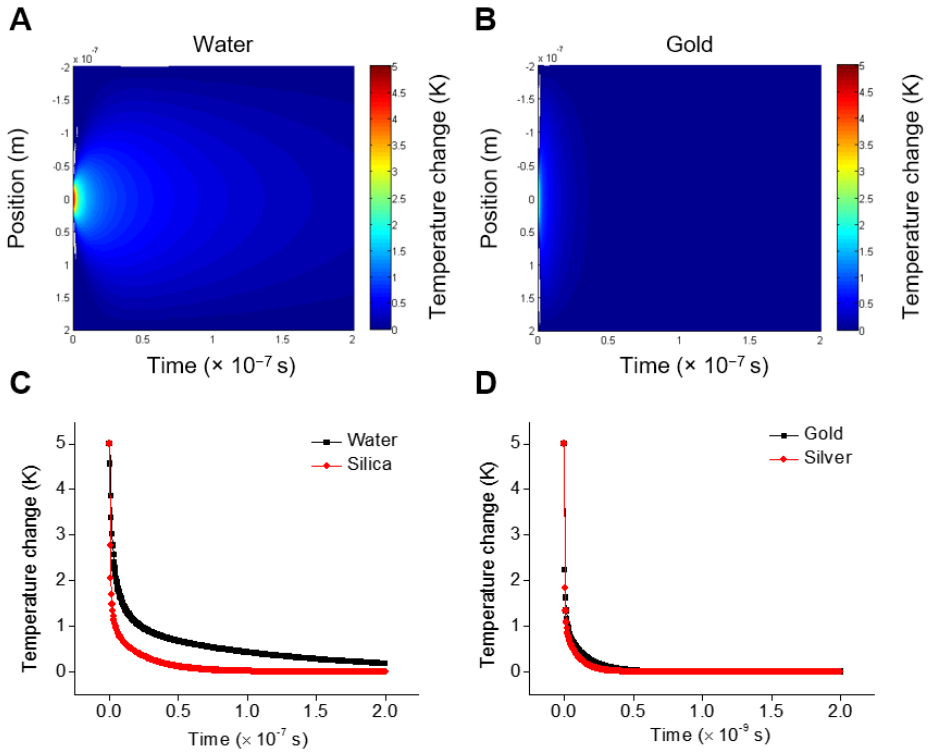

Figure 3.13. Simulated time-dependent temperature profile. (**A**) Simulation of time-dependent one dimensional temperature profile of water after a local 5 K temperature jump at position 0. (**B**) Same as A, but for gold. (**C**) The temperature change at position 0 with time, showing the heat dissipation rate on water and silica. (**D**) Same as C, but for gold and silver.

3.6. FDTD simulations, and additional simulation results

3.6.1. General method of FDTD simulation.

FDTD simulations were carried out using the simulation package FDTD Solutions from Lumerical Solutions, Inc. Our FDTD simulations use the experimental configuration of our single molecule fluorescence imaging and the nanostructure geometry determined from SEM to obtain the electric field enhancement pattern around every plasmonic nanostructure. The simulations were done in 2-D, to save computational time, as commonly done in the literature[21,22]. The detailed methods and parameters are described below:

(1) The light sources (i.e., 532 nm and/or 405 nm laser) were always circularly polarized. To generate the circular polarization for each wavelength, two overlapping light sources with orthogonal polarization direction and 90° initial phase difference was applied.[23] Light propagation directions were from the experimental geometry and are in the plane of the nanostructure from the evanescent field excitation from total internal reflection excitation geometry. When two wavelengths were used, their relative powers were taken from experimental values.

(2) The geometry of each gold nanorod in linked nanostructures was taken as a cylinder capped with hemispheres at two ends, of 22 nm in diameter. The length was determined from SEM image. The geometry of silver nanoparticles was taken as a sphere of 50 nm in diameter. Other geometry parameters (e.g. angles between nanorods, relative positions of Ag nanoparticles) were taken directly from SEM image (e.g., Figure 3.14A-D).

(3) Considering that the spatial resolution of our single-molecule super-resolution imaging was about 40 nm[8], we set the grid size as 1 nm × 1 nm in two-dimensional FDTD simulation, which was 40 times smaller than the spatial resolution. The surrounding environment was

set as pure water to simulate the aqueous solution (using silica as environment produced similar results). All dielectric constants were from Palik's Handbook of Optical Constants of Solids.[24]

(4) Electric field enhancement patterns were visualized on the *x*-*y* planes as $|E|^2/|E_0|^2$. To calculate the local electric field enhancement value at the gap and non-gap regions, the electric field enhancement within 3 nm away from the metal surface was used, as the catalytic reactions happen on the surface of metal nanoparticles and the molecules are only ~1 nm in size, and averaged within a circular region centered at the gap or a non-gap region (Figure 3.14E-F).

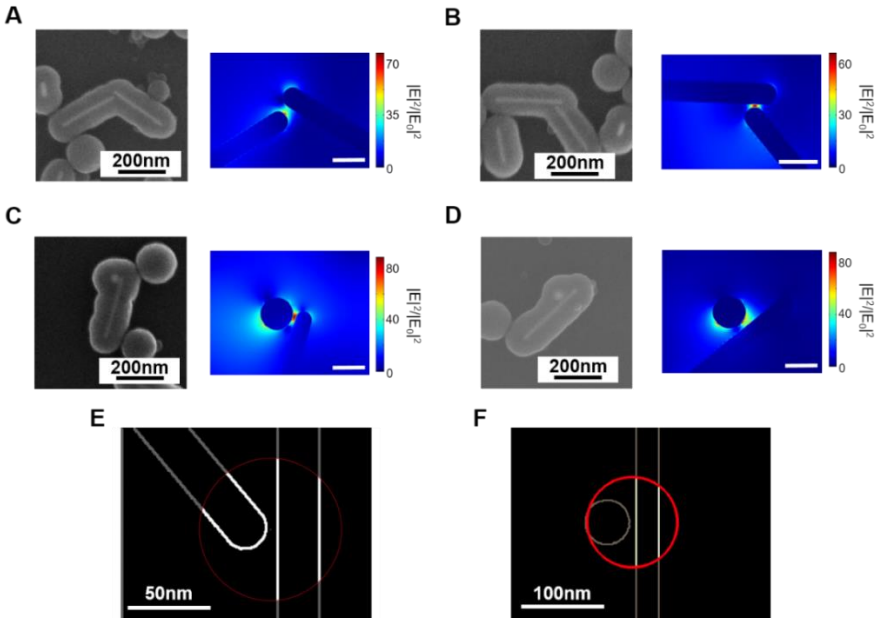

Figure 3.14. Examples of FDTD simulation. (**A-D**) Additional examples of SEM images of linked Au-Au nanorod (A, B) and Au-Ag nanorod-nanoparticle (C, D) nanostructures and corresponding electric field intensity distribution at 532 nm from FDTD simulation. All scale bars in FDTD simulations are 50 nm. (**E-F**) Averaging electric field enhancement was calculated by averaging the data points located within 3 nm from the Au surface (thick white lines) within a circular region (red line).

3.6.2. Electric field enhancement ratio of gap vs. non-gap regions depends less significantly on the direction of incident light propagation than on the linkage geometry

In the main text, we have shown that the local electric field enhancement ratio at gap vs. non-gap regions depends not only on the gap size, but also on the relative orientation of the two nanorods (i.e., linkage geometry). We also used FDTD simulations to demonstrate that the electric field enhancement ratio of gap vs. non-gap regions does not depend significantly on the propagation direction of incident light. Here, we used the two model geometries of Au-Au and Au-Ag linked nanostructures (Figure 3.15A-B) in simulation. By changing the angle (φ) between the light propagation direction and the x-axis from 0° to 180°, we calculated the electric field enhancement ratio at gap vs. non-gap regions for both nanostructures. The results show that the electric field enhancement ratio varies depending on the angle φ, but the variations between the maximum and minimum enhancements are between 13%-17% for both Au-Au and Au-Ag linked nanostructures, much smaller than the variation (~55-65%) caused by the differences in the gap size (Figure 2.5B and F) and that (~47%) caused by differences in the relative orientations of the two nanorods (Figure 2.5D). Therefore, the effect of light propagation direction on local electric field enhancement ratio of gap vs. non-gap is a less significant factor.

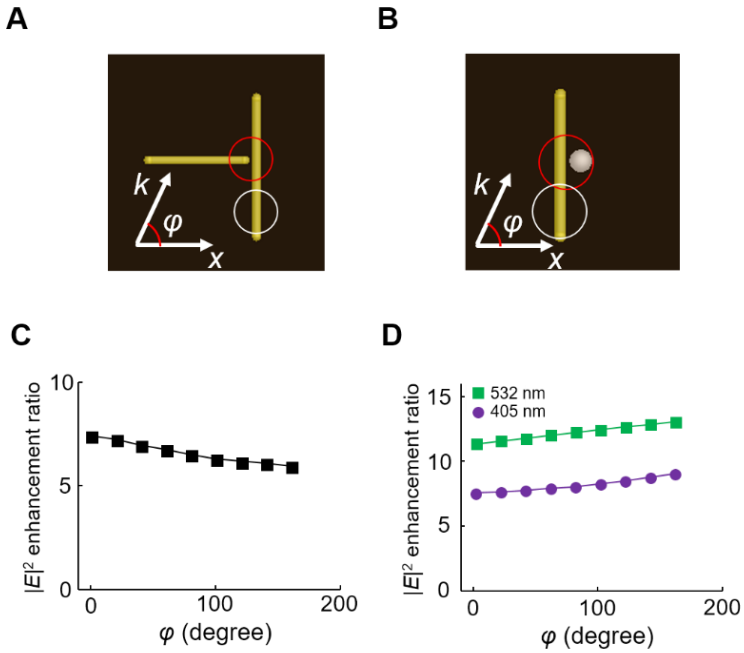

Figure 3.15. Electric field enhancement does not depend on the direction of light propagation. (**A**) Model geometry in FDTD simulations with 532 nm excitation for light propagation direction effect with a 5 nm gap for linked Au-Au nanorods. (**B**) Model geometry in FDTD simulations with simultaneous 532 nm and 405 nm excitation (equal intensities) for light propagation direction effect with a 5 nm gap for linked Au-Ag nanostructures. (**C**) Electric field enhancement ratio at gap vs. non-gap regions as a function of light propagation direction from FDTD simulations of the model Au-Au nanostructure in A. (**D**) Same as C but for the model Au-Ag nanostructure in B with two different detection wavelengths.

3.6.3. Localization error due to plasmonic antenna effect is less than ~20 nm, significantly smaller than the experimental localization precision of ~40 nm

In our single-molecule imaging experiments, all product molecules are detected around plasmonic nanocatalysts, in which the fluorescence emission could potentially couple to the plasmon resonance of the nanostructure via near-field antenna effect, leading

to a shift of the apparent position of the fluorescent molecule from its actual position. This antenna-effect typically cause an apparent position shift of ~20 nm of individual molecules,[21] smaller than our experimental localization precision (~40 nm) and much smaller than the circle diameter (80, 140, or 200 nm) that we use in picking out gap and non-gap regions. Therefore, we expect this antenna effect has no significant influence in our mapping the product locations on individual linked Au-Au and Au-Ag nanostructures. Nevertheless, in order to evaluate the potential localization error due to the plasmonic antenna effect, we carried out FDTD simulations on fluorescence emission from this molecule-antenna hybrid to quantify the effect.

In these FDTD simulations, a dimensionless emissive dipole was used to model a resorufin product molecule, emitting at 580 nm, the center wavelength of the optical bandpass filter in detecting the fluorescence of resorufin in our single-molecule imaging experiments. We used a T-shaped Au-Au nanorod linkage structure with 5 nm gap size as an example (Figure 3.16C). The dipole orientation was set to be one of the three orthogonal directions in a 3-dimensional space (parallel to x, y or z axis), while the distance between the dipole and the gold nanorod surface was set to be 5 nm to emulate the scenario of molecule-antenna hybrids (Positions 1, 2, and 3 in Figure 3.16C). As a comparison, another position of the emitting dipole at 100 nm away from Position 1 and 3 was also simulated (Position 4 in Figure 3.16C). For each geometry, the near-field electromagnetic intensity was calculated (e.g., Figure 3.16A). The far-field image was obtained by calculating the Fourier transform of Poynting vector within a certain monitoring volume and then applying an objective with a numerical aperture of 1.2 to mimic the image acquisition process in experiments. Then, the far-field image was fitted by a 2D Gaussian function to determine

the apparent centroid location of the molecule (Figure 3.16B), which can be compared with the actual position of the molecule in the simulation input. In Figure 3.16D, the results show that the apparent centroid position of the molecule is shifted by less than 20 nm from its actual position in all simulated cases, which is significantly less than the average localization precision of our single-molecule experiments (~40 nm). This verifies that the antenna effect around plasmonic nanostructures in our experiments would not change significantly the mapping of the catalytic product molecules.

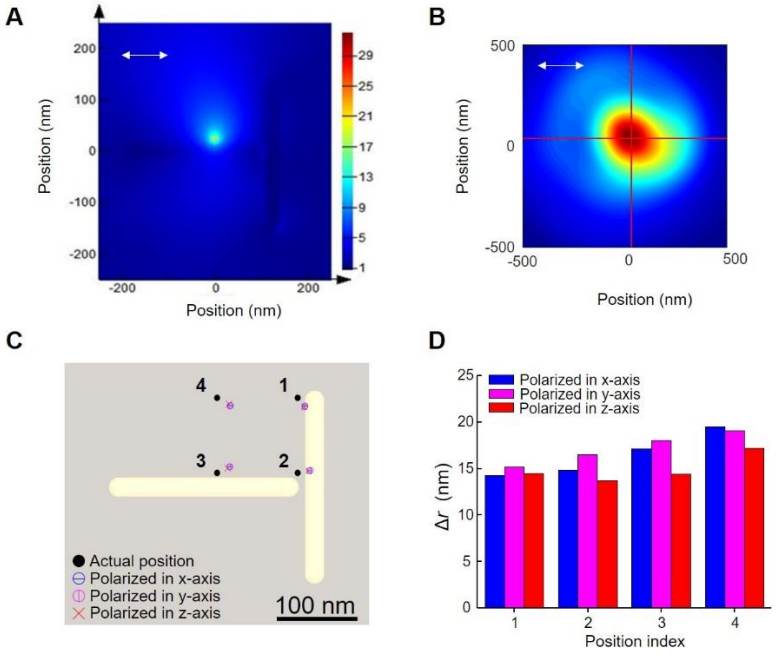

Figure 3.16. FDTD simulation on localization error due to plasmon antenna effect. (**A**) Near-field electric field pattern around a T-shaped Au-Au nanorod linkage structure with a dipole polarized along *x*-axis at Position 3 in C. (**B**) Corresponding far-field emission image of A and a 2D Gaussian fit to determine the centroid position (cross of the two red lines). (**C**) Comparison between actual molecule positions and apparent positions from the far-field imaging for all simulated cases with different dipole positions and polarization directions. (**D**) Location differences between actual positions and apparent positions.

3.7. Nanocatalyst surface area calculation within observation circles

3.7.1. Approximation of Au surface areas of linked Au-Au and Au-Ag nanostructures

For the calculation of Au nanorod surface area inside an observation circle, we first estimated the surface area through its geometry. Figure 3.17 shows typical linkage geometries of linked Au-Au nanorod structures, in which *C* is the center position of the gap; *O* is the center position of the hemisphere cap of Au nanorod; *K's* are the crossing points of the observation circle and the nanorod's central axes; *CM's* represent the vertical distances between the gap center and the central axes of the nanorods.

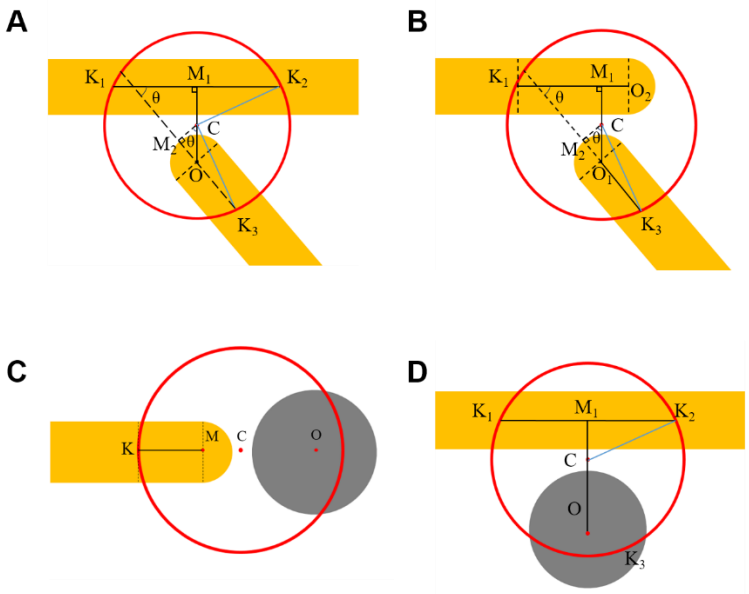

Figure 3.17. Typical linkage geometries of (**A, B**) Au-Au nanorod-nanorod and (**C, D**) Au-Ag nanorod-nanoparticle structures.

For the geometry in Figure 3.17A, total surface area within the red circle is from adding two nanorods' surface area. The surface area of one nanorod in the circle is approximated by the side surface area of a cylinder with a length of K_1K_2. The surface area

of the other nanorod is approximated by adding a hemisphere surface area and a cylinder with a length of OK_3.

Setting the diameter of nanorods as *d,* the gap size as *G*, the angle between two nanorods as θ, and the radius of observation circle as *R*, the surface area of the hemisphere is $\frac{\pi d^2}{2}$. The surface area of the two cylinders are $\pi d(K_1K_2+OK_3)$. The total nanorod surface area in the observation circle in Figure 3.17A is then:

$$S_A = \frac{\pi d^2}{2} + \pi d(K_1K_2+OK_3)$$

And

$$K_1K_2 = 2M_1K_2 = 2\sqrt{CK_2{}^2 - CM_1{}^2} = 2\sqrt{R^2 - \left(\frac{d+G}{2}\right)^2}$$

Since

$$CO = \frac{d+G}{2}$$

$$CM_2 = CO \cdot \cos\theta = \frac{d+G}{2} \cdot \cos\theta$$

$$OM_2 = CO \cdot sin\theta = \frac{d+G}{2} \cdot sin\theta$$

$$M_2K_3 = \sqrt{CK_3{}^2 - CM_2{}^2} = \sqrt{R^2 - \left(\frac{d+G}{2} \cdot \cos\theta\right)^2}$$

$$OK_3 = M_2K_3 - OM_2 = \sqrt{R^2 - \left(\frac{d+G}{2} \cdot \cos\theta\right)^2} - \frac{d+G}{2} \cdot sin\theta$$

Therefore,

$$S_A = \frac{\pi d^2}{2} + \pi d\left(2\sqrt{R^2 - \left(\frac{d+G}{2}\right)^2} + \sqrt{R^2 - \left(\frac{d+G}{2}\cdot\cos\theta\right)^2} - \frac{d+G}{2}\cdot sin\theta\right) \quad \text{Eq. 3.11}$$

For the geometry in Figure 3.17B, the surface area was obtained by adding two nanorods' surface area as well. Each nanorod is approximated by adding a hemisphere surface area and a cylinder of length of O_2K_1 or O_1K_3. By applying the same variables as the above calculation, the total nanorod surface area in observation circle in Figure 3.17B is:

$$S_B = \pi d^2 + \pi d(O_2K_1 + O_1K_3)$$

And

$$O_1K_3 = M_2K_3 - O_1M_2 = \sqrt{R^2 - \left(\frac{d+G}{2}\cdot\cos\theta\right)^2} - \frac{d+G}{2}\cdot sin\theta$$

Therefore

$$S_B = \pi d^2 + \pi d\left(O_2K_1 + \sqrt{R^2 - \left(\frac{d+G}{2}\cdot\cos\theta\right)^2} - \frac{d+G}{2}\cdot sin\theta\right) \quad \text{Eq. 3.12}$$

For the linked Au-Ag geometries in Figure 3.17C and Figure 3.17D, because only Au is catalytically active, we calculated the surface area of only the Au nanorod within the observation circle. Similarly, as we did above, for that in Figure 3.17C, we get:

$$S_C = \frac{\pi d^2}{2} + \pi d\cdot KM = \frac{\pi d^2}{2} + \pi d\cdot(CK - CM) = \frac{\pi d^2}{2} + \pi d\cdot\left(R - \frac{d+G}{2}\right) \quad \text{Eq. 3.13}$$

And

$$S_D = \pi d\cdot K_1K_2 = \pi d\cdot 2M_1K_2 = \pi d\cdot 2\sqrt{R^2 - \left(\frac{d+G}{2}\right)^2} \quad \text{Eq. 3.14}$$

3.7.2. Validation of approximation via numerical surface integration

To verify the above surface area approximations for the cylinder portion of the nanorods, we applied a surface integral of intersection of two cylinders to obtain the exact surface areas of the nanorods within the observation circle (Figure 3.18A). Specifically, the bigger cylinder in Figure 3.18A is the observation circle whose diameter can be 80 nm, 140 nm or 200 nm. The smaller one is a Au nanorod. The purpose here is to calculate the surface area of the smaller cylinder within the intersection with the bigger cylinder.

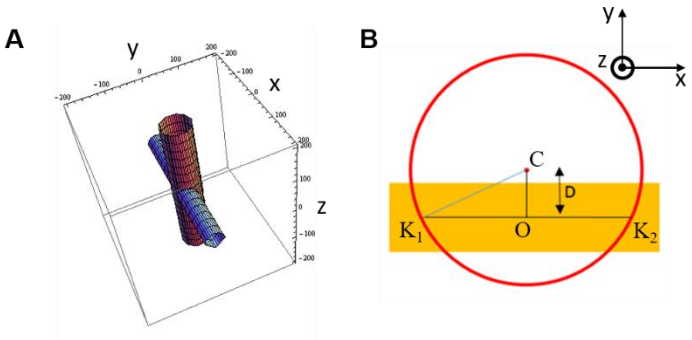

Figure 3.18. Surface integral of intersection to calculate the exact surface area of nanorod in an observation circle. (**A**) The intersection model of surface area calculation. One smaller cylinder along the *x*-axis represents the nanorod; the other bigger cylinder along the *z*-axis represents the observation circle, with the distance between the two axes being *D*. (**B**) Cross section of the model in A in the *xy* plane. Red circle represents the observation circle. Yellow rectangle represents the gold nanorod.

Figure 3.18A presents a common scenario where the smaller cylinder (radius *r*) goes through the bigger cylinder (radius *R*) in a perpendicular manner, oriented long the *x*- and *z*-axis, respectively. The distance between the central axes of Au nanorod and observation circle is *D*. In three-dimensional space, we set the center position of Au nanorod as the origin (O in Figure 3.18B). Then, the surface of the two cylinders follow these equations,

respectively:

$$\begin{cases} y^2 + z^2 = r^2 \\ x^2 + (y - D)^2 = R^2 \end{cases} \quad \text{Eq. 3.15}$$

Then, we have:

$$\begin{cases} x = \pm\sqrt{R^2 - (\sqrt{r^2 - z^2} - D)^2} \\ y = \pm\sqrt{r^2 - z^2} \end{cases} \quad \text{Eq. 3.16}$$

In order to calculate the surface area of the Au nanorod (smaller cylinder) inside the intersection of two cylinders, we used the method described by Weisstein[24]. The intersected surface area can be calculated by the surface integral as:

$$S_{int} = 8\int_0^r \sqrt{R^2 - (\sqrt{r^2 - z^2} - D)^2}\,\frac{r}{\sqrt{r^2 - z^2}}\,dz \quad \text{Eq. 3.17}$$

Specially, if $D = 0$, we can calculate the analytical solution of Equation Eq. 3.17:

$$S_{int} = 8r\sqrt{R^2 - r^2}\,\text{EllipticE}\left[\frac{r^2}{r^2 - R^2}\right] \quad \text{Eq. 3.18}$$

in which "EllipticE" is the complete elliptic integral which can be solved numerically. Otherwise, if $D \neq 0$, we can calculate the numerical integration of S_{int} after knowing the *r, R, D* values.

Meanwhile, we can also estimate the surface area of Au nanorod inside in the observation circle in Figure 3.18B. In this model, intersected surface area of nanorod is estimated by calculating surface area of cylinder with the same diameter of nanorod and with length of K_1K_2, similarly as in Equation Eq. 3.14. Hence the approximation surface area is:

$$S_{ap} = 4\pi r\sqrt{R^2 - D^2} \quad \text{Eq. 3.19}$$

By using the two methods above and applying the size of nanorod, observation circle, and D = 15 nm (i.e., assuming a gap size of 5 nm, close to the smallest gap size we experimentally observed), we have:

Table 3.2. Surface area difference from integral calculation and approximation with a gap size of 5 nm.

R (nm)	40	70	100
Integral calculation (nm^2)	6154.1	10905.7	15657.2
Approximation (nm^2)	5824.5	10739.8	15529.8
Error (%)*	5.36	1.52	0.81

* Error (%)= | (Integral calculation) – (Approximation) | / (Integral calculation) ×100%

By using the two methods above and applying the size of nanorod, observation circle and D = 20 nm (i.e., assuming a gap size of 15 nm, close to the largest gap size we experimentally observed), we have:

Table 3.3. Surface area difference from integral calculation and approximation with a gap size of 15 nm.

R (nm)	40	70	100
Integral calculation (nm^2)	5957.4	10814.2	15581.7
Approximation (nm^2)	5441.4	10537.2	15390.6
Error (%)	8.66	2.56	1.22

In summary, the value difference of surface area from integral calculation and approximation is always less than 10%. When we chose 70nm as the radius of observation circle to evaluate specific activity of Au nanorods, the error was even less than 3%. Therefore, it is reasonable to approximately calculate surface area of catalysts by using Equation Eq. 3.11 and Eq. 3.12.

Hence, the value difference of surface area from integral calculation and

approximation is always less than 10%. When we chose 70 nm as the radius of observation circle to evaluate specific activity of Au nanorods, the error was even less than 3%. Therefore, it is reasonable to approximately calculate surface area of catalysts by using Equations Eq. 3.11 or Eq. 3.12 for linked Au-Au nanorods structures and Equations Eq. 3.13 or Eq. 3.14 for linked Au-Ag nanorod-nanoparticle structures, which were used for calculating the specific activities reported in the main text.

3.8. Specific turnover rate follows a second order dependence on the excitation light power density.

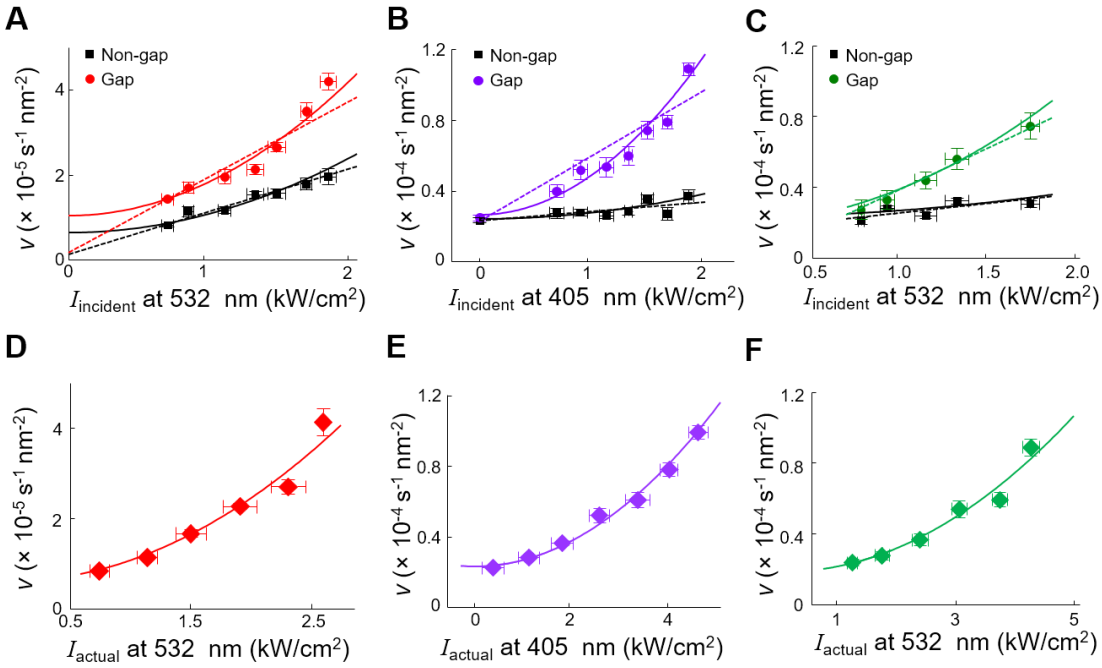

Figure 3.19. Comparison between the linear and quadratic fittings on the specific activity vs. local incident power density or local actual power density. The data presented here are the same as Fig. 1.6 in the Chapter 1, but only the binned and averaged data points are reporudced here. Fitting

parameters are summarized in Table 2.4. (**A**) Specific turnover rates v of linked Au-Au nanorods at gap and non-gap regions vs. their local incident light power density $I_{incident}$ at 532 nm. Solid lines: quadratic fits; dashed lines: linear fits (**B**) Same as A, but for linked Au-Ag nanorod-nanoparticle structures and for 405 nm light. (**C**) Same as B, but for 532 nm light. (**D-F**) Corresponding to A-C respectively, in which the incident local light power density has been converted to the actual local power density using the electric field enhancement factor obtained from FDTD simulations. x error bars are s.d.; y error bars are s.e.m.

Table 3.4. Comparisons of fitting parameters from Figure 2.19. All linear fittings use the equation $v = A_L + B \cdot I$, while all quadratic fittings use the equation $v = A_Q + C \cdot I^2$, in which v is the specific turnover rate and I is the power density. In all cases, the quadratic fitting has a higher R^2 value (green numbers) than the corresponding linear fitting, indicating that the second order relationship between activity and light power density fits the data better. Note both fittings are two-parameter fits; so, the degrees of freedoms are the same. Moreover, for the linear fits, A_L, which corresponds to the extrapolated specific activity at zero light illumination sometimes becomes negative for the gap region, further supporting the unreasonableness/inadequacy of the linear fits. Furthermore, the specific turnover rates of the gap regions fall on the same curve as those for the non-gap regions as a function of increasing actual local power density in all cases (red numbers). These results further demonstrate that the underlying mechanism of the plasmonic catalytic enhancement involves two photoexcited species.

		Gap (local power density)	Non-gap (local power density)	Actual power density
Au-Au 532nm	A_Q($\times10^{-5}$ s^{-1} nm^{-2})	1.04±0.06	0.64±0.06	0.61±0.06
	C ($\times10^{-1}$ m^2 W^{-2} s^{-1})	0.89±0.08	0.49±0.05	0.50±0.03
	R_Q^2	0.961	0.942	0.976
	A_L($\times10^{-5}$ s^{-1} nm^{-2})	-0.39±0.45	0.23±0.11	N/A
	B ($\times10^{6}$ W^{-1} s^{-1})	2.39±0.35	0.99±0.08	
	R_L^2	0.921	0.862	
Au-Ag 405nm	A_Q($\times10^{-5}$ s^{-1} nm^{-2})	2.56±0.22	2.39±0.15	2.29±0.09
	C ($\times10^{-1}$ m^2 W^{-2} s^{-1})	2.55±0.16	0.38±0.11	0.42±0.02
	R_Q^2	0.973	0.617	0.936
	A_L($\times10^{-5}$ s^{-1} nm^{-2})	0.16±0.08	0.23±0.28	N/A
	B ($\times10^{6}$ W^{-1} s^{-1})	0.43±0.67	0.61±0.22	
	R_L^2	0.853	0.452	
Au-Ag 532nm	A_Q($\times10^{-5}$ s^{-1} nm^{-2})	1.64±0.28	2.27±0.37	1.95±0.22
	C ($\times10^{-1}$ m^2 W^{-2} s^{-1})	2.23±0.20	0.34±0.02	0.39±0.03
	R_Q^2	0.968	0.491	0.962
	A_L($\times10^{-5}$ s^{-1} nm^{-2})	-1.29±0.25	1.68±0.61	N/A
	B ($\times10^{6}$ W^{-1} s^{-1})	5.30±0.22	0.92±0.52	
	R_L^2	0.954	0.349	

REFERENCES

(1) Jana, N. R.; Gearheart, L.; Murphy, C. J. *J. Phys. Chem. B* **2001**, *105*, 4065.

(2) Wang, Z. L.; Mohamed, M. B.; Link, S.; El-Sayed, M. A. *Surf. Sci.* **1999**, *440*, L809.

(3) Zhou, X.; Andoy, N. M.; Liu, G.; Choudhary, E.; Han, K.-S.; Shen, H.; Chen, P. *Nat. Nanotechnol.* **2012**, *7*, 237.

(4) Caswell, K. K.; Wilson, J. N.; Bunz, U. H. F.; Murphy, C. J. *J. Am. Chem. Soc.* **2003**, *125*, 13914.

(5) Stöber, W.; Fink, A.; Bohn, E. *J. Colloid Interface Sci.* **1968**, *26*, 62.

(6) Andoy, N. M.; Zhou, X.; Choudhary, E.; Shen, H.; Liu, G.; Chen, P. *J. Am. Chem. Soc.* **2013**, *135*, 1845.

(7) Aliaga, C.; Park, J. Y.; Yamada, Y.; Lee, H. S.; Tsung, C.-K.; Yang, P.; Somorjai, G. A. *J. Phys.*

Chem. C **2009**, *113*, 6150.

(8) Zhou, X.; Choudhary, E.; Andoy, N. M.; Zou, N.; Chen, P. *ACS Catalysis* **2013**, *3*, 1448.

(9) Djokić, S.; Nikolić, N.; Živković, P.; Popov, K.; Djokić, N. *ECS Trans.* **2011**, *33*, 7.

(10) Kuzuya, A.; Numajiri, K.; Kimura, M.; Komiyama, M. *Nucleic Acids Symp Ser (Oxf)* **2008**, 681.

(11) Xiaoge, H.; Wenlong, C.; Tie, W.; Erkang, W.; Shaojun, D. *Nanotechnology* **2005**, *16*, 2164.

(12) Paramelle, D.; Sadovoy, A.; Gorelik, S.; Free, P.; Hobley, J.; Fernig, D. G. *Analyst* **2014**, *139*, 4855.

(13) Awazu, K.; Fujimaki, M.; Rockstuhl, C.; Tominaga, J.; Murakami, H.; Ohki, Y.; Yoshida, N.; Watanabe, T. *J. Am. Chem. Soc.* **2008**, *130*, 1676.

(14) Xu, W.; Kong, J. S.; Yeh, Y.-T. E.; Chen, P. *Nat. Mater.* **2008**, *7*, 992.

(15) Thompson, R. E.; Larson, D. R.; Webb, W. W. *Biophys. J.* **2002**, *82*, 2775.

(16) Yildiz, A.; Forkey, J. N.; McKinney, S. A.; Ha, T.; Goldman, Y. E.; Selvin, P. R. *Science* **2003**, *300*, 2061.

(17) D Axelrod; T P Burghardt, a.; Thompson, N. L. *Annu. Rev. Biophys. Bioeng.* **1984**, *13*, 247.

(18) Saleh, B. E. A.; Teich, M. C. *Fundamentals of Photonics*; Wiley, 2007.

(19) Firoozabadi, A.; Ghorayeb, K.; Shukla, K. *AIChE J.* **2000**, *46*, 892.

(20) Govorov, A. O.; Richardson, H. H. *Nano Today* **2007**, *2*, 30.

(21) Su, L.; Yuan, H.; Lu, G.; Rocha, S.; Orrit, M.; Hofkens, J.; Uji-i, H. *ACS Nano* **2016**, *10*, 2455.

(22) Zheng, Z.; Tachikawa, T.; Majima, T. *J. Am. Chem. Soc.* **2015**, *137*, 948.

(23) https://kb.lumerical.com/en/ref_sim_obj_planewave_circular_polarization.html.

(24) In *Handbook of Optical Constants of Solids*; Academic Press: Burlington, 1997, p xv.

(25) Weisstein, E. W. *"Steinmetz Solid." From MathWorld--A Wolfram Web Resource*. http://mathworld.wolfram.com/SteinmetzSolid.html.

4. LONG-RANGE CATALYTIC COMMUNICATIONS WITHIN AND BETWEEN SINGLE NANOCATALYSTS

4.1. INTRODUCTION

Enzymes often show catalytic allostery in which reactions occurring at different sites communicate over a distance up to a few nanometers[1]. Here we report that phenomenologically similar, but mechanistically distinct, effects also exist in non-biological nanoparticle catalysts. Using spatiotemporally resolved single-molecule catalysis imaging, we find that catalytic reactions on a single Pd or Au nanocatalyst can communicate with each other, likely via hopping of positively-charged holes on the catalyst surface, over ~10^2 nanometers and with a temporal memory of ~10^1 to 10^2 seconds, giving rise to positive cooperativity among its surface active sites. Catalytic communication is also present between individual nanocatalysts, but operates via a molecular diffusion mechanism involving negatively-charged product molecules, and its communication distance is many microns. Generalization of these long-range intraparticle and interparticle catalytic communications may introduce a novel conceptual framework in understanding nanoscale catalysis.

A distinguishing feature of enzymes, or proteins broadly, is (catalytic) allostery, in which the binding or catalytic conversion of a substrate at one site affects the binding or catalysis at another site without direct interactions between the two substrates[2,3]. What underlies allostery fundamentally is the communication via local and global structural changes mediated by covalent bonds and intermolecular interactions that can connect active sites as far as a few nanometers apart. On the other hand, enzymes are not the only nanoscale

catalysts. Similar in size to enzymes, nanoparticles of various materials, such as metals or metal oxides, can catalyze many chemical transformations on their surfaces[4-8] and their surface active sites can be structurally or electronically coupled. Can reactions at different surface sites on the same nanocatalyst communicate with each other, as in allosteric enzymes?

Here we show they do, by analyzing the correlation between temporally subsequent reactions occurring at different locations *within* single nanocatalysts, resolved spatiotemporally using single-molecule fluorescence localization microscopy[9-12]. This intraparticle catalytic communication, a first-of-its-kind discovery, occurs in three Pd or Au based nanocatalysts and in three distinct catalytic reactions including a photo-induced disproportionation reaction, an oxidative deacetylation reaction, and a reductive deoxygenation reaction. And the communication reaches over ~10^2 nanometers with a temporal memory of ~10^1 to 10^2 seconds, leading to positive cooperativity among surface sites *within* a single nanocatalyst. We further observe a similar phenomenon *between* individual Au nanocatalysts in catalyzing the deacetylation and deoxygenation reactions, with communication distances of many microns, but *not* between Pd nanocatalysts in catalyzing the photo-induced disproportionation reaction. Using solution flow, electric field, and chemical manipulations, we show that the interparticle catalytic communication, if occurring, operates via a molecular diffusion mechanism, involving negatively-charged product ions that act as catalytic promoters. In contrast, the intraparticle catalytic communication operates via a distinct mechanism, involving positively-charged messengers, likely through hopping of surface holes localized on metal-oxide species. This intraparticle catalytic communication, phenomenologically similar and conceptually

analogous to enzyme cooperativity, could represent a novel perspective in understanding nanocatalysis.

4.2. METHOD

4.2.1. Catalysts.

Catalyst preparations are described in Supplementary Section 5.1, and characterizations summarized in Supplementary Section 5.1. Pd nanorods are 37.4 ± 4.8 nm in diameter and 559 ± 223 nm in length, and are likely 5-fold twinned nanostructures[13]. Au nanorods[11,29] have lengths of ~100-700 nm and diameters of 21.4 ± 3.2 nm, and are either multiply twinned crystals or single crystals[30-34]. The triangular- and hexagonal-shaped Au nanoplates[23,35] are single crystals with edge length of ~10-1000 nm and thickness of 13.7 ± 0.7 nm. All were later coated with a mesoporous silica shell[11,23,36,37] (~40-120 nm thick). This shell allows for subsequent calcination or UV/ozone treatment to remove the organic ligands on the metal surfaces, while still maintaining the morphologies of nanocatalysts and preventing their aggregation. The reactants can still access the metal surface for catalysis through the mesopores, and the mass transport of the reactants to the metal surface does not limit the catalytic kinetics because the catalytic conversion is slow, as we demonstrated previously on Au-based nanocatalysts[11,23]. This shell also helps trapping the fluorescent product molecules temporarily (e.g., via adsorption onto silica surface sites in the mesopores), facilitating their detection, as well as circumventing the potential fluorescence quenching associated with direct detection on metal surfaces. For the mSiO_2-coated Pd nanorods, calcination led to a mostly oxidized Pd surface, and $NaBH_4$ was used to reduce it

for later catalysis studies.

4.2.2. Catalytic reactions.

The Pd-nanorod-catalyzed photo-induced disproportionation reaction of resazurin was assayed first at the ensemble level and determined to have a 3:1 resazurin to resorufin stoichiometry (Supplementary Section 5.2). We previously showed[11,23] that Au-based nanocatalysts are active[11] in catalyzing the oxidative deacetylation of amplex red by H_2O_2 to generate resorufin, acetate, and water[38], and the reductive deoxygenation of resazurin by NH_2OH to generating resorufin and nitrite, which was detected and quantified by the colorimetric Griess reaction[39]. The metal particles are the active catalyst component, while the $mSiO_2$ shell is not. The reaction conditions are in Supplementary Section 5.2 and are all in buffered pH 7-9 conditions for imaging.

4.2.3. Single-molecule fluorescence microscopy and nanometer-precision mapping of fluorescent products.

Catalysis on individual nanocatalysts was imaged using single-molecule fluorescence microscopy[9-12,19,40-43], based on a total internal reflection fluorescence microscope, at room temperature under ambient conditions (Supplementary Figure 4.3), as described[11,23]. A continuous-wave circularly polarized 532 nm laser induced the fluorescence of the product resorufin generated on immobilized nanocatalysts on a slide in a microfluidic reactor. For the Pd-nanorod-catalyzed disproportionation reaction, this 532 nm laser also drives the catalytic reaction. The aqueous reactant solutions were supplied into the reactor continuously and in large excess compared with the reactant consumption rates to give

steady-state reaction kinetics, in which the kinetics were rate-limited by catalytic conversions from the reactants to the products rather than by mass transport, as we determined previously (for Au-based nanocatalysts)[11,22,23]. The fluorescence of the product resorufin was imaged at the single-molecule level by an EMCCD camera up to 25 ms frame rate. The images were then analyzed using a custom MatLab program[11] to localize the positions of individual fluorescent product molecules on individual nanocatalysts to about 35-45 nm precision, in correlation with the nanocatalyst's SEM image (Supplementary Section 5.4 and Supplementary Figure 5.4).

4.2.4. Solution flow and voltage manipulations.

The steady reactant solution flow into the microfluidic reactor was varied from ~5 to 100 μL min^{-1} (linear flow rates of ~100 to 2000 μm s^{-1}, depending on the cross section of the particular reactor). For voltage manipulations, two electrodes were used to apply a voltage of −1.2 to 1.2 V across the microfluidic reactor of 5-8 mm in width in the xy imaging plane perpendicular to the solution flow direction (Figure 4.4a). Because of the applied voltage and a continuous solution flow (the latter makes the microfluidic reactor a nonequilibrium solution system), a steady-state electrical current was achievable at each applied voltage (Supplementary Figure 5.24), which ensured a finite electric field inside the microfluidic reactor, even though the solution contained >100 mM buffer. Using copper or platinum electrodes gave similar results (Supplementary Figure 5.24).

4.2.5. Anion and cation effects.

Various concentrations of acetate and nitrite anions were titrated into the reaction solution

for the Au-nanocatalyst catalyzed deacetylation and deoxygenation reactions, respectively. At the ensemble level, the initial reaction rate was monitored by following the fluorescence signal of the reaction product resorufin (Supplementary Figure 5.25); here 5 nm Au nanoparticles were used as representative Au nanocatalysts because of their size homogeneity compared with the heterogeneous Au nanorod and nanoplate samples, which contain many different shapes of particles. We further measured the effect of acetate and nitrite on Au nanorod catalysis at the single-particle level (Supplementary Figure 5.26). The spectator cations were varied by varying the buffer concentrations, which use them as counter cations.

4.3. RESULTS

4.3.1. Single-molecule super-resolution mapping of photocatalysis on Pd nanorods

We synthesized penta-twinned crystalline Pd nanorods[13] of ~37 nm in width and ~200-1200 nm in length as a model pseudo-1-dimensional nanocatalyst (Figure 4.1a, Supplementary Figure 5.1a-d; Methods). We found they could catalyze the photo-induced disproportionation of resazurin[14,15] to generate the 2-electron-reduced fluorescent resorufin under 532 nm light illumination (Figure 4.1b, top). The reaction rate is appreciable only when the Pd nanorods and the 532 nm light are both present, whereas the un-catalyzed reaction is much slower (Supplementary Figure 5.2). The reaction stoichiometry between resazurin and resorufin is 3:1; the corresponding oxidized product of this disproportionation is likely two equivalents of 1-electron-oxidized neutral radical species from resazurin[14], which likely will further react to form other species. We further encapsulated these Pd nanorods with ~125 nm thick mesoporous silica (i.e., $mSiO_2$, Figure 4.1a). This

encapsulation allows for calcination to remove their organic surfactants while maintaining their morphology and stability, and the reactants can still access the Pd surface for catalysis via the mesopores.

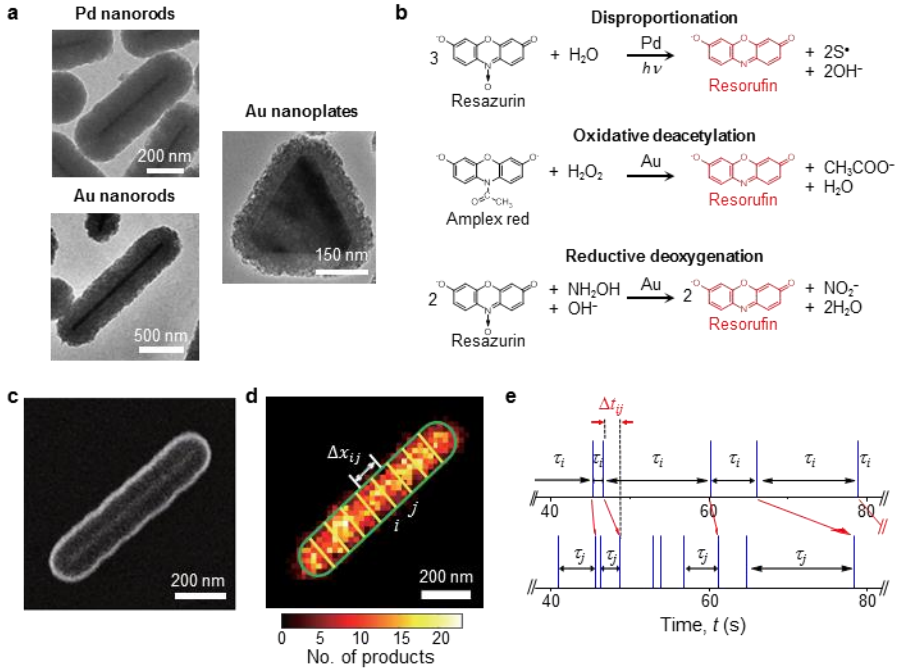

Figure 4.1. Real-time single-molecule super-resolution mapping of catalytic reactions on single nanocatalysts. **a,** TEM images of Pd nanorods, Au nanorods, and Au nanoplates encapsulated in mesoporous silica. **b**, Three fluorogenic Pd- or Au-nanoparticle catalyzed reactions. S•: one-electron oxidized neutral radical species from resazurin disproportionation[14]. **c**, SEM image of a $mSiO_2$-coated Pd nanorod. **d**, Two-dimensional histogram of >6000 fluorescent product molecules in 25^2 nm^2 bins from the Pd nanorod in **c**, mapped onto its SEM structural contour (green line). Yellow lines dissect the nanorod into ~100 nm segments. Δx_{ij}: center-to-center distance between segments *i* and *j*. **e**, Catalytic event sequences from segment *i* and *j* in **d**. In each sequence, the individual product generation events (vertical lines) are plotted against the time when they are detected. The microscopic reaction time τ for each product generation is the time separation from the previous one in the same sequence. Pairs of temporally subsequent reactions from segment *i* to *j* are linked by red

arrows, each pair with a time separation Δt_{ij}.

4.3.2. Long-range *intra*particle catalytic communication *within* single Pd nanorods

The mapping of individual products allowed us to dissect each Pd nanorod, as well as its catalytic product positions, into segments (e.g., ~100 nm length, greater than the ~40 nm product localization uncertainty, Figure 4.1d). For each segment, we extracted the temporal sequence of product generation events (Figure 4.1e), in which the time separation τ of any event from the previous one is the microscopic reaction time for generating this product at the respective segment. This τ is probabilistic, and $\langle \tau \rangle^{-1}$, where $\langle\ \rangle$ denotes averaging, is the rate of catalytic turnovers for that segment.

To probe whether catalytic reactions at different sites can communicate with each other within a single Pd nanorod, we computed the Pearson's cross-correlation coefficient ρ_{τ_i,τ_j} between the microscopic reaction time τ_i of any catalytic event at a segment *i* and the τ_j of the *immediate subsequent* event at another segment *j* ($j \neq i$) on the same nanorod (Figure 4.1e; Eq. 5.4). For any two segments *i* and *j*, ρ_{τ_i,τ_j} is a statistical property averaged over the many pairs of temporally neighboring catalytic events, in which the event pairs have the distance separation Δx_{ij} and an average time separation $\overline{\Delta t_{ij}}$. This ρ_{τ_i,τ_j} is a quantitative measure of how the microscopic reaction kinetics, reflected by τ, of any catalytic event at one location is correlated with that of a *subsequent* event at a *different* location.

Pooling results from >40 Pd nanorods, ρ_{τ_i,τ_j} shows striking *trends*: it starts being positive and decays exponentially with increasing intraparticle distance separation between the segments or increasing average time separation between temporally subsequent events,

approaching a residual value of ~0.03, even though the amplitude is small, ~0.05 (Figure 4.2 a-b, red). These trends suggest that reactions within a single Pd nanorod do communicate with each other: a reaction with a short τ (i.e., a fast reaction) at one segment tends to be followed by another fast reaction nearby, giving rise to a phenomenological positive cooperativity.

Moreover, when the temporal sequence, the locations, or both of the catalytic events are randomized, these trends of ρ_{τ_i,τ_j} vanish and it stays flat at a residual value of ~0.03 (Figure 4.2a-b, blue; Supplementary Section 5.7). Simulated random catalytic events also do not show these trends; ρ_{τ_i,τ_j} there stays flat at a similar residual value, indicating that this residual is some spurious contribution to the cross correlations (Supplementary Section 5.8). Control experiments show that rebinding of product resorufin to the nanorods contributes merely ~0.3% of the detected events, and it does not give these trends either (Supplementary Figure 5.12). Therefore, this intraparticle catalytic communication of Pd nanorods is specific to the spatiotemporal relations of the individual catalytic reactions on each nanorod.

Strikingly, the exponential distance decay constant x_0^{intra} of ρ_{τ_i,τ_j} is ~225 nm (Table 4.1), reflecting an intraparticle catalytic communication distance that is ~100× longer than that in allosteric enzymes, whose allosteric sites are typically a few angstroms to nanometers apart. (Note this distance is also much larger than both the ~40 nm product localization uncertainty and the ~100 nm segment size.) The exponential time decay constant t_0^{intra} of ρ_{τ_i,τ_j} is ~28 s (Table 4.1), reflecting a temporal memory of this catalytic communication. Both x_0^{intra} and t_0^{intra} are independent of the reactant concentration (Figure 4.2c) and the

laser power (Supplementary Figure 5.13a-b), supporting that they are not determined by reaction conditions, but rather characteristic to these Pd nanorods.

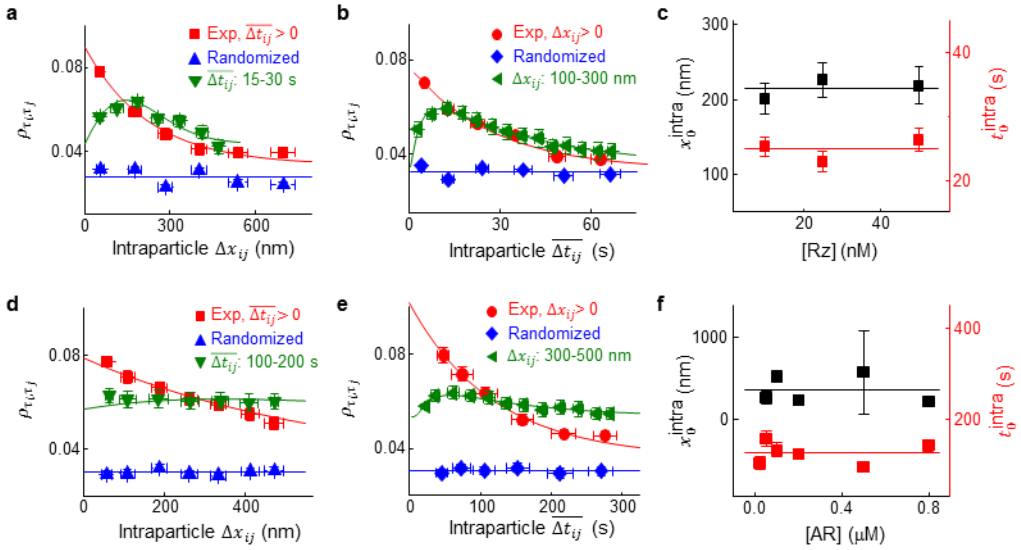

Figure 4.2. *Intra*particle catalytic communication within single Pd and Au nanocatalysts. a-b, For Pd nanorods catalyzing the photo-induced resazurin disproportionation: Pearson's cross-correlation coefficient $\rho_{\tau_i,\tau_j}(\Delta x_{ij}, \overline{\Delta t_{ij}})$ vs. the intraparticle distance separation Δx_{ij} (**a**) or the average time separation $\overline{\Delta t_{ij}}$ (**b**) of temporally subsequent reactions at two different segments on the same nanorod (red symbols), and after spatial (**a**) or temporal (**b**) randomization of catalytic events (blue symbols), and when $\overline{\Delta t_{ij}}$ or Δx_{ij} is constrained (green symbols). Data averaged over >230 segments from >40 Pd nanorods. Red lines: exponential fits; blue lines: horizontal fits; green lines: fits with Equations Eq. 5.16 and Eq. 5.22; fitting parameters summarized in Table 4.1 and Supplementary Table 5.2. **c**, x_0^{intra} and t_0^{intra} vs. the reactant resazurin concentration. Lines: horizontal fits. **d-f**, Same as **a-c** but for Au nanorods catalyzing amplex red deacetylation. Data averaged over >1100 segments from >220 Au nanorods. Corresponding data for Au nanorods and nanoplates catalyzing resazurin deoxygenation are in Supplementary Figure 5.15 and Figure 5.17. x error bars are all s.d.; *y* error bars are s.e.m. in **a-b** and **d-e**, and s.d. in **c** and **f**.

Table 4.1. Key parameters of intraparticle and interparticle catalytic communication behaviors*

		Pd nanorods	Au nanorods		Au nanoplates
		Rz disproportion.	AR deacetyl.	Rz deoxygen.	Rz deoxygen.
Intra-particle	x_0^{intra} (nm)	225 ± 20	516 ± 160	624 ± 180	130 ± 22
	t_0^{intra} (s)	27.5 ± 2.4	128 ± 32	168 ± 36	5.5 ± 0.7
	D_{eff} ($\times 10^{-15}$ m^2 s^{-1})	0.92 ± 0.08	1.1 ± 0.4	1.2 ± 0.4	0.77 ± 0.17
	Charge of messenger	positive	positive	positive	n/d
Inter-particle	x_0^{inter} (μm)	n/a	10.5 ± 3.3	9.3 ± 2.4	11.5 ± 0.7
	t_0^{inter} (s)	n/a	18.1 ± 3.8	7.7 ± 1.4	6.2 ± 0.6
	Charge (and identity) of messenger	n/a	negative (CH_3COO^-)	negative (NO_2^-)	n/d

* Results are overall averages taking into account of all experiments, including solution flow manipulations, voltage manipulations, reactant concentration variations, and various batches of nanocatalyst samples. A more comprehensive table of parameters is in Supplementary Table 5.2. Rz: resazurin; AR: amplex red.

4.3.3. Generality of *intra*particle catalytic communication across nanocatalysts and reactions

We further studied Au nanorods of ~21 nm in diameter and ~100-700 nm in length, encapsulated in $mSiO_2$, as another pseudo-1-dimensional nanocatalyst (Figure 4.1a)[11]. We examined them in catalyzing two distinct reactions: the oxidative deacetylation of the nonfluorescent amplex red to the fluorescent resorufin by H_2O_2 and the reductive deoxygenation of resazurin to resorufin by NH_2OH (Figure 4.1b, middle and bottom), which we have studied previously[11,22]. The intraparticle catalytic communication is observed in both reactions: the exponential decay trends are clear for the positive cross-correlation

coefficients ρ_{τ_i,τ_j} with increasing intraparticle distance and average time separations between temporally subsequent reactions; these trends again vanish when the catalytic events are temporally or spatially randomized (Figure 4.2d-e, red and blue). The catalytic communication distance x_0^{intra} and temporal memory t_0^{intra} here are ~516 nm and ~128 s for the deacetylation reaction, and ~624 nm and ~168 s for the deoxygenation reaction, respectively (Table 4.1).

Using the Au nanorod catalyzed deacetylation reaction as an example, we found that both x_0^{intra} and t_0^{intra} are independent of the experimental time resolution, segmentation size, laser intensity, and nanorod's catalytic activity, as well as of the fluorescence-intensity-threshold in analyzing the single-molecule fluorescence images (Supplementary Figure 5.19 to Figure 5.23). They also show no dependence on the reactant concentration (Figure 4.2f), further supporting that these intraparticle catalytic communication distances and temporal memories are characteristic to the nanocatalysts.

We further studied $mSiO_2$-coated Au nanoplates of ~14 nm in thickness and up to ~1 μm in edge length as a pseudo-2-dimensional nanocatalyst (Figure 4.1a)[23] in catalyzing the deoxygenation of resazurin. Again, the exponential decay trends of ρ_{τ_i,τ_j} are clear (Supplementary Figure 5.17a-c). The catalytic communication distance x_0^{intra} and temporal memory t_0^{intra} are ~130 nm and ~5.5 s (Table 4.1).

Altogether, the intraparticle catalytic communication, *observed for the first time here*, is general across different nanocatalysts (i.e., Pd and Au), different reactions (disproportionation, deacetylation, and deoxygenation), and different nanocatalyst morphologies (1-dimensional nanorods and 2-dimensional nanoplates) studied here.

4.3.4. *Inter*particle catalytic communication: non-universal

The above discovery of intraparticle catalytic communication prompted us to examine the cross-correlation between temporally subsequent reactions on *different* nanocatalysts. No interparticle catalytic communication is observed for Pd nanorods in catalyzing the photo-induced disproportionation reaction: the interparticle cross-correlation efficient ρ_{τ_i,τ_j} stays flat at the residual value of ~0.03 with increasing interparticle distance separation or average time separation between catalytic events, non-differentiable from those when the catalytic events are spatiotemporally randomized (Figure 4.3a-b).

In contrast, for Au nanorods in catalyzing the deacetylation reaction, interparticle catalytic communication indeed exists: ρ_{τ_i,τ_j} starts positive and decays exponentially with increasing interparticle distance and average time separations between catalytic events (Figure 4.3c-d, red). The communication distance x_0^{inter} is ~11 μm, tens of times longer than that of the intraparticle cases; the temporal memory t_0^{inter} is ~18 s. Similar behaviors are also clear for Au nanorods and Au nanoplates in catalyzing the deoxygenation of resazurin (Supplementary Figure 5.16a-b and Figure 5.17d-e). These interparticle cross-correlations between Au nanocatalysts all vanish when the catalytic events are spatiotemporally randomized (e.g., Figure 4.3c-d, blue), except for the residual spurious cross-correlation (~0.03), which is also present for simulated random catalytic events (Supplementary Figure 5.11h-i). Altogether, *inter*particle catalytic communication, with communication distance on the order of microns, occurs, but only to selected systems.

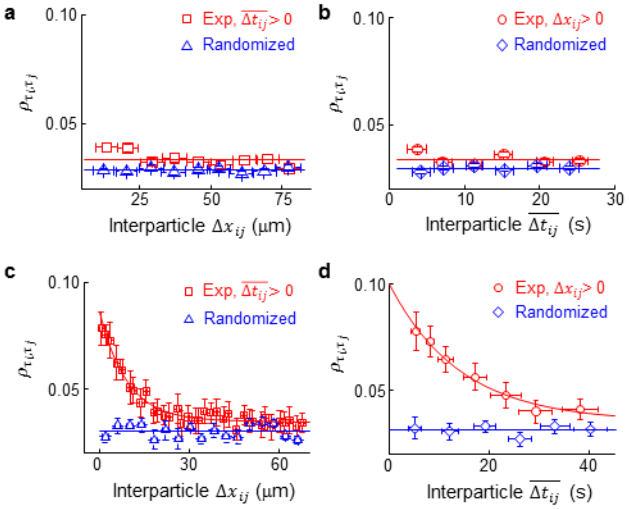

Figure 4.3. Non-universality of *inter*particle catalytic communication. **a-b**, For Pd nanorods catalyzing the disproportionation of resazurin. Pearson's cross-correlation coefficient $\rho_{\tau_i,\tau_j}(\Delta x_{ij}, \overline{\Delta t_{ij}})$ vs. the interparticle distance separation Δx_{ij} (**a**) or the average time separation $\overline{\Delta t_{ij}}$ (**b**) of temporally subsequent reactions at two different nanocatalysts (red symbols), and after spatiotemporal randomizations (blue symbols). Lines: horizontal fits. **c-d**, Same as **a-b** but for Au nanorods catalyzing the deacetylation of amplex red. Red lines: exponential fits; blue lines: horizontal fits; fitting parameters summarized in Table 4.1 and Supplementary Table 5.2. Corresponding data for Au nanorods and nanoplates catalyzing resazurin deoxygenation are in Figure 5.16 and Figure 5.17. x error bars are s.d.; *y* error bars are s.e.m.

4.3.5. Nature of *intra*particle catalytic messengers: positively-charged species universally

To probe the cause of intraparticle catalytic communication, we examined how solution flow, which supplies the reactants into the reactor, would affect it (Figure 4.4a inset). No difference was observed in the behaviors of the intraparticle ρ_{τ_i,τ_j} for any Pd or Au nanocatalyst catalyzed reactions with regard to the flow direction or rate (e.g., Figure 5.13

c). This independence is not surprising, as the catalysis occurs on the metal surfaces surrounded by a mesoporous silica shell, which could shield any flow effect on intraparticle behaviors.

We then applied a voltage across the reactor using two electrodes (which could affect any charged species) (Figure 4.4a), resulting in a steady-state electrical current perpendicular to the solution flow (Figure 5.24a). For Pd nanorods in catalyzing the disproportionation reaction, with increasing intraparticle distance, ρ_{τ_i,τ_j} decays slower when the intraparticle vector is pointed down the electric-field (EF) direction than that of upfield (Figure 4.4b). Moreover, the intraparticle communication distance x_0^{intra} shows cosinusoidal modulations vs. the orientation angle to the EF direction: they are larger for downfield directions than for upfield directions; and the modulation amplitude $\Delta x_{0,\text{EF}}^{\text{intra}}$ is positive and scales linearly with increasing voltage (Figure 4.4c-d). (No EF effect was observed on the temporal memory t_0^{intra}; e.g., Figure 5.18b.) Similar behaviors were observed for Au nanorods in catalyzing the deacetylation and the deoxygenation reactions (Figure 5.14a-c and Figure 5.15c-e). These trends indicate that the intraparticle catalytic communications in these three catalytic systems all involve *positively*-charged messenger species, which cause temporally neighboring reactions at different locations *within* a single nanocatalyst to correlate with each other and whose reach is facilitated down the EF direction.

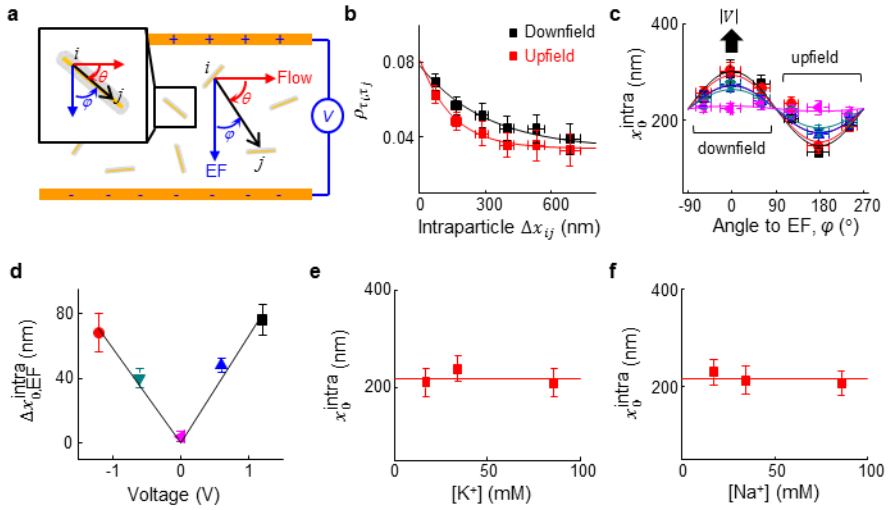

Figure 4.4. Nature of *intra*particle catalytic messenger for Pd nanorods catalyzing resazurin disproportionation (corresponding data for Au nanorods catalyzing the deacetylation and deoxygenation reactions in Figure 5.14 and Figure 5.15). **a**, Schematic of the microfluidic reactor in the *xy* imaging plane, and definitions of orientation angle θ of the interparticle and intraparticle (inset) *i*-to-*j* vector to the solution flow and angle φ to the electric field (EF) direction applied via two electrodes. **b**, $\rho_{\tau_i,\tau_j}(\Delta x_{ij}, \overline{\Delta t_{ij}})$ vs. Δx_{ij} when the *i*-to-*j* intraparticle vector is pointed downfield ($\varphi = 15 \pm 4°$) or upfield ($\varphi = 195 \pm 4°$) along the EF direction at 1.2 V. Lines: exponential fits with decay constant $x_0^{\text{intra}} = 302 \pm 19$ nm (downfield) or 148 ± 16 nm (upfield). **c**, Dependences of the intraparticle catalytic communication distance x_0^{intra} on the orientation angle relative to the EF direction at various voltages. Lines: fits with cosine function Eq. 5.1. **d**, Cosine function amplitude $\Delta x_{0,\text{EF}}^{\text{inter}}$ vs. voltage from **c**. Symbols color-coded as in **c**. Negative voltages indicate flipping electrode bias. **e-f**, x_0^{intra} vs. [K^+] or [Na^+] in the solution. Lines in **d-f**: linear eye-guides. *x* error bars are all s.d.; *y* errors bar are s.e.m. in **b**, and s.d. in **c-f**.

4.3.6. Mechanism of *inter*particle catalytic communication: diffusion of negatively-charged reaction products

Interparticle catalytic communication, although absent for Pd nanorods in catalyzing the disproportionation reaction, is clear for Au nanorods and nanoplates in catalyzing the deacetylation and deoxygenation reactions. As individual Au nanocatalysts are spatially separated from one another, a possible mechanism for their interparticle catalytic communication is that a reaction product desorbs from the Au surface of a nanocatalyst, diffuses out of the $mSiO_2$ shell and then through solution to affect reactions at a nearby nanocatalyst. This process would be related to the spillover effect in surface catalysis[20], and the solution part of molecular diffusion should be susceptible to the solution flow. We thus examined how solution flow would affect the interparticle catalytic communications of these Au nanocatalysts. Strikingly, for Au nanorods in catalyzing both the deacetylation and deoxygenation reactions, ρ_{τ_i,τ_j} decays slower with increasing interparticle distance when the interparticle vector is pointed downstream than that of upstream (e.g., Figure 4.5a). Moreover, the interparticle communication distances x_0^{inter} show cosinusoidal modulations vs. the orientation angle to the flow direction: they are larger for downstream directions than for upstream directions, and the modulation amplitudes $\Delta x_{0,\text{flow}}^{\text{inter}}$ scale linearly with increasing flow rate (e.g., Figure 4.5b-c). These trends indicate that these interparticle catalytic communications indeed occur via molecular diffusion, observed here *for the first time between individual nanocatalysts*, in which solution flow extends the communication distance.

We further examined how an applied voltage would affect the diffusing messenger

molecules that cause these interparticle communications. Down the EF direction, ρ_{τ_i,τ_j} decays faster with increasing interparticle distance than upfield in both the deacetylation and deoxygenation reactions (e.g., Figure 4.5d). The interparticle communication distances x_0^{inter} again show cosinusoidal modulations vs. the orientation angle to the EF direction: they are smaller for downfield directions than for upfield directions; the modulation amplitudes $\Delta x_{0,\text{EF}}^{\text{inter}}$ are thus *negative*, and scale linearly with increasing voltage (e.g., Figure 4.5e-f). These trends indicate that for both reactions, the diffusing messenger molecules for the interparticle catalytic communication between the Au nanocatalysts are *negatively*-charged species, whose motions are impeded down the EF direction, and whose charges are *opposite* to the intraparticle catalytic messengers that are universally observed for the Pd and Au nanocatalysts earlier.

As these interparticle catalytic communications between Au nanocatalysts are about an earlier reaction affecting positively the kinetics of a subsequent reaction, the negatively-charged messenger molecules must be reaction products that can act as promoters of the catalyzed reactions. For both the deacetylation and the deoxygenation reactions (Figure 4.1b), the negatively-charged, fluorescent product resorufin does not affect the reaction rate in either reaction (Figure 5.25b and d), and its binding to the nanocatalysts does not result in interparticle (or intraparticle) communication, either (Figure 5.12c-f). However, adding the product acetate (CH_3COO^-) or nitrite (NO_2^-) promotes the respective catalytic rate significantly; the rate eventually saturates, with the concentration at half saturation ($K_{1/2}$) being ~0.95 and 0.46 μM, respectively (e.g., Figure 4.5g). Moreover, adding acetate or

nitrite quenches the interparticle catalytic communication distance x_0^{inter}: it decreases asymptotically with $K_{1/2}$'s comparable to those in the catalysis promotion effect (e.g., Figure 4.5h). These results support that acetate and nitrite are the respective messenger molecules, which, once generated at one nanocatalyst, diffuse away to reach another nanocatalyst, perhaps helping either activate the reactants or stabilize intermediates there, leading to interparticle catalytic communication among the Au nanocatalysts.

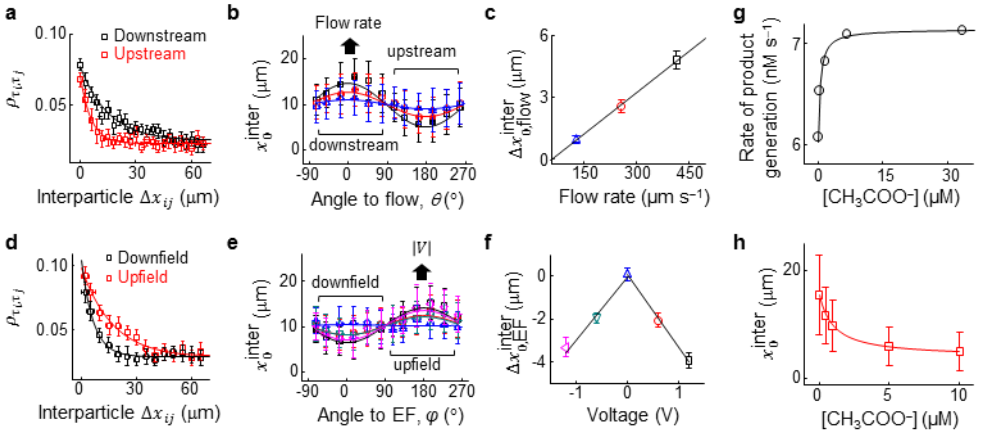

Figure 4.5. Mechanism of *inter*particle catalytic communication for Au nanorods catalyzing deacetylation reaction (corresponding data for the deoxygenation reaction in Supplementary Figure 5.16). **a, d**, $\rho_{\tau_i,\tau_j}(\Delta x_{ij}, \overline{\Delta t_{ij}})$ vs. Δx_{ij} when the *i*-to-*j* interparticle vector is pointed downstream (θ = 14 ± 5°) or upstream (θ = 194 ± 5°) along the solution flow at 415 μm s^{-1} flow rate (**a**), or pointed downfield (φ = 15 ± 4°) or upfield (φ = 195 ± 4°) along the EF direction at 1.2 V (**d**). Lines: exponential fits. **b, e**, Dependences of the interparticle catalytic communication distance x_0^{inter} on the orientation angle relative to the flow direction at various flow rates (**b**) or to the EF direction at various voltages (**e**). Lines: fits with cosine function Eq. 5.1. **c, f**, Cosine function amplitude $\Delta x_{0,\text{flow}}^{\text{inter}}$ vs. flow rate from **b** (**c**), and amplitude $\Delta x_{0,\text{EF}}^{\text{inter}}$ vs. voltage from **e** (**f**). Symbols color-coded as in **b** and **e**. Negative voltages in **f** indicate flipping electrode bias. Lines: linear eye-guides. **g**, Initial

product formation rate vs. [CH_3COO^-] in the solution at the ensemble level. Single-particle level data are in Figure 5.26. Line: fit with saturation function Eq. 5.2, with $K_{1/2}$ = 0.95 ± 0.15 μM. **h**, x_0^{inter} vs. [CH_3COO^-]. Line: fit with saturation function Eq. 5.3 with $K_{1/2}$ = 0.99 ± 0.14 μM. *x* error bars in **a-b** and **d-e** are s.d. *y* error bars are s.e.m. in **a** and **d**, and s.d. in **b-c** and **e-h.**

4.4. DISCUSSION

Using real-time single-molecule super-resolution reaction mapping, we have uncovered catalytic communications within and between single nanocatalysts. The intraparticle catalytic communications occur universally across the Pd- and Au-based nanocatalysts and the three distinct catalytic reactions. The interparticle catalytic communications only occur to Au-based nanocatalysts in catalyzing the deacetylation and deoxygenation reactions, and they operate via a molecular diffusion mechanism, in which a negatively-charged reaction product (acetate or nitrite) acts a catalytic messenger to relate reactions on different nanocatalysts spatiotemporally. (The lack of such reaction products could be the reason for the absence of interparticle communication in Pd-nanorod-catalyzed disproportionation reaction.)

For the universal intraparticle catalytic communications here, they all involve a catalytic messenger that is positively-charged, opposite to that of the interparticle cases and suggesting a distinct underlying mechanism. Consistently, adding acetate or nitrite exerts no effect on the intraparticle x_0^{intra} of Au nanorods in catalyzing the deacetylation or deoxygenation reaction (e.g., Figure 5.14f), even though it quenches the corresponding interparticle x_0^{inter} (e.g., Figure 4.5h). Being positively-charged also rules out any process

that involves the negatively-charged product resorufin (e.g., its blinking, diffusion, or rebinding).

Moreover, none of the three reactions generates positively-charged products (Figure 4.1b). The spectator counter cations from the reactants and buffer (i.e., K^+ and Na^+) do not affect the intraparticle catalytic communications (e.g., Figure 4.4e-f) or the catalytic kinetics (e.g., Figure 5.13d-e) in our three systems. All reactions were done in slightly basic buffers (pH 7-9), making proton involvement less likely (more discussions in Section 5.16.4). Yet, the fact that all involve positively-charged messengers and all have comparable EF modulation amplitudes suggests a common mechanism underlying the intraparticle catalytic communications. As all reactions involve redox in an aerobic environment, we propose a hole migration mechanism on the surface of Pd or Au particles, which likely is not pure metal but present surface metal oxide species. In this mechanism, a localized surface hole (e.g., a positive charge on an oxidized metal atom) generated at one site hops diffusively to other sites on the same nanocatalyst, leading to intraparticle communication (see other disfavored possible mechanisms and more discussions; Section 5.15 and 5.16). The intraparticle catalytic communication distance x_0^{intra} would then correspond to the migration distance of this hole during a time reflected by the temporal memory t_0^{intra}. This mechanism is consistent with that hole migration can occur over long distances, depending on the material's conductivity and the presence of charge traps[24-27], and such charges can be long-lived[28]. This hole migration mechanism also should not operate between nanocatalysts due to their spatial separation. Using x_0^{intra} and t_0^{intra}, we computed the effective diffusion coefficient (D_{eff}) for this hole migration (Section 5.16.1). D_{eff}'s are all similar across all

systems (~10^{-15} m^2 s^{-1}, Table 4.1), further supporting a common underlying mechanism.

Provided the hole migration mechanism for the intraparticle catalytic communications, it is predictable that ρ_{τ_i,τ_j} should show a delayed maximum with increasing average time separation $\overline{\Delta t_{ij}}$, if Δx_{ij} is constrained to a specific intraparticle distance over which the hole needs to take time to migrate. This delayed maximum is indeed observed (e.g., Figure 4.2b, e, green) and is quantitatively interpretable by an effective diffusion model (Section 5.17). Similarly, a delayed maximum is predictable, and observed, for ρ_{τ_i,τ_j} with increasing intraparticle distance separation, if $\overline{\Delta t_{ij}}$ is constrained to a specific range during which the hole would migrate over a certain distance (e.g., Figure 4.2a, d, green).

As the intraparticle and interparticle catalytic communications are phenomenologically similar and conceptually analogous to cooperativity and synergism in enzymes, which are nature's most efficient catalysts, we envision that exploration of their generality and utility may bring new theoretical framework in understanding nanocatalysis.

REFERENCES

1 Fersht, A. *Structure and mechanism in protein science: A guide to enzyme catalysis and protein folding*. (W. H. Freeman and Company, 1998).

2 Changeux, J.-P. Allostery and the monod-wyman-changeux model after 50 years. *Annu. Rev. Biochem.* **41**, 103-133 (2012).

3 Cui, Q. & Karplus, M. Allostery and cooperativity revisited. *Protein Science* **17**, 1295-1307 (2008).

4 Tao, F. *et al.* Reaction-driven restructuring of rh-pd and pt-pd core-shell nanoparticles.

Science **322**, 932-934 (2008).

5 Bell, A. T. The impact of nanoscience on heterogeneous catalysis. *Science* **299**, 1688-1691 (2003).

6 Jaramillo, T. F. *et al.* Identification of active edge sites for electrochemical h_2 evolution from mos_2 nanocrystals. *Science* **317**, 100-102 (2007).

7 Hervés, P. *et al.* Catalysis by metallic nanoparticles in aqueous solution: Model reactions. *Chem. Soc. Rev.* **41**, 5577-5587 (2012).

8 Buurmans, I. L. C. & Weckhuysen, B. M. Heterogeneities of individual catalyst particles in space and time as monitored by spectroscopy. *Nature Chem.* **4**, 873-886 (2012).

9 Roeffaers, M. B. J. *et al.* Super-resolution reactivity mapping of nanostructured catalyst particles. *Angewandte Chemie (International ed. in English) FIELD Publication Date:2004* **48**, 9285-9289 (2009).

10 Tachikawa, T., Yonezawa, T. & Majima, T. Super-resolution mapping of reactive sites on titania-based nanoparticles with water-soluble fluorogenic probes. *ACS Nano* **7**, 263–275 (2012).

11 Zhou, X. *et al.* Quantitative super-resolution imaging uncovers reactivity patterns on single nanocatalysts. *Nat. Nanotechnol.* **7**, 237–241 (2012).

12 Zhang, Y. *et al.* Superresolution fluorescence mapping of single-nanoparticle catalysts reveals spatiotemporal variations in surface reactivity. *Proceedings of the National Academy of Sciences* **112**, 8959–8964 (2015).

13 Huang, X. & Zheng, N. One-pot, high-yield synthesis of 5-fold twinned pd nanowires and nanorods. *J. Am. Chem. Soc.* **131**, 4602–4603 (2009).

14 Bueno, C. *et al.* The excited-state interaction of resazurin and resorufin with amines in aqueous solutions. Photophysics and photochemical reactions. *Photochem Photobiol* **76**, 385-390 (2002).

15 Balcerzyk, A. & Baldacchino, G. Implementation of laser induced fluorescence in a pulse radiolysis experiment--a new way to analyze resazurin-like reduction mechanisms. *Analyst* **139**, 1707-1712 (2014).

16 Henry, A. I. *et al.* Correlated structure and optical property studies of plasmonic nanoparticles. *J. Phys. Chem. C* **115**, 9291-9305 (2011).

17 Chang, W. S. *et al.* Radiative and nonradiative properties of single plasmonic nanoparticles and their assemblies. *Acc. Chem. Res.* **45**, 1936-1945 (2012).

18 Lai, S. C. S., Dudin, P. V., Macpherson, J. V. & Unwin, P. R. Visualizing zeptomole (electro)catalysis at single nanoparticles within an ensemble. *J. Am. Chem. Soc.* **133**, 10744–10747 (2011).

19 Renault, C. *et al.* Observation of nanometer-sized electro-active defects in insulating layers by fluorescence microscopy and electrochemistry. *Anal Chem* **87**, 5730-5737 (2015).

20 Collins, S. S. E., Cittadini, M., Pecharromán, C., Martucci, A. & Mulvaney, P. Hydrogen spillover between single gold nanorods and metal oxide supports: A surface plasmon spectroscopy study. *ACS Nano* **9**, 7846-7856 (2015).

21 Xu, W. *et al.* Single-molecule electrocatalysis by single-walled carbon nanotubes. *Nano Lett.* **9**, 3968–3973 (2009).

22 Xu, W., Kong, J. S., Yeh, Y.-T. E. & Chen, P. Single-molecule nanocatalysis reveals heterogeneous reaction pathways and catalytic dynamics. *Nat. Mater.* **7**, 992-996 (2008).

23 Andoy, N. M. *et al.* Single-molecule catalysis mapping quantifies site-specific activity and uncovers radial activity gradient on single 2d nanocrystals. *J. Am. Chem. Soc.* **135**, 1845–1852 (2013).

24 Bian, Z., Tachikawa, T., Kim, W., Choi, W. & Majima, T. Superior electron transport and photocatalytic abilities of metal-nanoparticle-loaded tio2 superstructures. *J. Phys. Chem. C* **116**, 25444–25453 (2012).

25 Chernyak, L., Osinsky, A., Fuflyigin, V. & Schubert, E. F. Electron beam-induced increase of electron diffusion length in p-type gan and algan/gan superlattices. *Appl. Phys. Lett.* **77**, 875-877 (2000).

26 Gonzalez-Vazquez, J. P., Anta, J. A. & Bisquert, J. Determination of the electron diffusion length in dye-sensitized solar cells by random walk simulation: Compensation effects and voltage dependence. *J. Phys. Chem. C* **114** 8552-8558 (2010).

27 Utterback, J. K. *et al.* Observation of trapped-hole diffusion on the surfaces of cds nanorods. *Nat Chem* **8**, 1061-1066 (2016).

28 Jennings, J. R. & Peter, L. M. A reappraisal of the electron diffusion length in solid-state dye-sensitized solar cells. *J. Phys. Chem. C* **111**, 16100-16104 (2007).

29 Jana, N. R., Gearheart, L. & Murphy, C. J. Wet chemical synthesis of high aspect ratio cylindrical gold nanorods. *J. Phys. Chem. B* **105**, 4065-4067 (2001).

30 Wang, Z. L., Mohamed, M. B., Link, S. & El-Sayed, M. A. Crystallographic facets and shapes of gold nanorods of different aspect ratios. *Surf. Sci.* **440**, L809-L814 (1999).

31 Johnson, C. J. *et al.* Growth and form of gold nanorods prepared by seed-mediated, surfactant-directed synthesis. *J. Mater. Chem.* **12**, 1765-1770 (2002).

32 Carbó-Argibay, E. *et al.* The crystalline structure of gold nanorods revisited: Evidence for higher-index lateral facets. *Angewandte Chemie (International ed. in English) FIELD Publication Date:2004* **49**, 9397-9400 (2010).

33 Katz-Boon, H. *et al.* Three-dimensional morphology and crystallography of gold nanorods. *Nano Lett.* **11**, 273–278 (2011).

34 Gai, P. L. & Harmer, M. A. Surface atomic defect structures and growth of gold nanorods. *Nano Lett.* **2**, 771-774 (2002).

35 Shankar, S. S. *et al.* Biological synthesis of triangular gold nanoprisms. *Nature Mater.* **3**, 482-488 (2004).

36 Liz-Marzán, L. M., Giersig, M. & Mulvaney, P. Synthesis of nanosized gold−silica core−shell particles. *Langmuir* **12**, 4329–4335 (1996).

37 Botella, P., Corma, A. & Navarro, M. T. Single gold nanoparticles encapsulated in monodispersed regular spheres of mesostructured silica produced by pseudomorphic transformation. *Chem. Mater.* **19**, 1979–1983 (2007).

38 Han, K. S., Liu, G., Zhou, X., Medina, R. E. & Chen, P. How does a single pt nanocatalyst behave in two different reactions? A single-molecule study. *Nano Lett.* **12**, 1253-1259 (2012).

39 Miranda, K. M., Espey, M. G. & Wink, D. A. A rapid, simple spectrophotometric method for simultaneous detection of nitrate and nitrite. *Nitric Oxide* **5**, 62-71 (2001).

40 Ha, J. W. *et al.* Super-resolution mapping of photogenerated electron and hole separation in single metal-semiconductor nanocatalysts. *J Am Chem Soc* **136**, 1398–1408 (2014).

41 Decan, M. R., Impellizzeri, S., Marin, M. L. & Scaiano, J. C. Copper nanoparticle heterogeneous catalytic 'click' cycloaddition confirmed by single-molecule spectroscopy. *Nat Commun* **5**, 4612 (2014).

42 Cordes, T. & Blum, S. A. Opportunities and challenges in single-molecule and single-particle fluorescence microscopy for mechanistic studies of chemical reactions. *Nat Chem* **5**, 993-999 (2013).

43 Goldsmith, R. H. *et al.* Redox cycling and kinetic analysis of single molecules of solution-phase nitrite reductase. *Proc. Nat. Acad. Sci. USA* **108**, 17269-17274 (2011).

5. SUPPORTING INFORMATION OF CHAPTER FOUR

5.1. Synthesis and characterization of nanocatalysts

5.1.1. Pd nanorods and $mSiO_2$ coating.

Pd nanorods were prepared using a hydrothermal synthesis following Huang et al.[1] All chemicals were purchased from Sigma-Aldrich unless specified otherwise. 17.7 mg $PdCl_2$, 300 mg NaI and 800 mg polyvinylpyrrolidone (PVP, MW = 55000) were dissolved in 18 mL nanopure water. Under stirring, the mixture was heated to 60 °C for 1 h in order to get a homogeneous solution and then transferred into a 100 mL Teflon-lined autoclave. The reactor was kept at 200 °C for 16 h to grow Pd nanorods. The resulting solution was cooled down to room temperature and mixed with isopropanol. The mixture was centrifuged at 10000 g for 10 min and then supernatant was removed. The washing and precipitation process was repeated once more. After purification, the precipitated Pd nanorods were collected and re-dispersed in 10 mL water for later silica shell overgrowth. The length and diameter of as-made Pd nanorods are 559 ± 223 nm and 37.4 ± 4.8 nm, respectively (Figure 5.1a-d). According to Huang et al[1], these Pd nanorods are likely 5-fold twinned structure with five {100} side surfaces along the ⟨110⟩ direction.

The as-made Pd nanorods were coated by a mesoporous silica shell using a procedure slightly modified from that reported in our previous work[2]. There were three steps involved: shell growth, shell etching, and sample activation:

(1) Shell growth: 100 μL 0.11 M 3-mercaptopropionic acid (MPA) in ethanol (instead of MPTMS in reference[2]) was added to 10 mL Pd nanorod aqueous solution under stirring to replace the PVP left on Pd surface. After 24 h of this ligand exchange reaction,

100 μL 17 mM sodium silicate (Fisher Scientific) solution was added to grow an initial thin layer of silica on Pd nanorods. The resulting solution (pH adjusted to 9 using 2 M HCl solution) was stirred for 48 h and then centrifuged at 3,000 g to remove the supernatant. The precipitate was re-dispersed in a 10 mL 4:1 v/v ethanol/water mixture for the subsequent shell growth. 120 μL 10% (v/v) tetraethyl orthosilicate (TEOS) in ethanol and 100 μL 0.1 M NaOH solution were added into the mixture under vigorous stirring to grow a thicker silica shell. After 24 h growth, the solution was centrifuged at 3,000 g, and the silica-coated Pd nanorods were collected. The silica shell thickness was ~150 nm. The silica-coated Pd nanorods were re-dispersed in 11:1 v/v water/ethanol mixture for etching the shell mesoporous.

(2) Shell etching: The above silica-coated Pd nanorod solution was mixed with 60 μL 0.1 M cetyltrimethylammonium bromide (CTAB) and 60 μL 0.1 M NaOH solutions. The mixture was stirred for 30 min and then heated at 90 °C for 40 min to form mesoporous silica (i.e., $mSiO_2$) coated Pd nanorods. The resulting solution was cooled to room temperature and centrifuged at 3,000 g to collect these nanorods as precipitate. The final sample was washed by water and ethanol multiple times and dried in air. According to literature[3], the mesoporous silica shell has ordered wormhole-like pores. The average pore size is ~35 Å; and its specific surface area is ~1000 $m^2 g^{-1}$.

(3) Sample activation: The dried sample was calcinated in air at 450 °C for 1 h to remove organic compounds introduced in the synthesis and make the metal surface accessible to the reactant for catalytic reactions. After calcination (which also led to formation of palladium oxide), the $mSiO_2$-coated Pd nanorods were re-dispersed in 1 mL water. An adequate amount (~10 μL) of 0.1 M $NaBH_4$ solution was added drop-wise into

the solution until the solution color was changed from brown to gray and kept for 5 min. (Note: too long an incubation in this solution would lead to a complete etch away of the shell.) The color change indicated that palladium oxide formed during the calcination process was reduced to Pd.[4] The sample after $NaBH_4$ treatment was washed by water multiple times to remove unreacted $NaBH_4$. The final $mSiO_2$ shell thickness is ~125 nm, and the Pd nanorod cores maintain their rod morphology (Figure 5.1e).

5.1.2. Au nanorods and nanoplates and mSiO2 coating.

Au nanorods were synthesized as we reported[2,5] (Figure 5.1f), and are multiply twinned or single crystals[6-11]. The triangular- and hexagonal-shaped Au nanoplates were synthesized also as we reported[12,13] (Figure 5.1h). The Au nanorods and nanoplates were then coated with a mesoporous silica shell (Figure 5.1g, i) as we reported[2,12].

5.1.3. Necessity and advantage of the $mSiO_2$ coating.

The $mSiO_2$ shell on Pd and Au nanocatalysts allows for subsequent calcination (or UV/ozone) treatment to remove the organic ligands on the metal surfaces for catalysis, while still maintaining the morphologies of nanorod and nanoplate cores and preventing their aggregation. This shell contains complex wormhole-like pores, which, according to literature, has an average pore size of ~3.5 nm and specific surface area of ~1000 $m^2 g^{-1}$.[3] The reactants can still access the metal surface for catalysis through the mesopores, and the mass transport of the reactants to the metal surface does not limit the catalytic kinetics as we demonstrated previously for $mSiO_2$-coated Au nanorods and nanoplates[2,12], primarily because the catalytic conversion kinetics is slow. The $mSiO_2$ shell also helps trapping the fluorescent product molecules temporarily (i.e., via molecular adsorption onto silica-based sites within the pores), facilitating their detection, as well as circumventing the potential

fluorescence quenching associated with direct detection on metal surfaces.

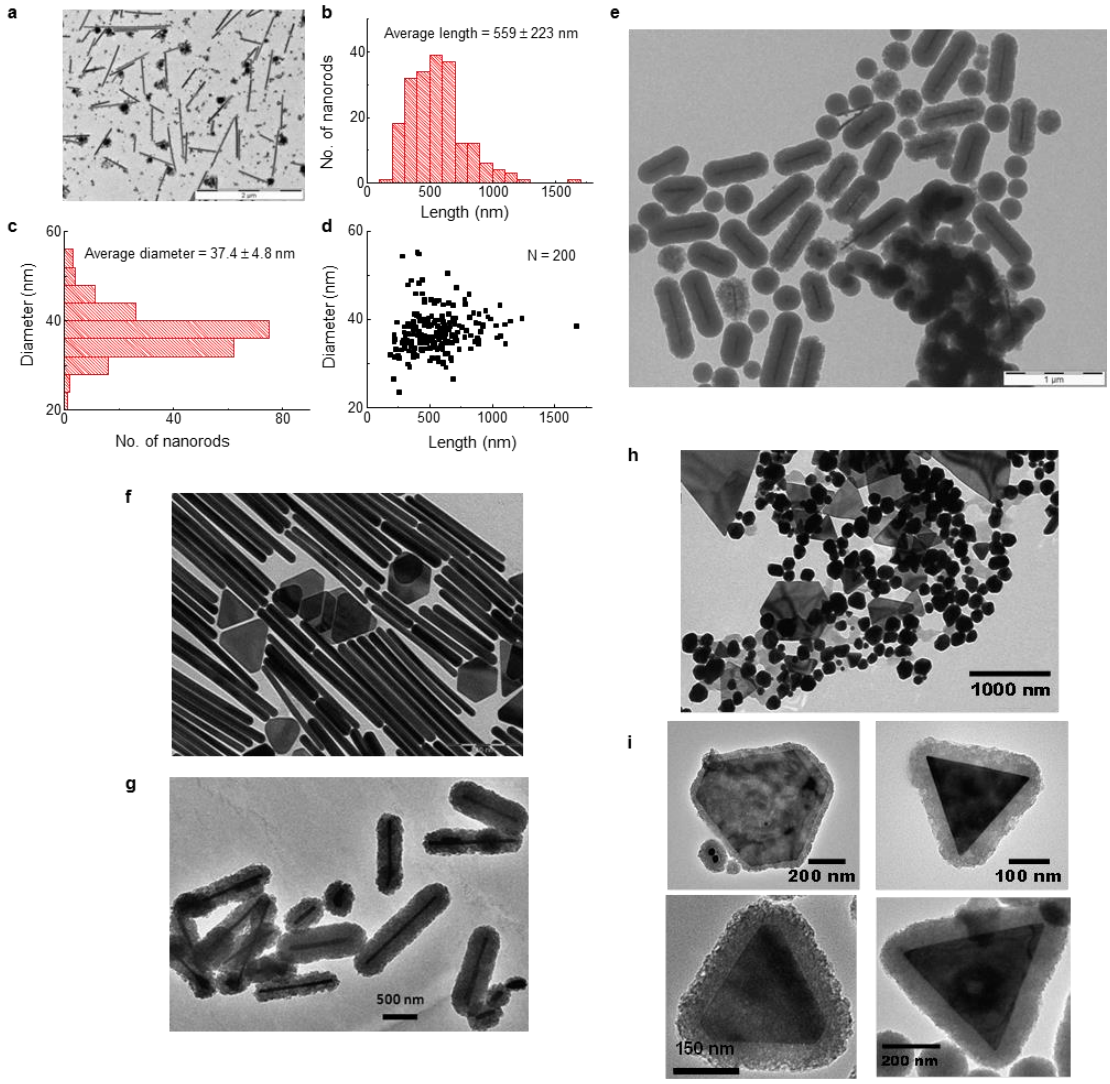

Figure 5.1. Characterization of Pd nanorods, Au nanorods, and Au nanoplates before and after $mSiO_2$ coating. (**a-d**) TEM image (a) and the structural parameters of as-synthesized Pd nanorods. (**e**) TEM of the $mSiO_2$-coated Pd nanorods after $NaBH_4$ treatment. $mSiO_2$ shell thickness: 125.5 ± 6.5 nm. (**f-g**) TEM image of the as-synthesized (f) and $mSiO_2$-coated Au nanorods after heat treatment at ~500 °C (g). The nanorod sample also contains other shaped and many pseudospherical particles. The Au nanorods are about 100 to 700 nm in length and 21.4 ± 3.2 nm in diameter; the $mSiO_2$ shell is ~85 nm thick[2]. (**h-i**) TEM image of as-synthesized (h) and $mSiO_2$-coated Au

nanoplates after UV/ozone treatment (i). The nanoplate sample is a mixture of Au nanoplates and pseudospherical particles. The nanoplates are triangular or hexagonal, with edge length of about 10 to 1000 nm and thickness of 13.7 ± 0.7 nm; the $mSiO_2$ shell is ~43 nm thick[12]. UV/ozone treatment was used instead of heat because heating to remove organic components changed the morphology of the Au nanoplate core.

5.2. Fluorogenic catalytic reactions, and ensemble assay shows that Pd nanorods can catalyze resazurin disproportionation to generate resorufin

The three fluorogenic catalytic reactions are shown in Figure 4.1b in the main text. For most experiments, the reactant concentrations were such that the kinetics was saturated and pseudo-zeroth order to the reactant concentrations, and the kinetics was rate-limited by catalytic conversion from the reactants to the products rather than by reactant adsorption or product desorption, as we experimentally determined for Au nanocatalysts[2,12,14].

For Pd-nanorod-catalyzed photo-induced disproportionation of resazurin (Rz), the typical reaction conditions were: [Rz] = 0.05 μM in 10 mM pH 9.1 borate buffer. The reaction stoichiometry of resazurin to resorufin is ~3:1, determined from fluorescence measurement of the reaction solution (Figure 5.2A). Previous studies have shown that under intense 532 nm excitation, photo-excited resazurin can disproportionate into a 1-electron reduced species and another 1-electron oxidized species[15], and the 1-electron reduced species can further disproportionate into resorufin, which is 2-electron reduced from resazurin, and resazurin[16]. We determined that the overall stoichiometry of this reaction without catalysis is also ~3:1 for resazurin to resorufin.

Regarding Au-based nanocatalysts, we have previously shown they can catalyze the oxidative deacetylation of AR by H_2O_2 and the reductive deoxygenation of Rz by NH_2OH. In both systems, the Au particle is the active catalyst component, while the $mSiO_2$ shell is not. For deacetylation, other reaction products include acetate and H_2O besides resorufin[17]. For deoxygenation, besides resorufin, another reaction product is nitrite (NO_2^-), which was detected by the colorimetric Griess reaction[18] and is consistent with the aqueous oxidative chemistry of NH_2OH[19]. The quantification of nitrite was done also by Griess reaction via calibration by standard solutions of potassium nitrite, giving a stoichiometry of resazurin to nitrite of ~2:1.

For AR deacetylation, the typical reaction conditions were (unless specified otherwise): [AR] = 0.2 μM, H_2O_2 kept at large excess at 60 mM, in 100 mM pH 7.2 phosphate buffer. At [AR] > ~0.2 μM, the reaction kinetics approaches pseudo-zeroth order to [AR] (and $[H_2O_2]$)[2]. For Rz deoxygenation, the reaction conditions were (unless specified otherwise): [Rz] = 0.2 μM, NH_2OH kept at large excess at 10 mM, in 100 mM pH 7.2 phosphate buffer. At [Rz] > ~0.15 μM, the reaction kinetics approaches pseudo-zeroth order to [Rz][12,14].

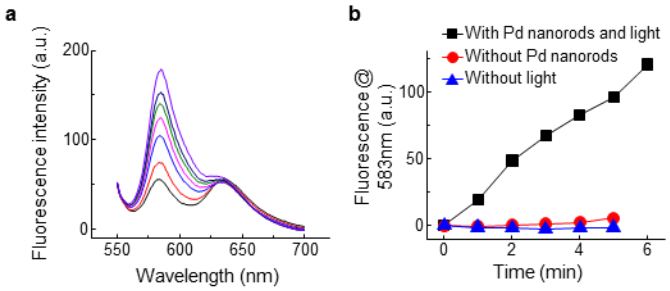

Figure 5.2 Ensemble activity assay shows that Pd nanorods can catalyze the photo-driven disproportionation of resazurin to generate resorufin, while the un-catalyzed or non-illuminated reaction is negligible relatively. (**a**) Time-dependent fluorescence spectra of a reaction solution

containing 86.4 μM resazurin, Pd nanorods and 0.2 M phosphate buffer under 5 mW 532 nm laser illumination (beam diameter = 0.7 mm). The ensemble measurements were done at pH = 7.2 to make the reaction faster and more easily measured, instead of pH 9.1 for single-molecule imaging measurements. The increase of fluorescence intensity peaked at 583 nm is due to the formation of resorufin. (**b**) Time profiles of fluorescence intensity at 583 nm of the reaction solution in a (black) and in control experiments similar to that in a except that no Pd nanorods were added (red) or no 532 nm laser illumination (blue). The reaction rate is 0.35 ± 0.10 μM/min for Pd-catalyzed disproportionation (black), 0.019 ± 0.024 μM/min for the uncatalyzed disproportionation (red) and zero (i.e., −0.004 ± 0.016 μM/min) without 532 nm illumination (blue). Methods: Since the as-synthesized Pd nanorods are capped by PVP, they cannot be used directly as catalysts. We thus used the surfactant-free Pd nanorods to test their ensemble catalytic activity. The heat-treated $mSiO_2$-coated Pd nanorods were dispersed in 0.1 M $NaBH_4$ and the mixture was kept for 3 h to reduce the palladium oxide formed in calcination as well as to dissolve the $mSiO_2$ shell (due to the strongly basic $NaBH_4$ solution), which exposed more Pd surfaces for ensemble activity measurements. The Pd nanorods were collected by centrifugation. The reaction solution was sealed in a borosilicate glass tube (Sutter Instrument) for the ensemble activity measurement.

5.3. Experimental setup for single-molecule fluorescence imaging, solution flow and voltage manipulations, as well as acetate and nitrite effects

5.3.1. Experimental setup for single-molecule fluorescence imaging.

Catalysis on individual nanocatalysts was imaged using single-molecule fluorescence microscopy[2,20-31], based on a total internal reflection fluorescence microscope, at room temperature under ambient conditions (Figure 5.3), as described[2,12]. A continuous-wave

circularly polarized 532 nm laser of 2-30 mW induced the fluorescence of the product resorufin generated on immobilized nanocatalysts within an area of ~50 × 100 μm^2 on a slide in a microfluidic reactor (dimension: ~150 μm high, ~5 to 10 mm wide, and ~3 cm long, formed by double-sided tape sandwiched between a quartz slide and a coverslip). The aqueous reactant solution was supplied into the reactor continuously at 5 to 100 μL min^{-1}, which provided a steady-state reaction condition. The fluorescence of the product resorufin was imaged at the single-molecule level and recorded by an EMCCD camera operating at 25 or 30 ms frame rate.

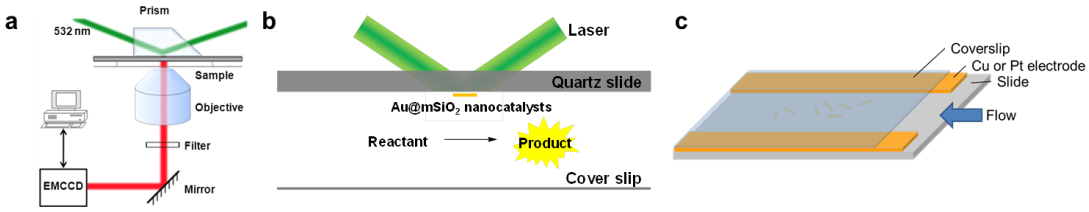

Figure 5.3. Single-molecule fluorescence imaging of catalysis. (**a**) Experimental scheme using a homebuilt prism-based total internal reflection (TIR) fluorescence microscope (Olympus IX71) with 532 nm laser excitation and a liquid microfluidic reactor cell made between a quartz slide and a cover slip. (**b**) Schematic of the microfluidic reactor cell (approximately 150 μm (height), 3 cm (length), and 5-10 mm (width)) showing catalyst particles immobilized on the slide, the fluorogenic catalytic reaction, and the TIR laser excitation. (**c**) Schematic of the microfluidic reactor construction for voltage manipulation experiments. The two metal electrodes (copper foil or platinum wire) are sandwiched between the quartz slide and the coverslip, held together by double-sided tapes. The distance between the two electrodes is 5-8 mm.

5.3.2. Solution flow and voltage manipulations.

The reactant solution flow was varied from ~5 to 100 μL min^{-1} using a syringe pump, corresponding to a linear flow rate of ~100 to 2000 μm s^{-1} (depending on the cross section

of the particular reactor). A two-electrode configuration potentiostat was used to apply a voltage ranging from –1.2 to 1.2 V across the microfluidic reactor (see Section 5.13 for more details).

The interparticle and intraparticle *i*-to-*j* vector orientation angles are defined in Figure 4.4a relative to the solution flow (θ) and the EF direction (φ). In analyzing the dependence of the catalytic communication distance on the orientation angle (e.g., Figure 3.5 b and e), the data were fitted with the following cosine function:

$$y = a\cos x + b \qquad \text{Eq. 5.1}$$

where x is either θ or φ; a is the amplitude of the cosine function (e.g., $\Delta x_{0,\text{flow}}^{\text{inter}}$ and $\Delta x_{0,\text{EF}}^{\text{inter}}$ in Figure 4.5c and f), which could be positive or negative; and b is an offset.

5.3.3. Acetate and nitrite effects.

Various concentrations of acetate and nitrite were titrated into the reaction solution for the Au-nanocatalyst catalyzed AR deacetylation and Rz deoxygenation, respectively. See data in Section 5.14. The promotion effect on the catalytic activity by acetate or nitrite (e.g., Figure 4.5g) was fitted with the following saturation equation:

$$y = \frac{ax}{x + K_{1/2}} + b \qquad \text{Eq. 5.2}$$

where x is either [CH_3COO^-] or [NO_2^-], and $K_{1/2}$ is the half saturation concentration of added acetate or nitrite. The corresponding quenching effect of acetate or nitrite on the interparticle catalytic communication distance (e.g., Figure 4.5h) was fitted with a negative saturation equation:

$$y = -\frac{ax}{x + K_{1/2}} + b \qquad \text{Eq. 5.3}$$

5.4. Data processing for single-molecule fluorescence imaging, localization precision, and spatial resolution

The fluorescence signals of the products during catalytic reactions were imaged at the single-molecule level and recorded in a movie. We analyzed the movie images to localize the positions of individual product molecules, as similarly done in STORM[30,32] and PALM[29,31,33], two closely related super-resolution imaging techniques based on wide-field single-molecule fluorescence detection. The analysis was done using a home-written MatLab program[2]. Exemplary data of individual product position maps are presented in Figure 5.4 f-j. Our analysis procedures were described in detail previously[2], and summarized schematically in Figure 5.4 and below.

We typically localize the positions of individual fluorescent product resorufin on individual nanocatalysts to about 35-45 nm precision, in correlation with the nanocatalyst's SEM image. This 35-45 nm uncertainty includes contributions from the signal/noise ratio of single-molecule fluorescence imaging, and is comparable to the potential influence from the fluorescence scattering by the plasmonic Au nanorods/nanoplates that could potentially shift the fluorescence central position by tens of nanometers[34-36]. Using different-diameter pseudospherical $mSiO_2$-coated Au nanoparticles, we previously showed that the typical spatial resolution of our method is 30-40 nm, reflected by the fact that this super-resolution catalysis imaging can accurately measure the diameter of pseudospherical Au nanocatalysts down to 30-40 nm[37]. *Note that this spatial resolution is <u>much smaller</u> than the segment size*

in dissecting Pd/Au nanorods and nanoplates in our analysis of catalytic communications as well as <u>much smaller</u> than the intraparticle catalytic communication distance x_0^{intra}.

First, we identified the individual nanocatalysts in both the SEM (Figure 5.4d-1) and the optical/fluorescence images (Figure 5.4d-3 and d-6); these nanocatalysts scatter laser light strongly, and are also emissive (for Au nanocatalysts) (Figure 5.4d-3), and thus readily identifiable in the optical microscope. We then extracted the fluorescence intensity trajectory of each nanocatalyst under catalysis from the recorded fluorescence movie by integrating the EMCCD counts over a 7×7 pixel area (each pixel ~267 nm) around the nanorod/nanoplate (Figure 5.4a-1 and b). The trajectory showed bursts of fluorescence intensity on top of the background emission signal of the nanorod/nanoplate itself; the bursts are due to catalytic formations of the product molecule resorufin. We then used intensity thresholds to select the fluorescence burst events from product molecule formation (Figure 5.4a-2). An area of 13 × 13 pixels (~3.5 ×3.5 μm^2) around the product molecule was cropped out, and all image frames contributing to the same single burst were added together to enhance the signal to noise ratio (Figure 5.4a-3). From this image, the emission/background signal of the nanocatalyst itself was subtracted; here the nanocatalyst emission signal was taken from the image frames right before the appearance of the burst signal in the movie. The resulting image only contained the fluorescence signal of the catalytic product molecule resorufin. Then the image of the molecule, which behaves as a point spread function (PSF), was fitted by a two-dimensional Gaussian function to obtain the center position (x_0, y_0) of the PSF, which reflects the position of the product molecule (Figure 5.4a-4 and c). Provided that a large number of fluorescence photons are detected, the center position (x_0, y_0) can be localized down to a few nm accuracy[38,39], but often around 35-45 nm in this study due to

short residence time of the product on the nanocatalyst. To reduce the contribution of noises to the selected burst events, we further filtered the selected burst events by their localization accuracies and the widths of the fitted PSF (Figure 5.4a-5), as we described previously[2]. The center positions of all molecules were further corrected for microscope stage drifting, using the intrinsic emission signal of the Au nanoparticles as position markers (Figure 5.4a-6). The positions of catalytic product molecules on a single nanocatalyst can be overlaid together in a scatter plot (Figure 5.4a-7 and d-4) and correlated with the SEM image of the nanocatalyst (Figure 5.4a-8 and d-1), whose structural contour was determined from the SEM image. The correlation with the SEM image could be directly mapped using position markers, as we described[2,12], and for the nanorods, could also be performed by fitting the SEM structural contour to the 2-D histogram of the product positions as we demonstrated (Figure 5.4d-5)[2]. Once the structural contour of a nanocatalyst was mapped on top of the positions of catalytic products, the nanocatalyst could be dissected into segments. The product molecules were sorted to their corresponding segments, on the basis of their positions.

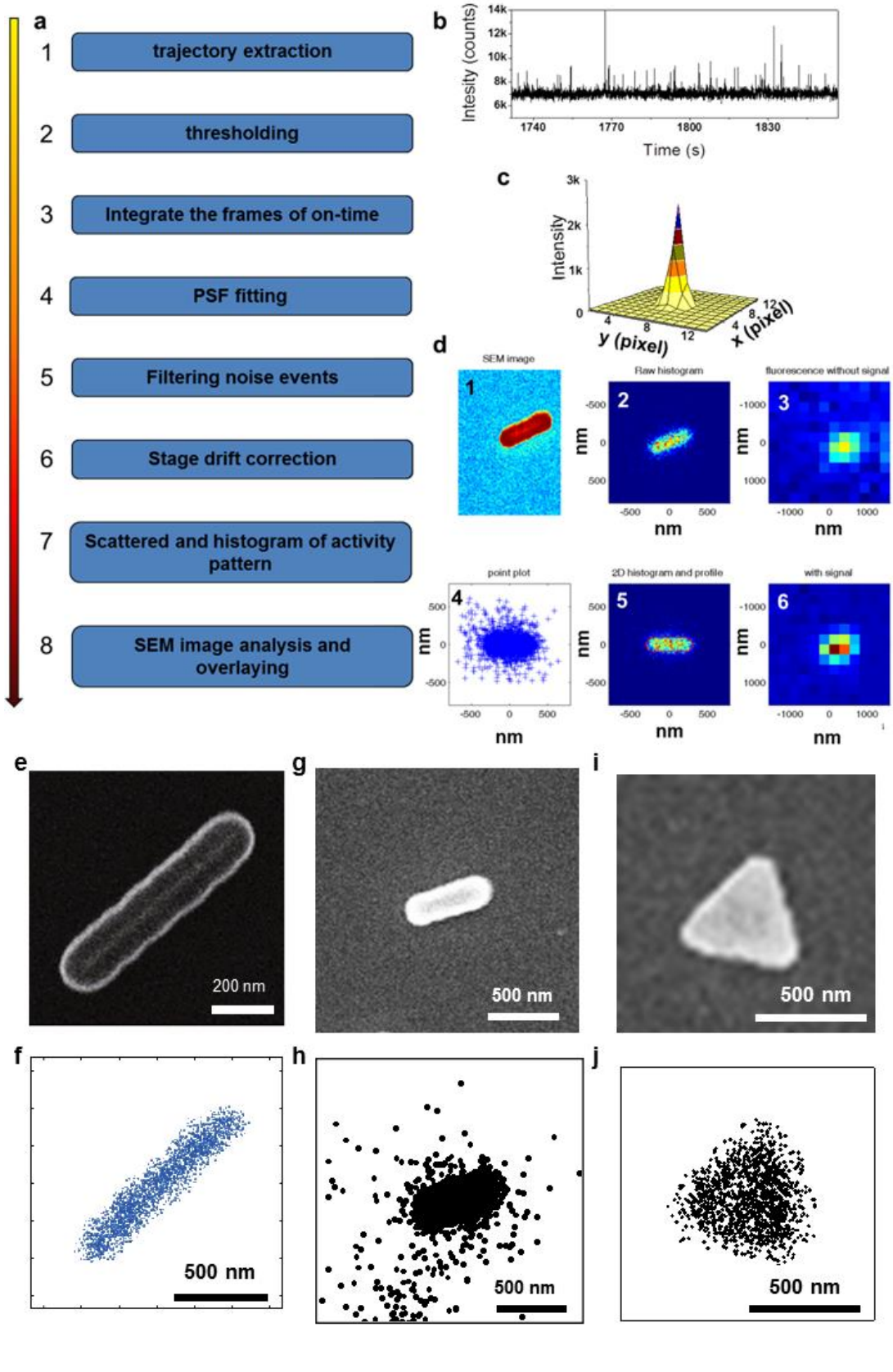
a
1
trajectory extraction
2
thresholding
3
Integrate the frames of on-time
4
PSF fitting
5
Filtering noise events
6
Stage drift correction
7
Scattered and histogram of activity pattern
8
SEM image analysis and overlaying
b
Intesity (counts)
Time (s)
c
Intensity
y (pixel)
x (pixel)
d
SEM image
Raw histogram
fluorescence without signal
point plot
2D histogram and profile
with signal
nm
e
200 nm
g
500 nm
i
500 nm
f
500 nm
h
500 nm
j
500 nm

Figure 5.4. Scheme of single-molecule super-resolution imaging analysis of catalytic reactions (a-d) and exemplary data on single Pd and Au nanocatalysts (e-j). (**a**) Major analysis steps for super-resolution imaging of the catalytic products on individual nanocatalysts. (**b**) A fluorescence intensity trajectory from a $mSiO_2$-coated Au nanorod undergoing catalysis; the fluorescence intensity bursts are due to the formation events of the catalytic product resorufin. (**c**) 2-D Gaussian fitting of the PSF of a fluorescent product on a Au nanorod. (**d**) Exemplary data: (1) SEM image of a $mSiO_2$-coated Au nanorod; (2) 2-D histogram of product positions as in (4) on the nanorod shown in (1). (3) The emission signal/image of the nanorod in (1). (4) Scatter plot of the positions of the many product molecules detected on the nanorod in (1). (5) 2-D histogram of (4) with the SEM structural contour from (1) overlaid on top; note that the orientations of both (4) and (5) are rotated relative to those of (1) and (2) so that the long axis of the nanorod lies horizontally. (6) The fluorescence signal/image of a resorufin product on top of the nanorod. (**e**) SEM of the Pd nanorod, same as Figure 4.1c in the main text. (**f**) Positions of many product P molecules from the disproportionation of resazurin on the nanorod in **e**, from which the 2-D histogram in Figure 4.1d was obtained. Each dot is one P molecule. (**g**) SEM of a $mSiO_2$-coated Au nanorod. (**h**) Positions of many product P molecules from the deacetylation reaction of amplex red detected on the nanorod in **g**. (**i)** SEM of a triangular $mSiO_2$-coated Au nanoplate presented in Figure 5.17a. Note that the orientation of Figure 5.17a has been rotated so that one edge of the nanoplate aligns horizontally. **(j)** Positions of many P molecules from the deoxygenation reaction of resazurin detected on the nanoplate in **i**.

5.5. The product resorufin stays on the nanorod for ~38 ms on average, orders of magnitude shorter than its photoblinking/bleaching on-time, and it stays essentially stationary within our localization precision before desorbing into solution.

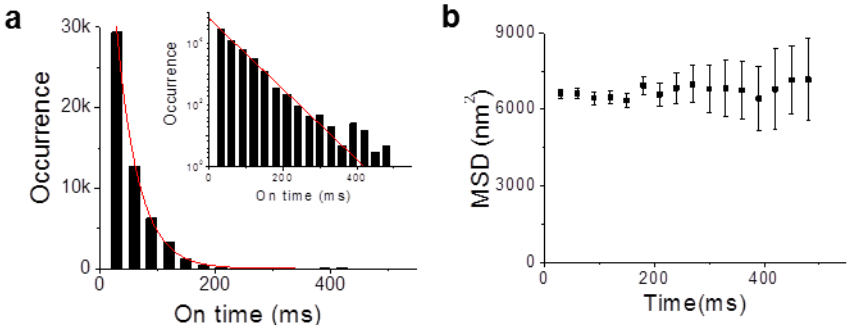

Figure 5.5. Diffusion analysis of product molecules. (**a**) Distribution of the fluorescence on-time (i.e., the time each product molecule stays adsorbed on the nanocatalysts) for Au nanorod catalyzed AR deacetylation reaction. It follows a single exponential distribution (red line) with **a time constant 37.9±0.6 ms, which is <2 imaging frames and is ~2 orders of magnitude shorter than the photobleaching/blinking on-times of the product resorufin that occur at seconds or longer timescales**[14,40]. Inset: same plot in log-linear scale, showing that some *individual* on-times can be a few hundred ms long, which allows us to track the position of the product molecule frame-by-frame while it stayed adsorbed on the nanocatalyst. **(b)** Mean-square-displacement (MSD, $\langle r^2 \rangle = \langle (x_i - x_j)^2 + (y_i - y_j)^2 \rangle$) vs time of the product resorufin during the fluorescence on-times by tracking the position of the individual resorufin product during each fluorescence on-time. The MSD does *not* increase with increasing time, **indicating that the resorufin stays essentially stationary and does not diffuse much laterally within the $mSiO_2$ shell before it desorbs into the surrounding solution**. This stationary behavior likely comes from resorufin adsorption onto sites in the mesopores of the $mSiO_2$ shell, at which desorption into solution is faster than diffusing along the nanorod's long

axis within the $mSiO_2$ shell laterally. The finite positive value of MSD (i.e., $\langle r^2 \rangle$~6500 nm^2) comes from the fact that the *x* and *y* positions of each product molecule have a localization uncertainty of ~40 nm. This localization uncertainty can be described by a Gaussian distribution of *x* and *y*, $P(x)$ and $P(y)$, centered at the true positions x_0 and y_0 with a standard deviation σ of ~40 nm: $P(x) = \frac{1}{\sigma\sqrt{2\pi}} e^{-\frac{(x-x_0)^2}{2\sigma^2}}$ and $P(y) = \frac{1}{\sigma\sqrt{2\pi}} e^{-\frac{(y-y_0)^2}{2\sigma^2}}$. The expected value of r^2 is then $E(r^2) = E\left((x_i - x_j)^2 + (y_i - y_j)^2\right) = \iint (x_i - x_j)^2 P(x_i)P(x_j)\mathrm{d}x_i\mathrm{d}x_j + \iint (y_i - y_j)^2 P(y_i)P(y_j)\mathrm{d}y_i\mathrm{d}y_j = 4\sigma^2$. As σ ~ 40 nm, the expected value of r^2 is ~6400 nm, consistent with the experimental observation here.

5.6. Analysis procedures of the *intra-* and *inter-particle* catalytic communications between temporally subsequent reactions that occur at different locations.

5.6.1. Intraparticle catalytic communication within Pd or Au nanorods

Once we obtained the catalytic event sequence of each nanorod segment, we analyzed the correlation of the microscopic reaction time τ between temporally subsequent reactions that occur at different segments. For any segment *i* on a single nanorod that has many catalytic events (*i* = 1 to *n*; *n* is the total number of segments of a nanorod), the microscopic reaction time τ_i of each event is paired with τ_j of the *immediate subsequent* catalytic event that occurs on a different segment *j* (*j* = 1 to *n*; $j \neq i$) on the same nanorod (Figure 5.6a, b). In this way, we obtained many $\tau_i \rightarrow \tau_j$ pairs between the event sequence of segment *i* and that of segment *j*. A Pearson's cross-correlation coefficient ρ_{τ_i,τ_j} was then

calculated for these *many* $\tau_i \rightarrow \tau_j$ pairs:

$$\rho_{\tau_i,\tau_j} = \frac{\langle \tau_i \tau_j \rangle - \langle \tau_i \rangle \langle \tau_j \rangle}{\sqrt{\left(\langle \tau_i^2 \rangle - \langle \tau_i \rangle^2\right)\left(\langle \tau_j^2 \rangle - \langle \tau_j \rangle^2\right)}} \qquad \text{Eq. 5.4}$$

Note that this event pairing is directional and asymmetric between the segment *i* and *j*: it uses all τ_i's in the event sequence from segment *i*, except for its last event, which may or may not have a subsequent event on sequence *j*; but not all τ_j's of the event sequence *j* are necessarily used. Our analysis computed the cross-correlation coefficient for both directions when both *i* and *j* are stepped from 1 to *n*. ρ_{τ_i,τ_j} is a quantitative measure of how the catalytic kinetics, reflected by τ, of any reaction on one segment is correlated with the temporally subsequent one at another segment on the same nanorod. Each ρ_{τ_i,τ_j} is also a statistical property averaged over the many pairs of temporally subsequent catalytic events, in which the pairs all have the distance separation Δx_{ij} between the two segments *i* and *j*, defined as the center-to-center distance of the two segments.

For each $\tau_i \rightarrow \tau_j$ pair, the event associated with τ_j occurred at a certain time after that associated with τ_i, i.e., there is a time delay Δt_{ij} between these two temporally subsequent events that occur at two different segments. By averaging all Δt_{ij}, we obtained $\overline{\Delta t_{ij}}$, the average time separation between any two temporally subsequent events that occurred on the two segments *i* and *j*. Each ρ_{τ_i,τ_j} is thus also associated with an average time separation, $\overline{\Delta t_{ij}}$, besides a distance separation, Δx_{ij}. **Overall, $\boldsymbol{\rho_{\tau_i,\tau_j}}$ is a function of $\boldsymbol{\Delta x_{ij}}$ and $\boldsymbol{\overline{\Delta t_{ij}}}$, i.e., $\boldsymbol{\rho_{\tau_i,\tau_j}\left(\Delta x_{ij}, \overline{\Delta t_{ij}}\right)}$.** The value of ρ_{τ_i,τ_j} can be between −1 and 1. If τ_i and τ_j are completely correlated, $\rho_{\tau_i,\tau_j} = 1$; if completely uncorrelated, $\rho_{\tau_i,\tau_j} = 0$; if completely anticorrelated, ρ_{τ_i,τ_j}

= –1.

The obtained ρ_{τ_i,τ_j} between many segments from many nanorods are pooled together to increase statistics, binned along the dimension of Δx_{ij} or $\overline{\Delta t_{ij}}$, and then averaged within each bin, so as to obtain the dependence of ρ_{τ_i,τ_j} on Δx_{ij} or $\overline{\Delta t_{ij}}$, for example as presented in Figure 4.2a-b in the main text.

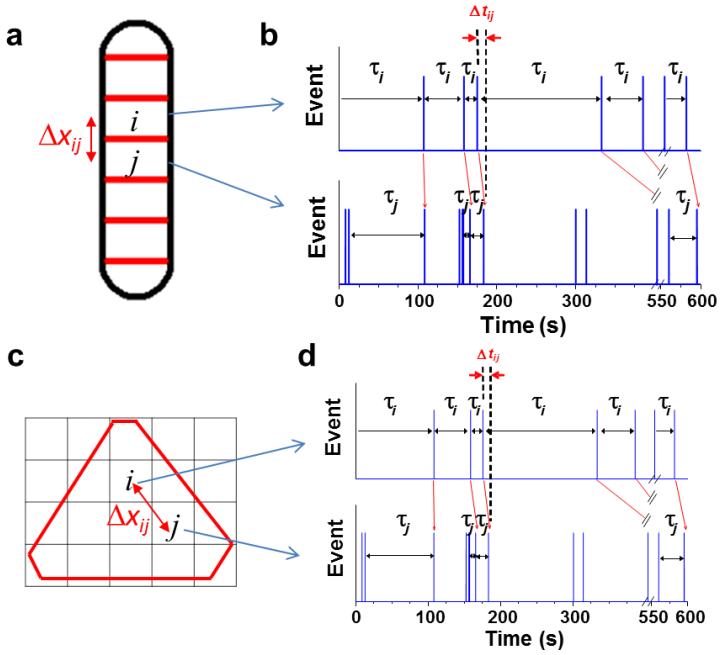

Figure 5.6. Spatiotemporally dependent cross-correlation analysis of the microscopic reaction time τ between temporally subsequent reactions that occur on two different segments on a single nanorod (a-b) or nanoplate (c-d). (**a**) Schematic of dissecting a nanorod into segments. (**b**) Schematic of two catalytic event sequences, each from a single segment. In each sequence, the individual product formation events (vertical lines) were plotted against the times when they were detected. The microscopic reaction time τ for each event is the time separation from the previous one in the same sequence. Pairs of reactions that are temporally subsequent but occur at different segments are linked by red arrows. The time separation (Δt_{ij}) was shown for one pair of catalytic events, each occurring

at one of the two segments. (**c-d**) Same schematics as a-b, but for a nanoplate, which is dissected into square segments.

5.6.2. Intraparticle catalytic communication within Au nanoplates

For the pseudo-2-D nanocrystal Au nanoplates, we dissected each nanoplate into square segments of 100 - 200 nm in each dimension (Figure 5.6c). Depending on the nanoplate, the size of the square segments was varied so that there were appreciable amount catalytic events in each segment. Most segments have more than 40 events. (The segments near the edges and corners of a nanoplate are not squares, and sometime they are so small that there are less than 40 events in it; these edge/corner segments were thus excluded in the analysis.) From each segment, we obtained its time sequence of catalytic events (Figure 5.6d). We then calculated ρ_{τ_i,τ_j} between any two segments of every Au nanoplate, and pooled all ρ_{τ_i,τ_j} from many nanoplates together.

5.6.3. Interparticle catalytic communication between temporally subsequent reactions that occur on different particles

For interparticle analysis, Pearson's cross-correlation coefficient ρ_{τ_i,τ_j} was calculated between temporally subsequent reactions that occur on *different* nanorods or nanoplates. Two effectively same methods were used in calculating the interparticle ρ_{τ_i,τ_j}. In one method, the ρ_{τ_i,τ_j} was calculated between the real-time catalytic event sequences of two segments, each belonging to a different nanorod or nanoplate (i.e., the segment-to-segment method). In the alternative method, the real-time sequences of catalytic events were generated for the individual nanocatalysts as a whole, and then calculate ρ_{τ_i,τ_j} between any two nanorods or nanoplates (i.e., the particle-to-particle method). In both methods, each

ρ_{τ_i,τ_j} is also associated with an interparticle distance separation (Δx_{ij}) and an average time separation $\overline{\Delta t_{ij}}$ between any two temporally subsequent events that occur on two different segments/particles. Figure 5.7 shows the results for Au nanorods catalyzing the deacetylation reaction. In both methods, the ρ_{τ_i,τ_j} vs. Δx_{ij} or $\overline{\Delta t_{ij}}$ dependences are indistinguishable within experimental error. As the particle-to-particle method allows for analyzing the data from pseudospherical particles that were also present in the sample of Au nanorods/nanoplates and that could not be segmented due to their smaller size (Figure 5.1f-i), the particle-to-particle method allows for more statistics. We thus used the particle-to-article method for all later analysis of interparticle catalytic communications.

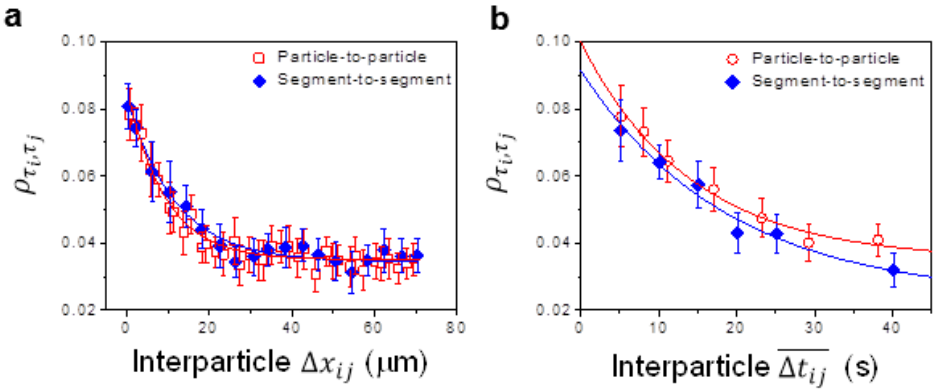

Figure 5.7. Segment-to-segment and particle-to-particle analysis of interparticle catalytic communication between Au nanorods (and pseudospherical particles) in catalyzing the deacetylation reaction. (**a, b**) Cross-correlation coefficient ρ_{τ_i,τ_j} for interparticle catalytic communication vs. interparticle Δx_{ij} or $\overline{\Delta t_{ij}}$. Solid lines are single exponential fits with a y-offset, which is the limiting value at long distance and time separations and represents the spurious contribution. For the segment-to-segment analysis method, x_0^{inter} = 10.2 ± 2.6 μm and t_0^{inter} = 16.2 ± 3.6 s; for the particle-to-particle analysis method, x_0^{inter} = 11.7 ± 2.0 μm and t_0^{inter} = 18.9 ± 2.8 s; both methods yield

essentially the same results.

5.6.4. Spurious contributions to cross-correlation coefficients, reflected by the interparticle ρ_{τ_i,τ_j} at long distance and time separations, are used as a residual offset for the intraparticle ρ_{τ_i,τ_j}

For interparticle cross-correlation coefficient ρ_{τ_i,τ_j}, it decays exponentially with increasing interparticle Δx_{ij} or $\overline{\Delta t_{IJ}}$, but it does not decay to zero, and instead to a limiting residual value at long distance and time separations (e.g., Figure 5.7). This residual cross-correlation varies slightly (0.034 ± 0.009) depending on the particular catalytic reaction and the different batches of samples. This residual cross-correlation is also present when the catalytic events are randomized spatially, temporally, or both (Figure 5.9c-d); and it is also present in the simulated random catalytic events (Figure 5.11h-i). Therefore, this residual cross-correlation represents spurious contributions to the calculated ρ_{τ_i,τ_j}, and it was used as a fixed residual offset in fitting exponential functions to all intraparticle ρ_{τ_i,τ_j} vs. Δx_{ij} or $\overline{\Delta t_{IJ}}$ results, which, due to the particle size limit, does not have values at long intraparticle distance separations.

5.7. Both intra- and inter-particle catalytic communication behaviors vanish if the temporal sequence, spatial locations, or both of the catalytic events on each nanocatalyst are randomized

For a single particle (or a segment), the detected catalytic product formation events occur one at a time, each associated with a microscopic reaction time τ, which is the time separation from the previous event on the same particle (or segment), and with a location

(x,y) where this event occurred. For the n'th event (n is the event index), the absolute time t this event occurred is equal to $\sum_{m=1}^{n} \tau_m$. When we analyzed the cross-correlation coefficient of the microscopic reaction time (τ) between temporally subsequent reactions that occur at different segments on the same particle (i.e., intraparticle) or on different particles (i.e., interparticle), we paired the microscopic reaction time τ of each catalytic event on one segment (or particle) with the microscopic reaction time τ of the immediate subsequent catalytic event that occurs on another segment (or particle). In this way, we obtained many τ-pairs between two segments of the same particle or between two different particles, and then computed the Pearson's cross-correlation coefficient of these catalytic events in *both temporally and spatially defined manner*.

As this cross-correlation coefficient is related to the temporal sequence and spatial locations of individual catalytic reactions, we expected that the correlation, i.e., catalytic communication behavior, would vanish, if we artificially randomize the temporal sequence, spatial locations, or both of the individual reaction events. To randomize the temporal sequence of the catalytic events, we randomly changed the temporal order of catalytic events, for each of which its τ and location (x, y) are maintained (Figure 5.8a). To randomize the spatial locations, we randomly swapped the locations of individual events, for each of which its τ and temporal sequence and thus its absolute occurring time are maintained Figure 5.8b). To randomize both the temporal sequence and spatial locations, we randomly changed the temporal order of each τ, but left the locations in the same order so that for each τ, it has a different location and different occurring time (Figure 5.8c). All these event randomizations do not change the average turnover rate of the particle (or segment), as we do not change the total number of events on each segment (or particle).

a. temporal randomization

Events Index	X_0(nm)	Y_0(nm)	τ(s)	Accumulative Time (s)
1	-62.54	399.17	3.88	3.88
2	-303.9	435.67	2.36	6.24
3	151.38	786.63	9.305	15.545
4	211.51	770.89	2.91	18.455
5	126.17	814.6	0.035	18.49
6	-109.8	350.2	3.13	21.62
7	-268.9	504.21	2.485	24.105
8	-367.3	437	0.025	24.13
9	1502.4	6.35	4.32	28.45
10	179.05	932.72	1.325	29.775
11	248.81	930.1	5.9	35.675
12	141.46	800.88	21.275	56.95
13	645.46	-654.9	8.295	65.245
14	108.82	915.56	16.995	82.24
15	122.46	1102.7	0.265	82.505
16	9.36	1138.5	2.93	85.435
17	112.89	983.15	2.075	87.51
18	113.02	1146.5	2.32	89.83
19	-259	520.58	2.93	92.76
20	221.36	619.19	0.235	92.995

Events Index	X_0(nm)	Y_0(nm)	τ(s)	Accumulative Time (s)
1	-109.8	350.2	3.13	3.13
2	151.38	786.63	9.305	12.435
3	9.36	1138.5	2.93	15.365
4	248.81	930.1	5.9	21.265
5	-268.9	504.21	2.485	23.75
6	112.89	983.15	2.075	25.825
7	108.82	915.56	16.995	42.82
8	-367.3	437	0.025	42.845
9	126.17	814.6	0.035	42.88
10	-259	520.58	2.93	45.81
11	122.46	1102.7	0.265	46.075
12	-62.54	399.17	3.88	49.955
13	-303.9	435.67	2.36	52.315
14	211.51	770.89	2.91	55.225
15	113.02	1146.5	2.32	57.545
16	645.46	-654.9	8.295	65.84
17	1502.4	6.35	4.32	70.16
18	221.36	619.19	0.235	70.395
19	179.05	932.72	1.325	71.72
20	141.46	800.88	21.275	92.995

b. spatial randomization

Events Index	X_0(nm)	Y_0(nm)	τ(s)	Accumulative Time (s)
1	-62.54	399.17	3.88	3.88
2	-303.9	435.67	2.36	6.24
3	151.38	786.63	9.305	15.545
4	211.51	770.89	2.91	18.455
5	126.17	814.6	0.035	18.49
6	-109.8	350.2	3.13	21.62
7	-268.9	504.21	2.485	24.105
8	-367.3	437	0.025	24.13
9	1502.4	6.35	4.32	28.45
10	179.05	932.72	1.325	29.775
11	248.81	930.1	5.9	35.675
12	141.46	800.88	21.275	56.95
13	645.46	-654.9	8.295	65.245
14	108.82	915.56	16.995	82.24
15	122.46	1102.7	0.265	82.505
16	9.36	1138.5	2.93	85.435
17	112.89	983.15	2.075	87.51
18	113.02	1146.5	2.32	89.83
19	-259	520.58	2.93	92.76
20	221.36	619.19	0.235	92.995

Events Index	X_0(nm)	Y_0(nm)	τ(s)	Accumulative Time (s)
1	141.46	800.88	3.88	3.88
2	-109.77	350.2	2.36	6.24
3	645.46	-654.94	9.305	15.545
4	-303.85	435.67	2.91	18.455
5	248.81	930.1	0.035	18.49
6	179.05	932.72	3.13	21.62
7	122.46	1102.67	2.485	24.105
8	9.36	1138.47	0.025	24.13
9	-62.54	399.17	4.32	28.45
10	113.02	1146.49	1.325	29.775
11	126.17	814.6	5.9	35.675
12	108.82	915.56	21.275	56.95
13	-268.91	504.21	8.295	65.245
14	151.38	786.63	16.995	82.24
15	1502.43	6.35	0.265	82.505
16	-259.03	520.58	2.93	85.435
17	211.51	770.89	2.075	87.51
18	221.36	619.19	2.32	89.83
19	-367.26	437	2.93	92.76
20	112.89	983.15	0.235	92.995

c. spatial and temporal randomization

Events Index	X_0(nm)	Y_0(nm)	τ(s)	Accumulative Time (s)
1	-62.54	399.17	3.88	3.88
2	-303.9	435.67	2.36	6.24
3	151.38	786.63	9.305	15.545
4	211.51	770.89	2.91	18.455
5	126.17	814.6	0.035	18.49
6	-109.8	350.2	3.13	21.62
7	-268.9	504.21	2.485	24.105
8	-367.3	437	0.025	24.13
9	1502.4	6.35	4.32	28.45
10	179.05	932.72	1.325	29.775
11	248.81	930.1	5.9	35.675
12	141.46	800.88	21.275	56.95
13	645.46	-654.9	8.295	65.245
14	108.82	915.56	16.995	82.24
15	122.46	1102.7	0.265	82.505
16	9.36	1138.5	2.93	85.435
17	112.89	983.15	2.075	87.51
18	113.02	1146.5	2.32	89.83
19	-259	520.58	2.93	92.76
20	221.36	619.19	0.235	92.995

Events Index	X_0(nm)	Y_0(nm)	τ(s)	Accumulative Time (s)
1	-62.54	399.17	4.32	4.32
2	-303.9	435.67	0.025	4.345
3	151.38	786.63	2.36	6.705
4	211.51	770.89	9.305	16.01
5	126.17	814.6	0.235	16.245
6	-109.8	350.2	2.32	18.565
7	-268.9	504.21	2.91	21.475
8	-367.3	437	16.995	38.47
9	1502.4	6.35	3.88	42.35
10	179.05	932.72	8.295	50.645
11	248.81	930.1	2.93	53.575
12	141.46	800.88	5.9	59.475
13	645.46	-654.9	1.325	60.8
14	108.82	915.56	2.93	63.73
15	122.46	1102.7	0.035	63.765
16	9.36	1138.5	3.13	66.895
17	112.89	983.15	2.485	69.38
18	113.02	1146.5	21.275	90.655
19	-259	520.58	0.265	90.92
20	221.36	619.19	2.075	92.995

Figure 5.8. Illustration of randomization of the individual catalytic events from a single Au nanorod catalyzing the deacetylation reaction. Each catalytic event has a microscopic reaction time τ, a spatial location (x, y), and a temporal sequence represented by its event index. (**a**) Randomization of the temporal sequence of the individual catalytic events. (**b**) Randomization of the spatial locations of individual catalytic events. (**c**) Randomization of both the temporal sequence and spatial locations of individual catalytic events.

After the above randomizations, we re-computed the intra- and inter-particle cross-correlation coefficients ρ_{τ_i,τ_j}. We use the experimental data from the Au nanorods in catalyzing the deacetylation reaction as illustrations here. For intraparticle catalytic communication, the characteristic exponential dependences of ρ_{τ_i,τ_j} on intraparticle Δx_{ij} and $\overline{\Delta t_{ij}}$ vanishes, and it stays essentially flat at the residual value of ~0.03 (Figure 5.9a, b). Similarly, for interparticle catalytic communication, the dependences of ρ_{τ_i,τ_j} on interparticle Δx_{ij} and $\overline{\Delta t_{ij}}$ also vanishes (Figure 5.9c, d); ρ_{τ_i,τ_j} here is flat and has a similar

residual value of ~0.03. These residual values represent the spurious contribution to the cross-correlation coefficient, which is also present in simulations of random catalytic events (Section 5.8 below). *Therefore, the experimental observed Δx_{ij} and $\overline{\Delta t_{ij}}$ dependences of the cross-correlation coefficient ρ_{τ_i,τ_j} are inherently related to the temporal sequence and spatial locations of the individual catalytic events*.

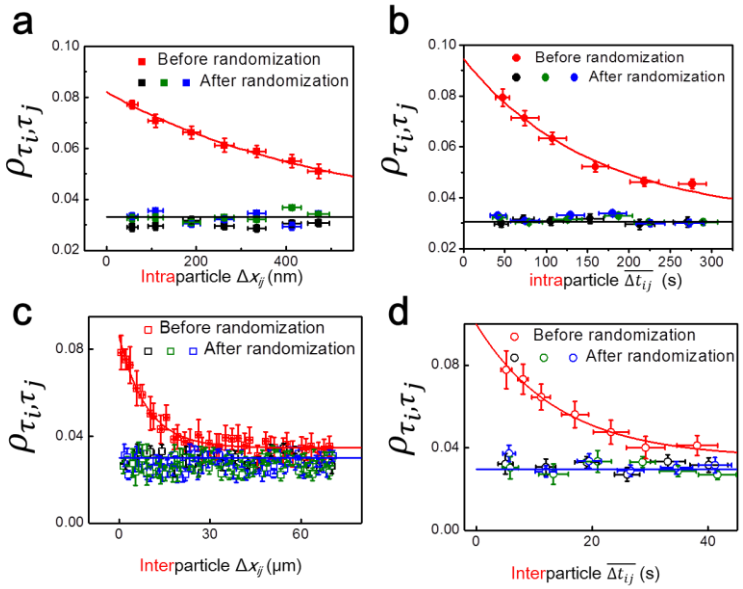

Figure 5.9. Effect of catalytic event randomizations on the cross-correlation coefficient ρ_{τ_i,τ_j} for intra- and inter-particle catalytic communications, using as an example Au nanorods in catalyzing the deacetylation reaction. (**a, b**) ρ_{τ_i,τ_j} vs. intraparticle Δx_{ij} or $\overline{\Delta t_{ij}}$ before and after randomization. (**c, d**) ρ_{τ_i,τ_j} vs. interparticle Δx_{ij} or $\overline{\Delta t_{ij}}$ before and after event randomization. The black, green and blue points represent the temporal, spatial, or both randomizations, respectively. Red lines are all exponential fits. Black or blue lines are the mean values. *x* error bars are s.d. and *y* error bars are s.e.m.

5.8. Simulations show that temporally random catalytic events do not show intra- or inter-particle catalytic communications, but have a spurious residual cross correlation.

As a further control, we performed simulations of catalytic events on single nanorods of various lengths, on which the catalytic events occur in a temporally random fashion, but the time-averaged turnover rate and the spatial distribution of catalytic events match those we experimentally measured, for example Au nanorods in catalyzing the deacetylation reaction[2]. Using the simulated events, we then evaluated whether or not these temporally random catalytic events *would* show intra- and inter-particle catalytic communications.

In the simulation, we used 200 nanorods, each modeled as a rectangle with length in the range of 200 to 600 nm (Figure 5.10b) (i.e., ignoring the two ends that are pseudo-half-spheres), similar to the Au nanorod core length of those studied experimentally (Figure 5.10a). The width of the nanorod core was fixed at 21 nm; this is about the actual average width of the nanorod core of $mSiO_2$-coated Au nanorods, which do not vary much from rod to rod[2]. The nanorods in the simulations were treated as 2-D objects, as our experimental imaging was in 2-D.

For each nanorod of length L in the simulation, its catalytic activity at a specific location along its length was taken from our previous study of Au nanorods in catalyzing the deacetylation reaction of amplex red[2]. In this previous study, we found that these nanorods have an activity gradient along their lengths, with their centers more active, and decaying linearly toward the two ends, attributable to an underlying defect density gradient that is the highest at the center and less toward the two ends. The local catalytic activity

along the length of a single nanorod was found to follow the relationship:

$$k_L(x) = -2\beta_L x + k_{c,L} \qquad \text{Eq. 5.5}$$

where $k_L(x)$, in s^{-1} nm^{-2}, is the catalytic activity at a distance x from the center of a nanorod with length L. Parameter β_L, in s^{-1} nm^{-3}, is the activity gradient from the nanorod center toward the two ends. $k_{c,L}$, in s^{-1} nm^{-2}, is the activity at the center position. Both β_L and $k_{c,L}$ were found to be dependent on the nanorod length L. Using the experimental data from our previous study (Figure 5.10c-d), for each nanorod with a length L, we determined its β_L and $k_{c,L}$, and thus $k_L(x)$, which was used as input parameters for our simulations.

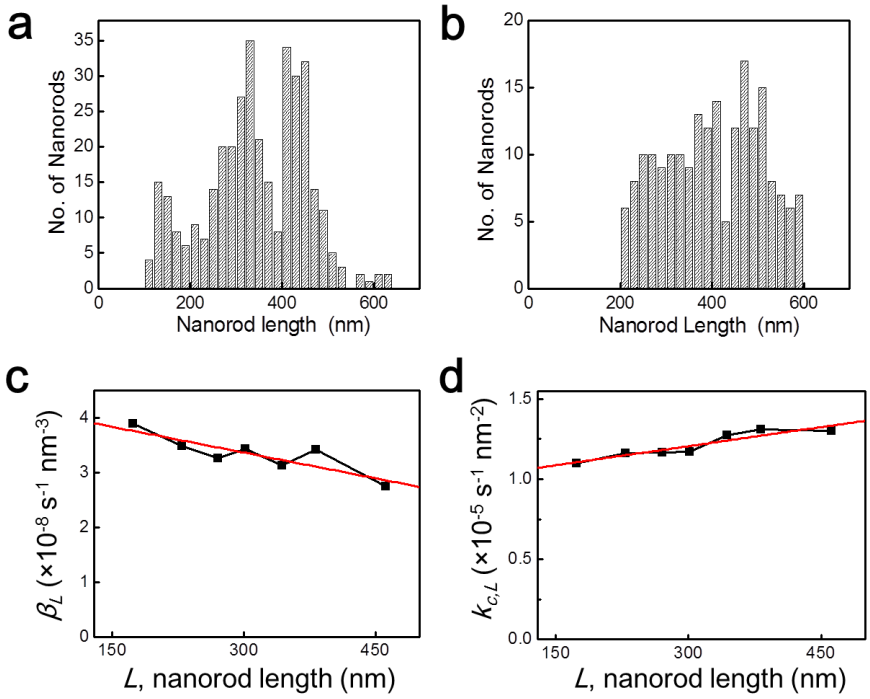

Figure 5.10. Temporally random catalytic events do not show intra- or inter-particle catalytic communications (**a**) Length distribution of the as-synthesized Au nanorods from our previous study[2]. (**b**) Length distribution of the nanorods in simulations**.** (**c, d**) Dependence and linear fitting of β_L and $k_{c,L}$ on nanorod length L from Zhou et al[2]: (**c**) β_L (×10^{-8} s^{-1} nm^{-3}) = –0.00314 L (nm) + 4.314; (**d**) $k_{c,L}$

($\times 10^{-5}$ s^{-1} nm^{-2}) = 0.00079L (nm) + 0.968.In order to assign the spatial locations of the simulated catalytic events on the surface of nanorods, we divide every simulated nanorod into segments with 10 nm in length (a size smaller than the spatial resolution of ~40 nm in our experimental imaging of reaction locations). The local activity $k_L(x)$ (in s^{-1} nm^{-2}) of each segment for a nanorod of length L can then be determined from Eq. 5.5 and data in Figure 5.10c-d. Moreover, the Au surface area of each segment is ~660 nm^2, treating the nanorod as a cylinder with a diameter of 21 nm. Using $k_L(x)$ and the surface area of each segment, the reaction rate (in s^{-1}) of each segment can be obtained, giving rise to a volcano-shaped activity profile from the center toward the two ends (Figure 5.11c). Based on this profile, the number of catalytic events is then sampled for each segment, until the total number of events of the whole nanorod reaches about 8000, which is approximately the number of events we observed experimentally for a single nanorod. Within each segment of 10 nm, the location along the nanorod long axis of each catalytic event is randomly assigned. Considering the real catalyst particles are core-shell nanostructures with a mesoporous SiO_2 shell of ~80 nm in thickness, the positions of simulated events are randomly distributed in the direction perpendicular to the nanorod long axis (Figure 5.11b). By doing so, we can simulate the 2-D spatial distribution of catalytic events on a single nanorod with length L (Figure 5.11a).

We next determined the microscopic reaction time τ for each catalytic event in the simulation within the event sequence for the *whole* nanorod. For temporally random catalytic events in which the catalytic kinetics contains one rate-limiting step, the distribution of τ follows a single-exponential decay, where the exponential time constant is equal to $\langle \tau \rangle$. Here, $\langle \tau \rangle^{-1}$ is equivalent to the average reaction rate of the nanorod as whole,

which can be obtained from the reaction rates of all segments described above. Therefore, the exponential distribution of τ can be determined for a nanorod of length L (Figure 5.11d). All the catalytic events, whose spatial distribution on the nanorod was determined earlier, were then assigned a microscopic time τ by sampling the exponential distribution. Taken all together, the simulation produces a sequence of catalytic events that are temporally random (e.g., Figure 5.11e), but spatially follow the distribution observed experimentally, and have a time-averaged rate consistent with experimental data.

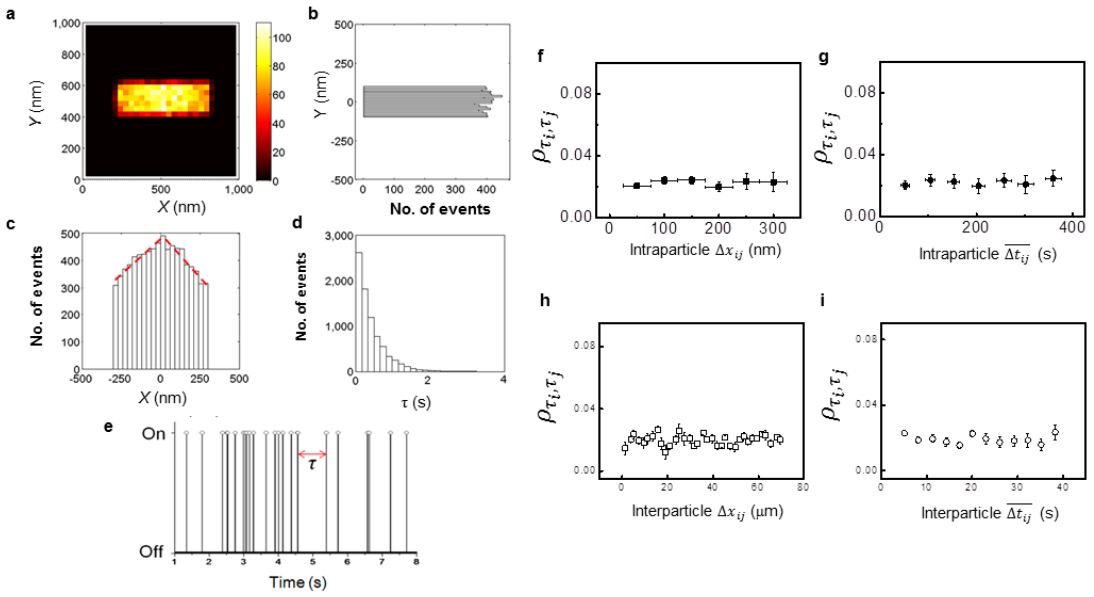

Figure 5.11. Simulated temporally random catalytic events do not show intra- and inter-particle catalytic communication behaviors. (a-e) Exemplary simulated catalytic events on a single nanorod of length = 500 nm. (**a**) Two-dimensional spatial histogram of catalytic events in 20 × 20 nm^2 bins. The two hemisphere ends are omitted here, as we did not include in the analysis of experimental data either. (**b, c**) Spatial distributions of catalytic events perpendicular to (**b**) and along (**c**) the nanorod long axis. Red dash lines in **c** indicate the linear gradient of catalytic activity from the center toward the two ends along the nanorod length as described by Eq. 5.5. (**d**) Distribution of τ of the simulated catalytic events follows a single exponential distribution. (**e**) A segment of simulated time trajectory

of event sequence for the whole nanorod. (**f-i**) **Cross-correlation coefficient ρ_{τ_i,τ_j} for probing intra- and inter-particle catalytic communications obtained from simulations as those in a-e**. (**f, g**) intraparticle ρ_{τ_i,τ_j} vs. the intraparticle distance separation Δx_{ij} or average time separation $\overline{\Delta t_{ij}}$. (**h, i**) Same as (**f, g**) but for interparticle ρ_{τ_i,τ_j}.

Using the simulated results of the 200 nanorods of various lengths, we performed the cross-correlation analysis to probe the existence of *intraparticle* catalytic communication, as we did on experimental results. To analyze potential *interparticle* catalytic communication using the simulated results, we needed to assign positions to these 200 nanorods. Here we used the locations of nanorods on the quartz slide that we studied experimentally, and assigned these experimental locations randomly to the 200 simulated nanorods.

For the intraparticle analysis, Figure 5.11f and g show ρ_{τ_i,τ_j} vs. the intraparticle distance separation Δx_{ij} and the average time separation $\overline{\Delta t_{ij}}$ between temporally subsequent catalytic events on different segments. No exponential decay behavior of ρ_{τ_i,τ_j} is observed with increasing Δx_{ij} or $\overline{\Delta t_{ij}}$, and ρ_{τ_i,τ_j} stays flat at a residual value of ~0.02, which represents a spurious contribution. Therefore, temporally random catalytic events do not show intraparticle catalytic communications. Figure 5.11h and i show the corresponding data for interparticle analysis. Again, ρ_{τ_i,τ_j} does not show any decay behavior with increasing interparticle distance separation Δx_{ij} and average time separation $\overline{\Delta t_{ij}}$ between temporally subsequent events on different nanorods, and it stays flat at ~0.02, which again represents a spurious contribution from random events to the cross-correlation coefficient. The

independence of ρ_{τ_i,τ_j} on Δx_{ij} or $\overline{\Delta t_{ij}}$ here demonstrates that temporally random catalytic events do not show interparticle catalytic communications, either.

Altogether, the results from these simulations support that the intra- and inter-particle catalytic communications we observed experimentally are inherently related to the temporal relationship of the individual catalytic events, and that temporally random events do not possess similar properties.

5.9. Resorufin rebinding to nanocatalysts contributes to ~0.3% of the detected events and does not give rise to intra- or inter-particle catalytic communication behaviors

To ensure that the rebinding of the catalytic product resorufin to the nanocatalysts is not the cause for the observed intra- and inter-particle catalytic communications, we performed a control experiment where we followed in 5 nM resorufin into the microfluidic reactor and imaged resorufin binding to single nanocatalysts, using the $mSiO_2$-coated Au nanorods as a representative. Based on the background fluorescence level in the flow reactor, which is proportional to the concentration of resorufin in the solution, this 5 nM resorufin is about 10 times larger than the steady-state concentration of resorufin generated during the catalytic reaction under similar laser excitation and solution flow conditions. Figure 5.12a shows that even under this 10× higher concentration of resorufin, the rate of detected events on a single Au nanorod is only ~3% of those detected during the Au nanorod catalyzed AR deacetylation and Rz deoxygenation reactions, *demonstrating that resorufin rebinding has no significant contribution (i.e., ~0.3%) to the detected events in catalysis*. The rate per Pd nanorod in the catalytic reaction is even larger due to the larger size of the particle. The

average fluorescence on-time of individual resorufin in this rebinding control experiment is the same as those measured in the three catalytic reactions (~40 ms) (Figure 5.12b), consistent with that the on-time is the adsorption of the product resorufin within the mesoporous of the $mSiO_2$ shell of the Pd/Au nanocatalysts, which should not differ when the resorufin is generated catalytically or rebound from the solution.

Using the detected resorufin rebinding events on single Au nanorods in this control experiment, we calculated the same cross-correlation coefficient ρ_{τ_i,τ_j} between temporally subsequent *adsorption* events that occur at different segments or at different nanorods. For both the intra- and inter-particle ρ_{τ_i,τ_j}, there are no trends of ρ_{τ_i,τ_j} being positive and decaying exponentially with increasing distance and average time separations between the temporally subsequent events (Figure 5.12c-f). *Therefore, rebinding of resorufin to the nanocatalysts, even if it were to contribute to the detected events, does not give rise to the intra- and inter-particle communication behaviors.*

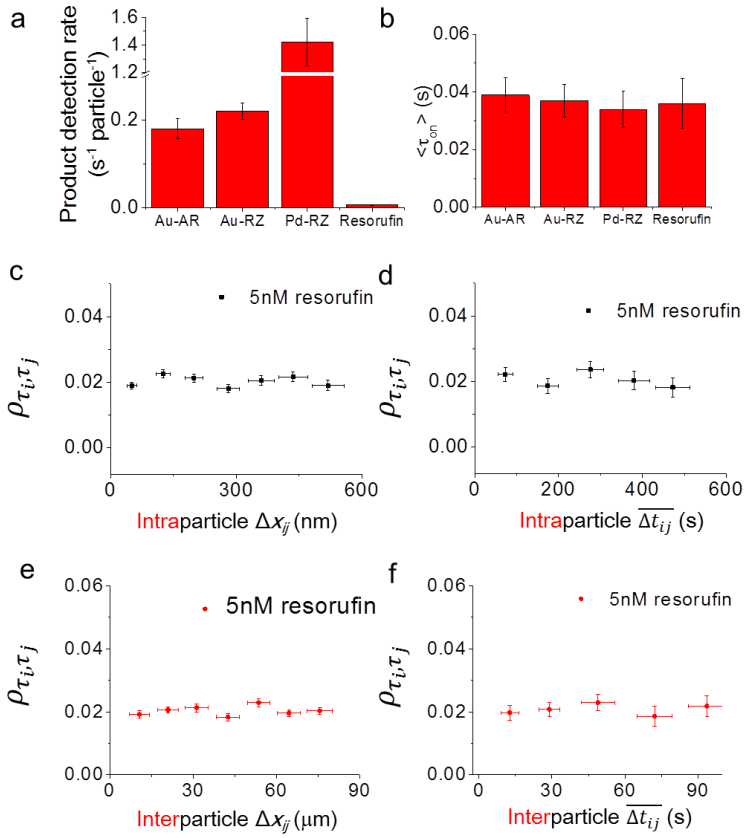

Figure 5.12. Resorufin rebinding to nanocatalysts contributes to ~0.3% of the detected events. (**a**) Average product detection rates in the Au-nanorod-catalyzed AR deacetylation reaction, Au-nanorod-catalyzed Rz deoxygenation reaction, Pd-nanorod-catalyzed Rz disproportionation reaction, and the resorufin rebinding at 5 nM on single Au nanorods. The data are averaged over 62, 56, 45, and 43 nanorods respectively. (**b**) The average fluorescence on-time in the four experiments as in **a**. (**c, d**) Pearson's cross-correlation coefficient $\rho_{\tau_i,\tau_j}(\Delta x_{ij}, \overline{\Delta t_{ij}})$ vs. the intraparticle distance separation Δx_{ij} or the average time separation $\overline{\Delta t_{ij}}$ of temporally subsequent adsorption events at two different segments on the same Au nanorod in the resorufin adsorption control experiment. (**e, f**) Same as **c**, **d**, but between adsorption events that occur on different nanorods.

5.10. Additional experimental results.

5.10.1. Additional results on Pd nanorods in catalyzing Rz disproportionation.

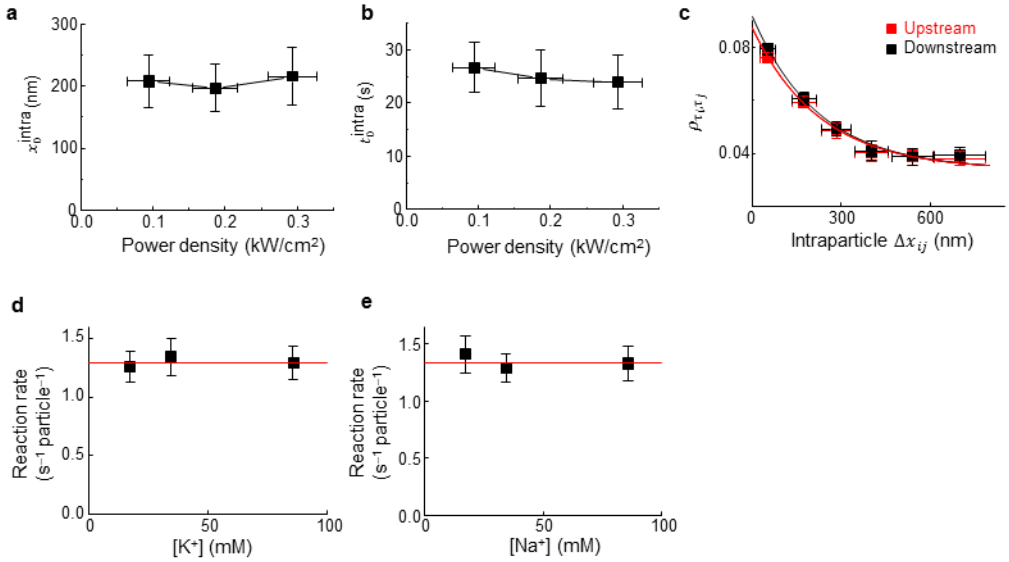

Figure 5.13. Additional results on the intraparticle catalytic communication within single Pd nanorods in catalyzing the photo-driven Rz disproportionation. (a-b) Laser power has no effect: x_0^{intra} (**a**) and t_0^{intra} (**b**) vs. the 532 nm laser excitation power density; no significant dependence is discernable. (**c**) **Solution flow has no effect:** Cross-correlation coefficient ρ_{τ_i,τ_j} vs. the intraparticle distance separation Δx_{ij} when the i-to-j intraparticle vector is pointed downstream ($\theta = 13\pm3°$) or upstream ($\theta = 193\pm3°$) along the solution flow at 180 μm s^{-1} flow rate. No significant differences are observed between the two curves. (**d, e**) **Spectator cations have no effect on Pd nanorod activity**. The averaged single-particle catalytic rate of Pd nanorods as a function of $[K^+]$ and $[Na^+]$ in the solution. The K^+ and Na^+ concentrations were varied by varying the buffer concentrations, in which they are the counter cations.

5.10.2. Additional results on Au nanorods in catalyzing AR deacetylation.

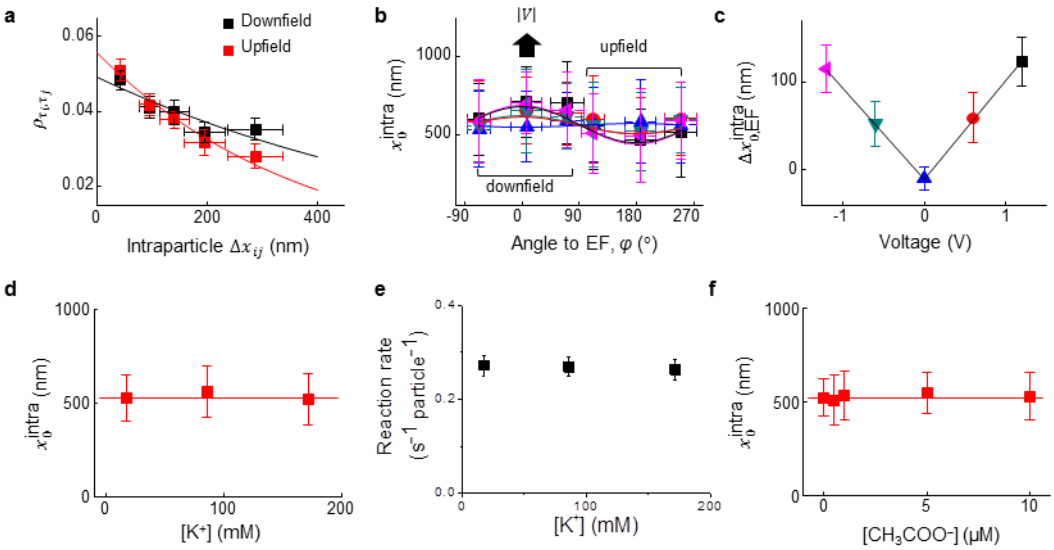

Figure 5.14. Additional results on the intraparticle catalytic communication of Au nanorods in catalyzing AR deacetylation. (a-c) EF effects indicate that the messenger for the intraparticle catalytic communication here is a positively-charged species: (**a**) ρ_{τ_i,τ_j} vs Δx_{ij} when the i-to-j intraparticle vector is pointed downfield ($\varphi = 14 \pm 5°$) or upfield ($\varphi = 194 \pm 5°$) along the EF direction at 1.2 V. Lines: all exponential fits. (**b**) x_0^{intra} vs. orientation angle φ to the EF direction at various voltages. Lines: fits with cosine function Eq. 5.1 (**c**) Cosine function amplitude $\Delta x_{0,\text{EF}}^{\text{intra}}$ vs. voltage from **c**. Symbols color-coded as in **c**; lines are eye-guides. (**d-e**) **Spectator cation does not affect the intraparticle catalytic communication or the reaction kinetics (**in this catalytic reaction, the only spectator cation is K^+, which comes from the phosphate buffer; the two reactants, amplex red and H_2O_2, were both obtained in their neutral forms**):** x_0^{intra} (**d**) vs. [K^+] in solution; no significant dependence is discernable. (**e**) The catalytic activities of single $mSiO_2$-coated Au nanorods are independent of [K^+] in the reaction solution. Data averaged over 46 nanorods. The [K^+] was varied by using a range of phosphate buffer concentrations (pH maintained at 7.2), in which the counter cation is K^+. (**f**) **The product acetate has no effect:** x_0^{intra} vs. externally added [CH_3COO^-]; no

significant dependence is discernable.

5.10.3. Results on Au nanorods in catalyzing Rz deoxygenation.

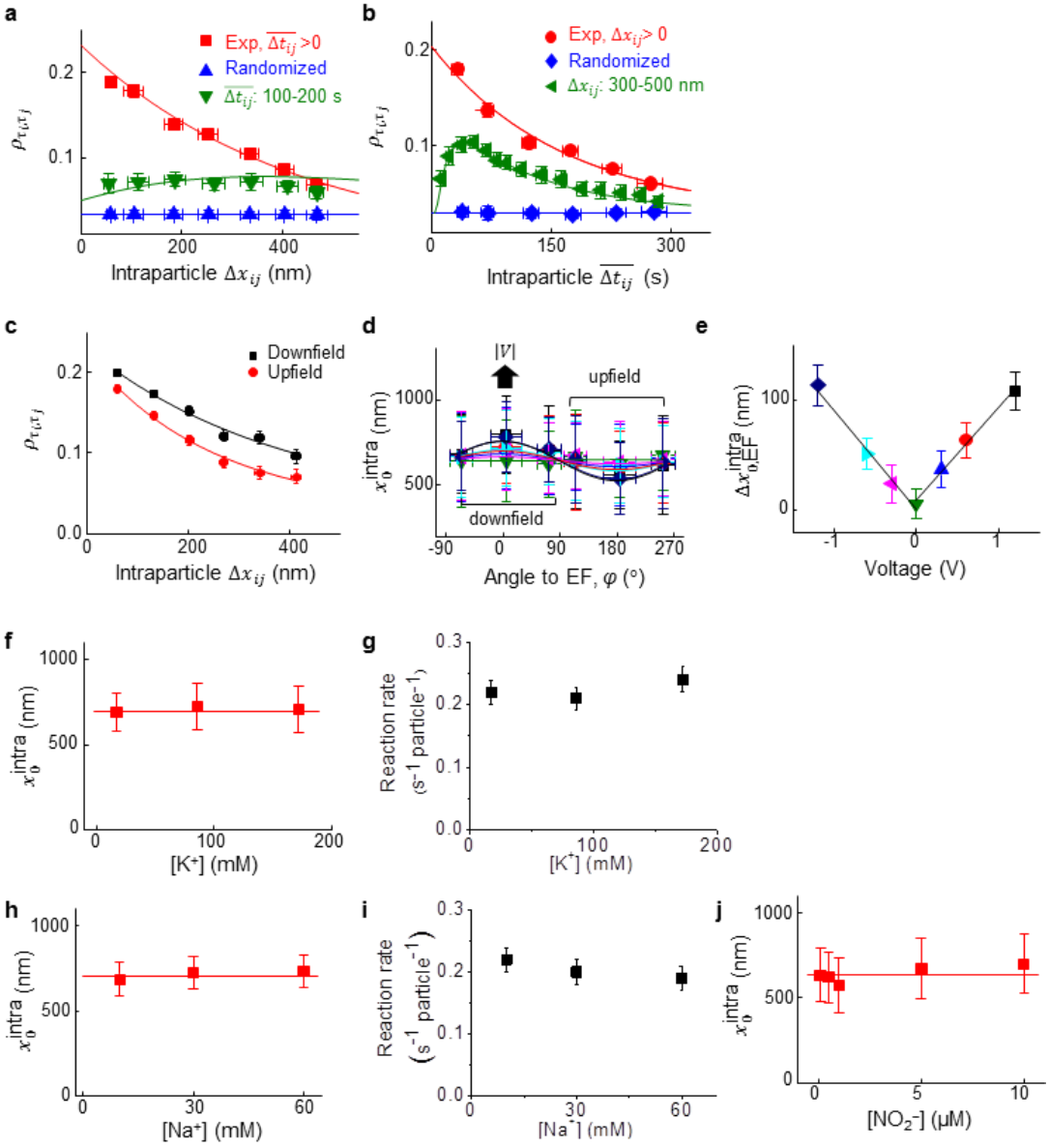

Figure 5.15. Results on intraparticle catalytic communication within single Au nanorods catalyzing Rz deoxygenation. (**a,b**) Pearson's cross-correlation coefficient ρ_{τ_i,τ_j} vs. the intraparticle distance separation Δx_{ij} or the average time separation $\overline{\Delta t_{ij}}$ of temporally subsequent reactions at different

segments on the same nanorod (red), and after spatial (**a**) or temporal (**b**) randomization of the catalytic events (blue), and when $\overline{\Delta t_{ij}}$ or Δx_{ij} is constrained (green). Note the cross-correlation amplitudes here are 0.213 ± 0.045 (**a**) and 0.183 ± 0.068 (**b**), significantly larger than that for the AR deacetylation reaction in Figure 4.1d-e, indicating that the strength of intraparticle catalytic communication can vary depending on the catalytic reaction. Data averaged over >750 segments from >170 nanorods. Red lines: exponential fits with distance constant x_0^{intra} = 624 ± 180 nm and time constant t_0^{intra} = 168 ± 36 s. Complete fitting parameters in Table 4.2. Blue lines: horizontal fits. Green lines: fits with Eq. 4.16 and 4.22. x error bars are s.d. y error bars are s.e.m. (**c-e**) **EF effects indicate that the messenger for the intraparticle catalytic communication here is a positively-charged species:** (**c**) ρ_{τ_i,τ_j} vs Δx_{ij} when the i-to-j intraparticle vector is pointed downfield (φ = 15 ± 5°) or upfield (φ = 195 ± 5°) along the EF direction at 1.2 V. Lines: all exponential fits. (**d**) x_0^{intra} vs. orientation angle to the EF direction at various voltages, fitted with cosine function Eq. 5.1; (**e**) the cosine function amplitude $\Delta x_{0,\text{EF}}^{\text{inter}}$ vs. voltage from **d**. Symbols color-coded correspondingly. (**f-i**) **Spectator counter cations do not affect the intraparticle catalytic communication or the reaction kinetics (**in this catalytic reaction, the spectator cations are K^+, which comes from the phosphate buffer, and Na^+, which comes from the counter cation of the resazurin salt and NaOH that was used to neutralize $NH_2OH{\cdot}HCl$, a co-reactant): x_0^{intra} (**f** and **h**) vs. $[K^+]$ or $[Na^+]$ in the solution; no significant dependence is discernable. The $[K^+]$ concentration was varied by using a range of phosphate buffer concentrations (pH maintained at 7.2), in which the counter cation is K^+. The $[Na^+]$ was varied by using different concentrations of the co-reactant NH_2OH that was obtained commercially in the form of $NH_2OH{\cdot}HCl$ and neutralized by various amounts of NaOH. At this range of $[NH_2OH]$, the reaction kinetics is pseudo-zeroth order to $[NH_2OH]$[12,14]. (**g**,**i**) The catalytic activities of single Au nanorods are independent of $[K^+]$ or $[Na^+]$ in the reaction solution. Data averaged over 57 nanorods. (**j**) **The product nitrite has no effect:** x_0^{intra}

vs. externally added [NO_2^-]; no significant dependence is discernable.

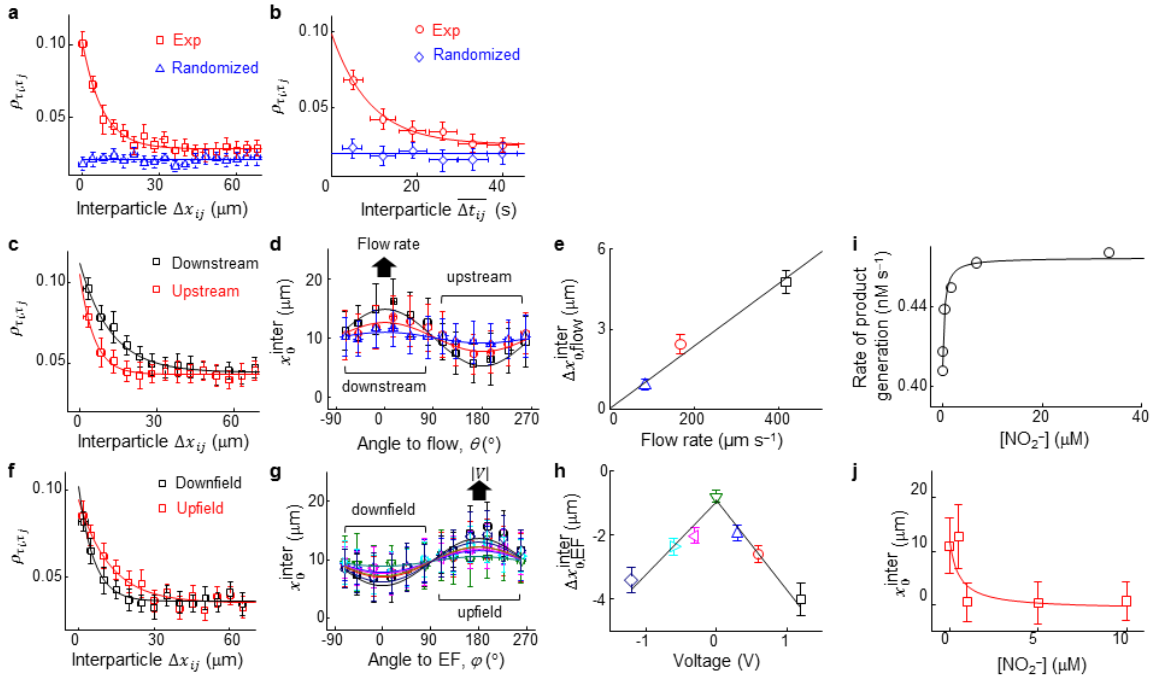

Figure 5.16. Results on the *inter*particle catalytic communication between individual Au nanorods in catalyzing Rz deoxygenation. (**a**,**b**) Pearson's cross-correlation coefficient ρ_{τ_i,τ_j} vs. the interparticle distance separation Δx_{ij} or the average time separation $\overline{\Delta t_{ij}}$ of temporally subsequent reactions at two different nanocatalysts (red) and after spatiotemporal randomizations (blue). Data averaged over >170 nanocatalysts. Red lines: exponential fits with distance constant $x_0^{\text{inter}} = 8.6 \pm 2.2$ μm and time constant $t_0^{\text{inter}} = 7.7 \pm 1.4$ s, and offsets = 0.032. Blue lines: horizontal fits. (**c-h**) **Solution flow and EF effects show that the interparticle catalytic communication occurs via a molecular diffusion mechanism, involving a negatively-charged species:** (**c**, **f**) ρ_{τ_i,τ_j} vs. Δx_{ij} when the *i*-to-*j* interparticle vector is pointed downstream ($\theta = 15 \pm 4°$) or upstream ($\theta = 195 \pm 4°$) along the solution flow at 415 μm s^{-1} flow rate (**c**), or pointed downfield ($\varphi = 14 \pm 5°$) or upfield ($\varphi = 194 \pm 5°$) along the EF direction at 1.2 V (**f**). Lines: all exponential fits. (**d**,**g**) Dependences of the interparticle catalytic communication distance x_0^{inter} on the orientation angle relative to the flow

direction at various flow rates (**d**) and to the EF direction at various voltages (**g**). Lines: fits with cosine function Eq. 5.1. (e,**h**) Cosine function amplitude $\Delta x_{0,\mathrm{flow}}^{\mathrm{inter}}$ vs. flow rate from **d**, and amplitude $\Delta x_{0,\mathrm{EF}}^{\mathrm{inter}}$ vs. voltage from **g**. Symbols color-coded as in **d** and **g**. The negative voltages in **h** indicate flipping electrode bias. Lines: linear eye-guide. (**i,j**) **The reaction product NO_2^- is the interparticle catalytic messenger molecule:** (**i**) Initial product formation rate vs. [NO_2^-] in the solution at the ensemble level. Single-particle level data are in Figure 5.26. B. Line: fit with saturation function Eq. 5.2; $K_{1/2}$ = 0.46 ± 0.14 μM. (**j**) x_0^{inter} vs. [NO_2^-]. Line: fit with saturation function Eq. 5.3; $K_{1/2}$ = 0.53 ± 0.12 μM. X error bars in **a-d**, **f-g** are s.d. Y error bars in **a-c, f** are s.e.m., in **d-e, g-j** are s.d.

5.10.4. Results on Au nanoplates in catalyzing Rz deoxygenation.

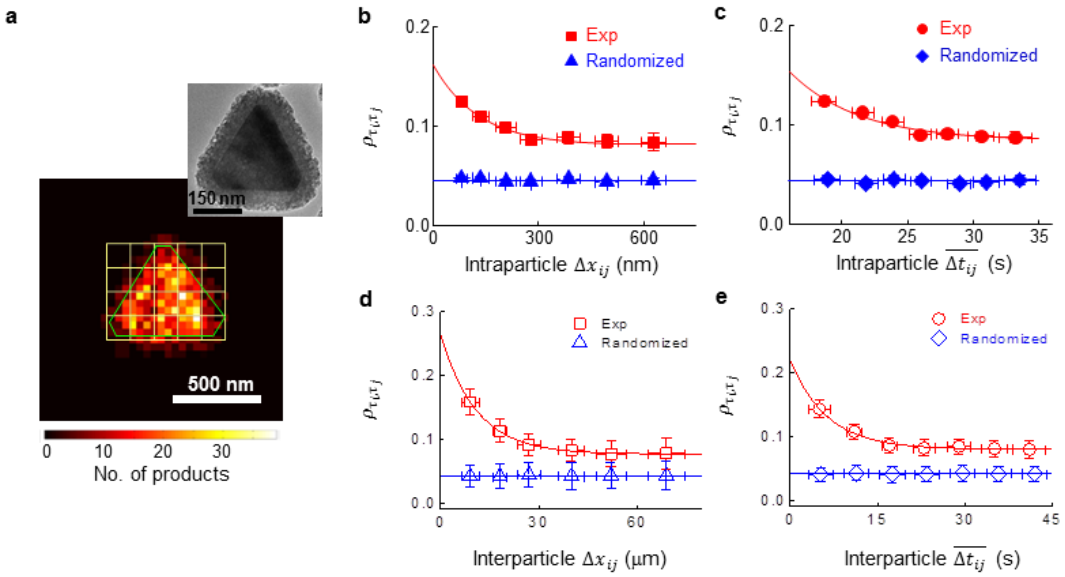

Figure 5.17. *Intra-* and *inter*-particle catalytic communication of single Au nanoplates in catalyzing Rz deoxygenation. (**a**) Two-dimensional histogram of ~2350 fluorescent product molecules in 40×40 nm^2 bins from a single $mSiO_2$-coated Au nanoplate, mapped onto its SEM structural contour (green line; Figure 5.4i). Yellow lines dissect the nanoplate into ~150×150 nm^2 square segments. Inset: TEM of a representative $mSiO_2$-coated Au nanoplate. (**b**, **c**) Pearson's cross-correlation coefficient

ρ_{τ_i,τ_j} vs. the intraparticle distance separation Δx_{ij} or the average time separation $\overline{\Delta t_{ij}}$ of temporally subsequent reactions at different segments on the same nanoplate (red), and after spatial (**b**) or temporal (**c**) randomization of the catalytic events (blue). Data averaged over ~520 segments from ~50 nanoplates. Lines: exponential fits with distance constant x_0^{intra} = 130 ± 22 nm and time constant t_0^{intra} = 5.5 ± 0.6 s. Complete fitting parameters summarized in Table 5.2. (**d, e**) Same as **b**-**c**, but for interparticle cases. Lines: exponential fits with distance constant x_0^{inter} = 11.5 ± 0.7 μm and time constant t_0^{inter} = 6.2 ± 0.6 s. X error bars are s.d. Y error bars are s.e.m.

5.10.5. The temporal memories t_0 of both intra- and inter-particle catalytic communications are unaffected by the solution flow, electric field, and presence of cations and anions in the solution: Au nanorods in AR deacetylation reaction as an example.

No effect on the temporal memory of intraparticle catalytic communications. The temporal memories t_0^{intra} of intraparticle catalytic communications within single Pd and Au nanorods show no significant dependence on the nanorod's orientation to the solution flow direction or the EF direction (e.g., Figure 5.18a-b). The independence on the solution flow is expected, as the catalytic reactions occur on the metal surface and the $mSiO_2$ shell would shield any influence from the solution flow on intraparticle processes. The independence on the EF is also consistent with our proposed hole migration mechanism, in which a surface localized hole is a catalytic messenger. In this mechanism, the temporal memory should correspond to the lifetime of this surface hole on the catalyst particle, which is likely not to be dependent on externally applied EF. The independence of t_0^{intra} on externally added anions or cations is expected (e.g., Figure 5.18c-d), as these anions and cations play no roles

in intraparticle catalytic communication.

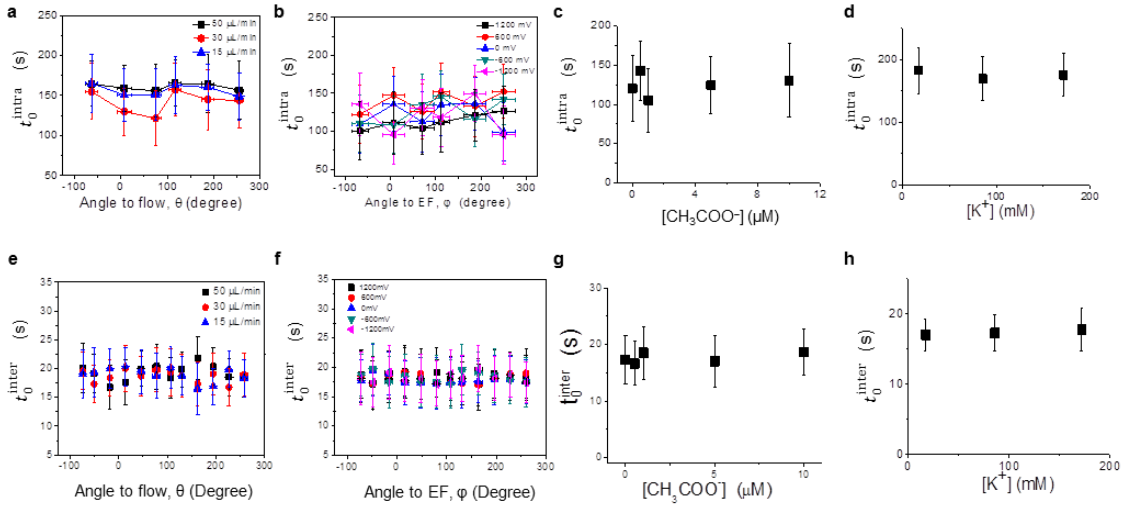

Figure 5.18. The temporal memories t0 of both intra- and inter-particle catalytic communications are unaffected. The temporal memories of intraparticle (**a-d**) and interparticle (**e-h**) catalytic communication of Au nanorods in catalyzing AR deacetylation do not change significantly across a range of solution flow, electric field, product anion, and spectator cation conditions. Intra- and inter-particle catalytic communication temporal memory vs. the inter-nanorod orientation angle θ to the solution flow direction (**a**, **e**), the angle φ to the EF direction (**b, f**), externally added [CH_3COO^-] (**c, g**), and spectator cation [K^+] in the solution (**d**, **h**); no significant dependence is discernable in any case.

No effect on the temporal memory of interparticle catalytic communications because the messenger molecules spent <0.1% of its diffusing time in the solution. The temporal memories t_0^{inter} of interparticle catalytic communications between individual Au nanorods show no significant dependence on the inter-nanorod vector orientation to the solution flow direction or the EF direction or on the added anionic interparticle catalytic messenger (e.g., Figure 5.18e-g), even though the mechanism here is the diffusion of negatively-charged product molecule (acetate or nitrite). Below we provide explanations of these

independences.

Because of the molecular diffusion mechanism, the temporal memory t_0^{inter} of interparticle catalytic communication corresponds to the average time that takes for the messenger molecule (i.e., acetate or nitrite) to diffuse from the Au surface of a nanocatalyst to reach the Au surface of another nanocatalyst at a distance away. This distance corresponds to the interparticle catalytic communication distance x_0^{inter}, and it includes the distance in the solution (L_{solution}) and the distances in the $mSiO_2$ shell (L_{shell}) on both nanocatalysts through which the messenger molecule has to travel through via diffusion (Scheme 5.1):

$$x_0^{\text{inter}} = L_{\text{solution}} + 2L_{\text{shell}} \qquad \text{Eq. 5.6}$$

L_{shell} = 85 nm, which is the average thickness of the $mSiO_2$ shell on the Au nanorods. For nanorods in catalyzing the AR deacetylation reaction, x_0^{inter} = 10.5 μm (Table 5.2), and thus L_{solution} = 10.33 μm.

Scheme 5.1. Components of the interparticle catalytic communication distance, which includes the shell thickness on two Au nanocatalysts and the distance within the solution that the messenger molecule needs to travel through. The nanocatalysts are approximated here as spheres to omit the geometric anisotropy of nanorods.

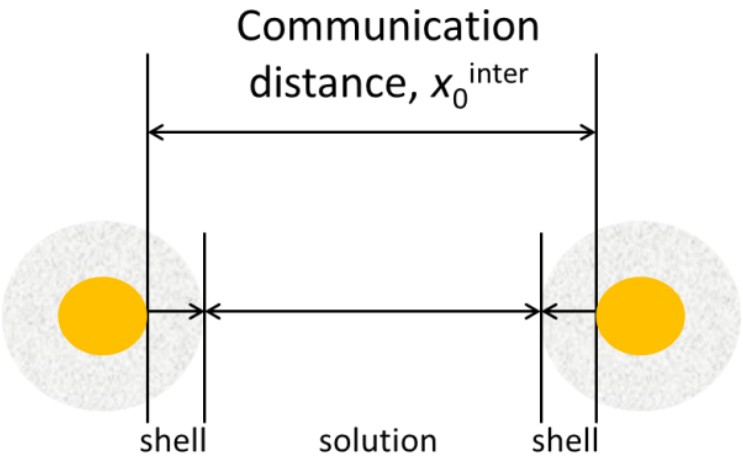

Within each travel segment, the messenger molecule's travel distance should follow the 2-dimensional Brownian diffusion behavior, $L^2 = 4Dt$, where t is the time spent in each of the travel segment (note our imaging is 2-dimensional projection). And the total travel time corresponds to t_0^{inter} (=18.1 s, for nanorods in AR reaction; Table 4.2), which includes both the time spent in the solution ($t_{solution}$) and that in each of the two shells (t_{shell}) on the two nanocatalysts:

$$t_0^{inter} = t_{solution} + 2t_{shell} \quad \text{Eq. 5.7}$$

The diffusion coefficient of acetate in solution ($D_{solution}$) is 1.7×10^{-9} m^2 s^{-1}.[41] Therefore,

$$t_{solution} = \frac{(L_{solution})^2}{4D_{solution}} = 0.016 \text{ s} \quad \text{Eq. 5.8}$$

$$t_{shell} = \frac{t_0^{inter} - t_{solution}}{2} = 9.09 \text{ s} \quad \text{Eq. 5.9}$$

Therefore, the messenger molecule that diffuses to mediate interparticle catalytic communication only spends a <0.1% of its diffusing time in the solution (i.e., $t_{solution}/t_0^{inter}$ = (0.016 s)/(18.1 s) × 100% = 0.09%, < 0.1%), and >99.9% of its time is spent diffusing

through the two $mSiO_2$ shells. It is thus not surprising that the solution flow and EF do not change the temporal memories of interparticle catalytic communication.

Similarly, the independence of t_0^{inter} on the externally added [acetate] or [nitrite] is expected, as the major component of t_0^{inter} is the diffusion time within the $mSiO_2$ shell of the interparticle catalytic messenger (i.e., acetate or nitrite), not that in the solution. The independence on the added cation is expected (Figure 5.18h), as the cations do not play a role in interparticle catalytic communications.

5.11. The intraparticle catalytic communication distance x_0^{intra} and temporal memory t_0^{intra} are independent of experimental time resolution, segment size, catalytic activity, and fluorescence intensity threshold.

Here we present controls regarding our data analysis procedures, using as examples the data from Au nanorods in catalyzing the deacetylation reaction.

5.11.1. They are independent of experimental time resolution within experimental error.

Here we binned every two consecutive frames in the original fluorescence movie so that the image exposure time increased by a factor of two (i.e., time resolution decreased by 2 times) and analyzed the subsequent results. The results are summarized in Figure 5.19 below.

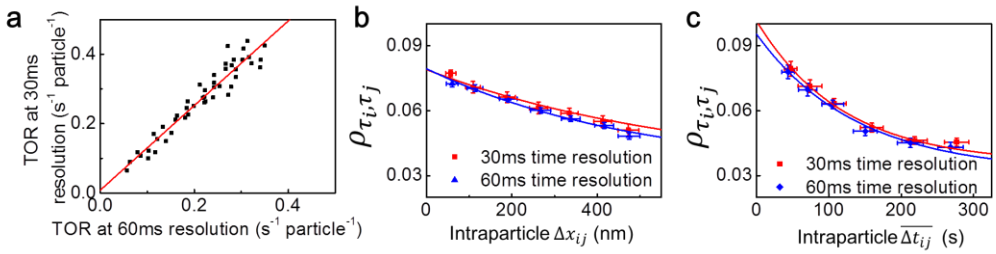

Figure 5.19. Examination of intraparticle catalytic communication vs. experimental time resolution for Au nanorods in catalyzing the AR deacetylation. (**a**) Correlation of measured single-particle turnover rate at 30 ms and 60 ms time resolution. Each dot is for one nanorod. The line is a linear fit with the slope of 1.22 ± 0.05, bigger than one, indicating that at lower time resolution (i.e., 60 ms) the observed turnover rate for each nanorod is lower. This slower apparent turnover rate is expected, because the decrease in time resolution will lead to missing detection of some of the faster (i.e., shorter fluorescence on-time) catalytic events. (**b,c**) Dependence of the intraparticle cross-correlation coefficient ρ_{τ_i,τ_j} on the intraparticle distance separation Δx_{ij} (**b**) or average time separation $\overline{\Delta t_{ij}}$ (**c**) at the two different time resolutions. Exponential fits (lines) in b gives the intraparticle catalytic communication distance x_0^{intra} of 518 ± 160 nm at 30 ms time resolution and 502 ± 148 nm at 60 ms time resolution, within error bars of each other; residual correlation offset at 0.032 ± 0.005. Exponential fits in c gives the intraparticle catalytic communication temporal memory t_0^{intra} of 128 ± 32 s at 30 ms time resolution and 137 ± 26 s at 60 ms time resolution, also within error bars of each other; residual correlation offset at 0.034 ± 0.009. Y error bars in b and c are s.e.m. X error bars in b and c are s.d. Therefore, the intraparticle catalytic communication distance x_0^{intra} and its temporal memory t_0^{intra} are independent of the experimental time resolution. Note that practically, the time resolution cannot be too slow to dis-allow sufficient detection of catalytic events; otherwise, the imaging experiments would not be possible.

5.11.2. They are independent of the segment length in dissecting the individual nanorods

We examined the dependences of the intraparticle communication distance x_0^{intra} and temporal memory t_0^{intra} on the segment length. As our spatial resolution is about ~40 nm,[42] making the segment shorter than 40 nm is meaningless. On the other hand, if the length of segments is too long, very few segments could be obtained on a single nanorod that has a limited length of up to ~700 nm. Therefore, we varied the segment length from 38 nm to 95 nm (Figure 5.20).

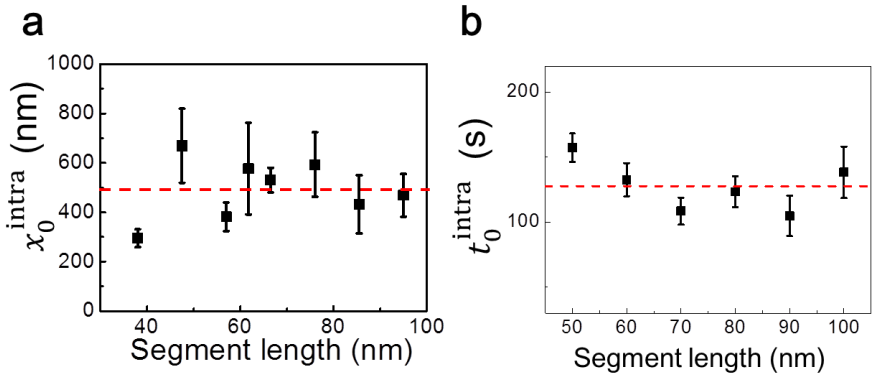

Figure 5.20. Intraparticle catalytic communication distance x_0^{intra} and temporal memory t_0^{intra} vs. the segment length for Au nanorods in catalyzing the deacetylation of AR. **Both x_0^{intra} and t_0^{intra} are essentially independent of the segment length.** The dash lines mark the overall averages. The *y*-error bars are s.d.

5.11.3. They are independent of the nanorod's catalytic activity.

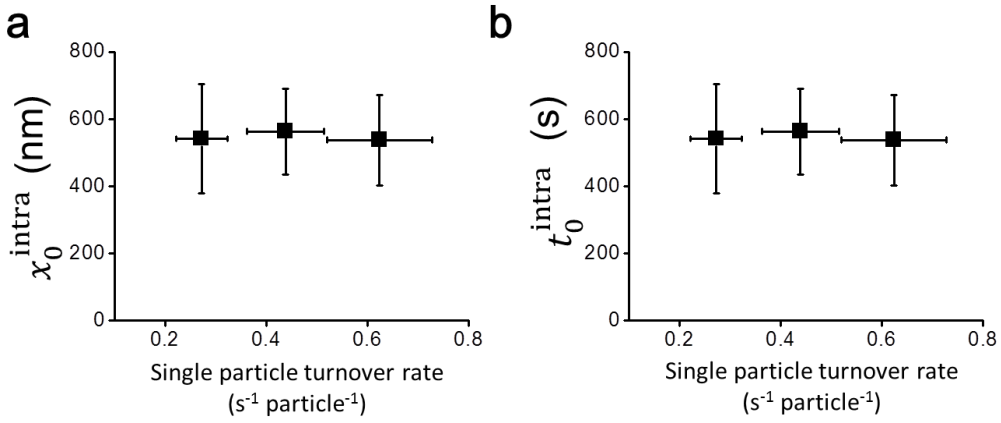

Figure 5.21. Intraparticle catalytic communication distance x_0^{intra} and temporal memory t_0^{intra} vs. single-particle turnover rate (i.e., activity) for Au nanorods in catalyzing the deacetylation of AR. Within each batch of sample, individual nanorods show natural heterogeneity in catalytic activity, allowing us to sort them into three groups of different catalytic activity, analyzing them in each group to determine the dependence on the single-nanorod activity. **Both x_0^{intra} and t_0^{intra} are essentially independent of the nanorod's catalytic activity.** The *x*,*y* error bars are s.d.**They are independent of the fluorescence intensity threshold for selecting catalytic events on each nanocatalyst.**

In analyzing the original fluorescence movies of catalytic product formations, we automated the selection of the fluorescence burst signals by initially thresholding the fluorescence intensity vs time trajectory from a single nanocatalyst (see data analysis procedures in Section 5.4). The value of the threshold was optimized by comparing the data from a nanocatalyst under catalysis with those from a sample area that has no catalyst (i.e., fluorescence background trajectory). The value of the threshold (4.5σ) was also set in the units of the standard deviation σ of the fluorescence background trajectory. After

thresholding, the corresponding images of the selected fluorescence bursts were further analyzed by point-spread-function fitting, in which we obtained the fluorescence spot size, location, and integrated photon counts that could be further used to differentiate true fluorescence signals of single molecules from random background noises.

To probe if this initial fluorescence intensity threshold affects the intraparticle catalytic communication behavior, we analyzed the same experimental data while varying the threshold from 3σ to 5σ, again using the Au nanorods catalyzed AR deacetylation reaction as an example (Figure 5.22).

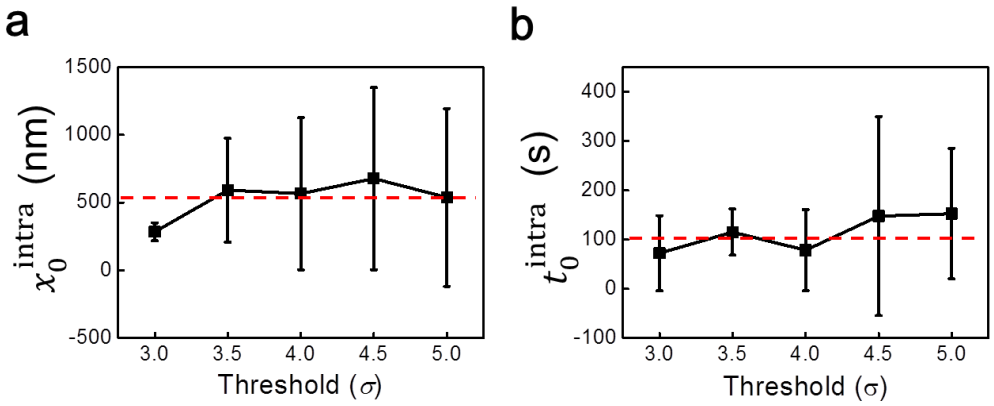

Figure 5.22. Intraparticle catalytic communication distance x_0^{intra} and temporal memory t_0^{intra} vs the fluorescence intensity threshold. The dash lines represent the average values, which are 532 ± 148 nm and 113 ± 37 s, respectively. The y-error bars are s.d. **These results show that the intraparticle catalytic communication distance x_0^{intra} and temporal memory t_0^{intra} have no clear dependence on this fluorescence intensity threshold.** It is worth noting that with increasing threshold value, the number of selected fluorescence bursts decreased, giving lower apparent turnover rate for each nanocatalyst; this is expected, however, as higher threshold value would miss events that have relatively lower fluorescence intensities.

5.12. Both intraparticle and interparticle catalytic communications are independent of the laser light power density, supporting that laser excitation and thus surface plasmon resonance of Au play insignificant roles.

The Au nanorods and nanoplates are both plasmonic particles, and their localized surface plasmon resonances (LSPR)[10,43-49] overlap with the wavelength of the laser (532 nm) that we used to induce the fluorescence of the catalytic product resorufin. To probe whether LSPR excitation would play any role in the observed intraparticle and interparticle catalytic communications, we examined their dependence on the power density of the laser light, using Au nanorods as the representative system.

In our experiments, the 532 laser beam was used to illuminate a ~50×100 μm^2 area via TIR geometry. Because of the Gaussian laser beam shape, there was a natural dispersion of the light power density across the illumination area: highest at the center and lower toward the periphery. And the local light power density at any location could be easily obtained from the laser illumination spatial profile and the total laser power illuminating the sample. As a result, individual Au nanorods experience different laser power density depending on their locations within the illumination area. We thus sorted individual Au nanorods into groups of similar local light power densities. As a control, we first examined whether their catalytic activity, normalized by their length, would depend on the light power density using the sorted individual nanorods. For both the deacetylation reaction and the deoxygenation reaction, the catalytic activities (i.e., reaction rates) of individual nanorods are essentially independent of local light power density within experimental error (Figure 5.23a, f). *This*

independence indicates that within our experimental laser power density range (~0.05 to 0.4 kW/cm^2), the laser excitation, and thus LSPR excitation, has insignificant contributions to the observed catalytic reactions, consistent with our previous findings[50] .

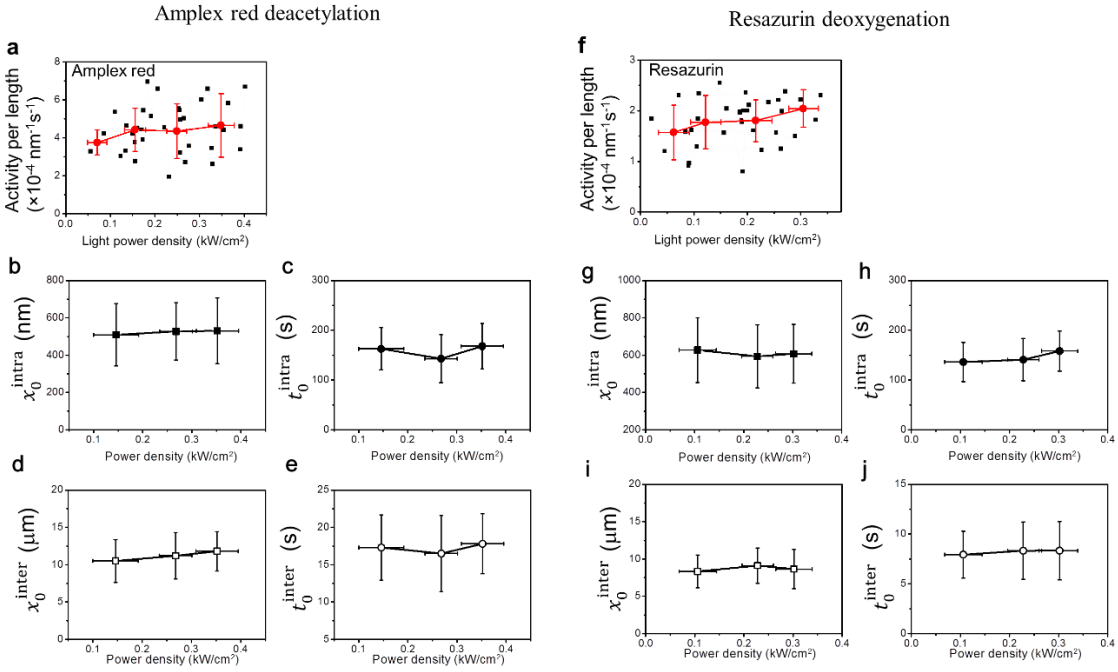

Figure 5.23. Both intraparticle and interparticle catalytic communications of Au nanorods are independent of the laser light power density, supporting that laser excitation and thus surface plasmon resonance of Au play insignificant roles. (**a, f**) Catalytic activity of individual Au nanorods, normalized by the nanorod length, vs. the local 532 nm light power density in catalyzing the AR deacetylation (**a**) and Rz deoxygenation (**f**). Each black square represents a single nanorod; the red squares are average values after sorting the nanorods into groups of similar local light power density. Error bars are s.e.m. (**b-e, g-j**) Intraparticle and interparticle catalytic communication distance x_0 and temporal memory time t_0 of Au nanorods vs. the local 532 nm light power density in catalyzing the AR deacetylation reaction (b-e) and the Rz deoxygenation reaction (**g-j**).

We then examined the intraparticle and interparticle catalytic communications within each group of individual Au nanorods of similar light power density, and determined

their catalytic communication distance x_0 and the temporal memory t_0. For both the deacetylation reaction and the deoxygenation reaction and for both intraparticle and interparticle catalytic communications, the determined x_0 and t_0 show no significant dependences on the local light power density (Figure 5.23b-e and g-j). *These independences indicate that the laser light plays no significant roles in the observed catalytic communications; they also support that LSPR, which could be excited by the laser light, does not play any significant roles, either*.

5.13. Applying voltage across the reactor cell using two Cu or Pt electrodes results in a steady-state electrical current, and they also cause similar changes in intra- and interparticle catalytic communication distances.

We used a two-electrode configuration potentiostat to apply a voltage ranging from −1.2 to 1.2 V across the microfluidic reactor of 5-8 mm in width in the *xy* imaging plane perpendicular to the solution flow direction (Figure 5.3c). The electrodes (made of copper foil or platinum wire) were connected to the working and counter electrodes of the potentiostat. Here the voltage direction being orthogonal to the solution flow minimized the cross-influence between the electric field effect and the solution flow effect.

Upon applying the voltage using Cu electrodes, an electrical current can be detected, and it reaches a steady state after ~800 seconds (Figure 5.3a). The steady-state current increases when the voltage magnitude increases, and the current changes direction when the voltage bias is flipped (Figure 5.3a-b). This steady-state electrical current has contributions from both the charging current and some redox processes on the electrode. The charging

current comes from the fact that the microfluidic reactor is under continuous flow of the reactant solution, containing >100 mM electrolytes (e.g., phosphate buffer), giving its nonequilibrium state, and is indicated by that the steady-state current increases with increasing solution flow rate (Figure 5.3c). The redox contribution is indicated by color changes of the Cu electrodes over a period of time (i.e., Cu electrode is likely oxidized) and visible formation of gas bubbles (possibly H_2 and O_2 formation from water electrolysis).

Using two Pt electrodes, similar behaviors were observed, although the steady-state electrical currents are smaller than those from Cu electrodes at the same voltages (Figure 5.3d-e). The smaller currents here are likely due to much less redox contribution to the current, as Pt electrodes are inert and we did not observe visually significant formations of gas bubbles. The cosine function amplitudes $\Delta x_{0,\mathrm{EF}}^{\mathrm{intra}}$ using Pt electrodes are smaller (Figure 5.3f-g), likely due to smaller steady-state electrical current.

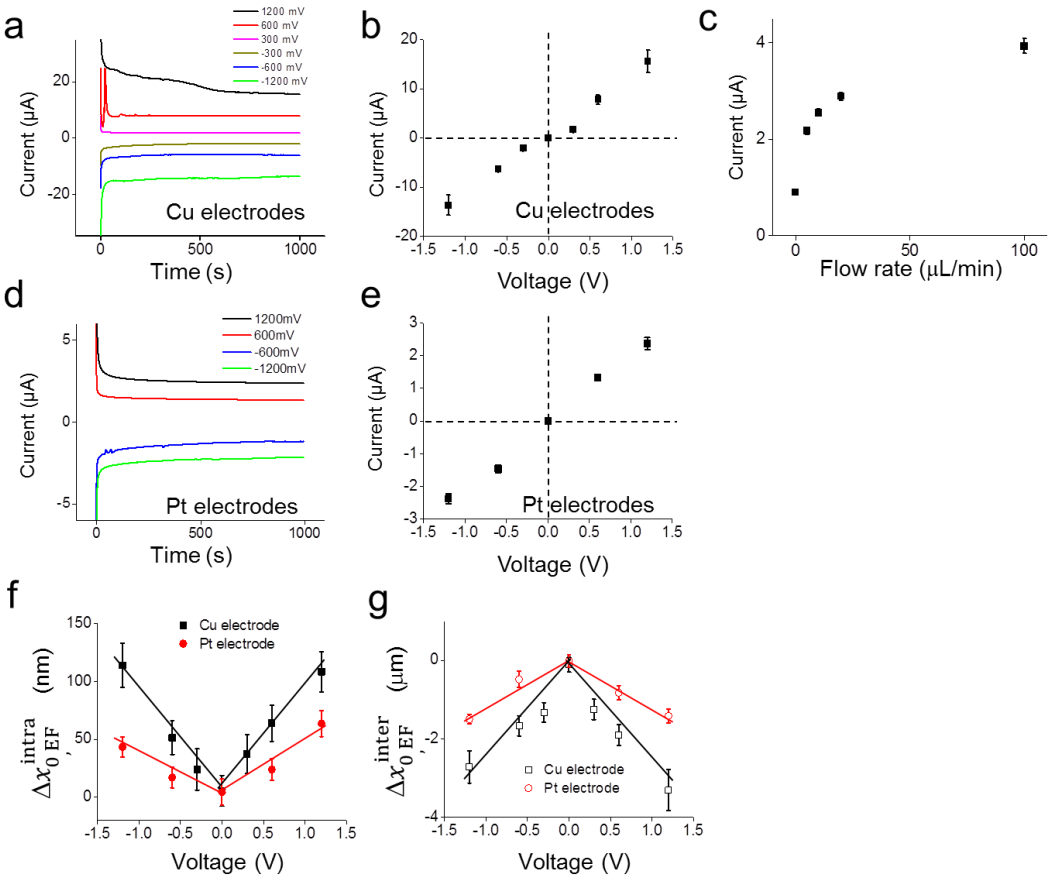

Figure 5.24. Applying voltage using two metal electrodes results in a steady-state electrical current across the microfluidic reactor cell: (**a**) Electrical current vs. time upon applying voltages at $t = 0$ using two Cu electrodes at a flow rate = 10 μL/min. (**b**) The steady-state current vs. applied voltage from **a**. (**c**) The steady-state current using two Cu electrodes vs. solution flow rate at a voltage of 0.3 V. (**d-e**) Same as **a** and **b** but using two Pt electrodes. (**f-g**) **Using Cu or Pt electrodes results in similar changes in intra- and inter-particle catalytic communication distances** (e.g., for Au-nanorod-catalyzed Rz deoxygenation): Cosine function amplitude $\Delta x_{0,\mathrm{EF}}^{\mathrm{intra}}$ vs. voltage from voltage manipulations of intra- (**f**) and inter-particle (**g**) catalytic communication distance of Au nanorods in catalyzing Rz deoxygenation, using Cu or Pt electrodes. Lines: all linear eye-guide. The data using Cu electrodes are the same as presented in Figure 5.15e and Figure 5.16h.

5.14. Acetate and nitrite promote the reaction rates of Au-particle-catalyzed AR deacetylation and Rz deoxygenation, respectively, whereas resorufin does not

5.14.1. Ensemble reaction kinetics shows that the reaction product acetate and nitrite can promote the Au-particle-catalyzed reaction rates of AR deacetylation and Rz deoxygenation, respectively, whereas the product resorufin does not

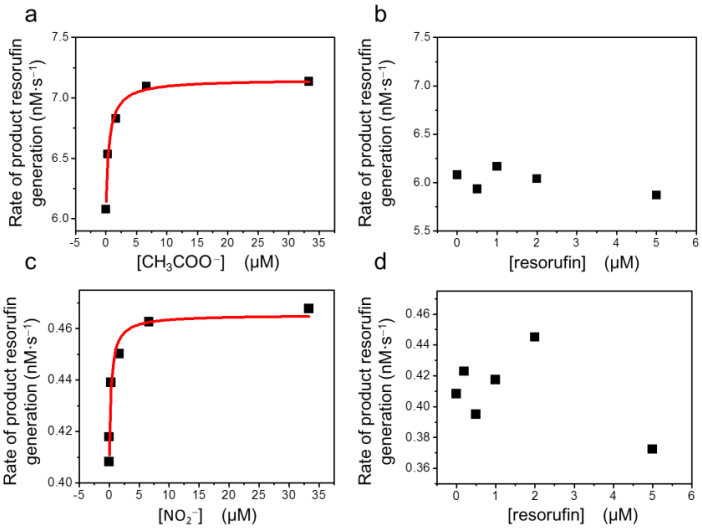

Figure 5.25. Dependence of initial catalytic reaction rates on the presence of externally added reaction products measured at the ensemble level. 5 nm Au particles (PELCO® NanoXact™) were used as representative Au nanocatalysts here because of their size homogeneity compared with Au nanorod and nanoplate samples, which are heterogeneous and contain many different shapes of particles (Figure 5.1f-i). (**a, b**) Initial rate of resorufin generation in AR deacetylation as a function of initial acetate (**a**) or resorufin (**b**) concentration in the solution. **The data show that acetate can promote the rate of Au-particle-catalyzed AR deacetylation — with increasing acetate concentration, the initial reaction rate increases and eventually saturates — whereas resorufin cannot, as its presence does not affect the initial reaction rate.** Reaction condition: 3 μM amplex

red, 100 mM H_2O_2, 50 nM 5 nm Au nanoparticles, and variable potassium acetate or resorufin in 100 mM pH 7.1 phosphate buffer. Panel **a** is also presented as Figure 5.5g in the main text. (**c, d**) Initial rate of resorufin generation in Rz deoxygenation as a function of initial nitrite (**c**) or resorufin (**d**) concentration in the solution. **The data show that nitrite can promote the rate of Au-particle-catalyzed Rz deoxygenation, whereas resorufin cannot.** Reaction condition: 20 μM resazurin, 10 mM NH_2OH, 200 nM Au nanoparticles, and variable nitrite or resorufin in 100 mM pH 7.1 phosphate buffer. Panel **c** is also presented as Figure 5.16i. Red lines in **a** and **c** are fits with saturation rate Eq. 5.2, where $K_{1/2}$ is the half saturation concentration of the promoter. For acetate, $K_{1/2} = 0.95 \pm 0.15$ μM; for nitrite, $K_{1/2}$ is 0.46 ± 0.14 μM. The apparent promoting effects of acetate and nitrite on the respective reactions are not strong, as the catalytic reaction rates only increase by up to 20%. It remains to be determined how mechanistically acetate or nitrite can have apparent promoting effects on the catalytic rate on the Au particle surfaces. One possibility is that acetate or nitrite can adsorb near the surface active sites, forming some interactions with the surface adsorbed reactant molecules and thus stabilizing the transition state, leading to catalytic rate enhancement. Other mechanisms may operate as well.

5.14.2. Single-particle catalytic kinetics of Au nanorods also shows that acetate and nitrite can promote the catalytic rates of AR deacetylation and Rz deoxygenation, respectively.

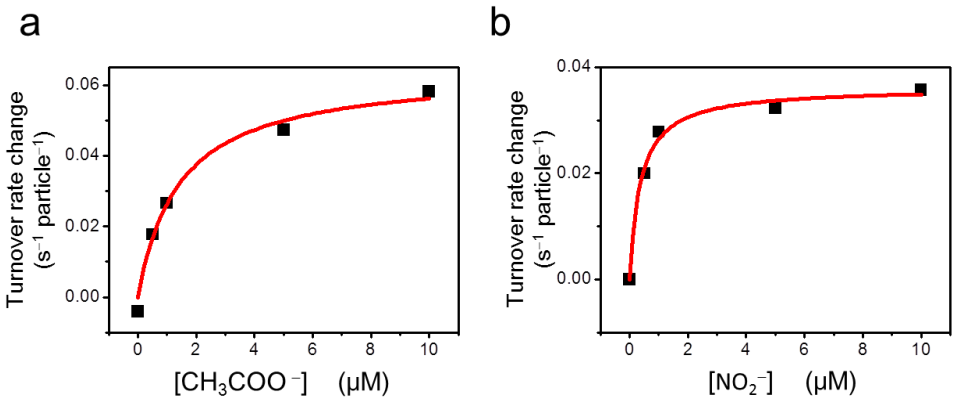

Figure 5.26. Changes of single-particle catalytic turnover rate on the presence of externally added acetate in the AR deacetylation reaction (a) or the presence of added nitrite in the Rz deoxygenation reaction (b) catalyzed by mSiO$_2$-coated Au nanorods measured through single-molecule fluorescence imaging. The data are averaged over > 40 nanorods, which were monitored over several hours while the acetate or nitrite concentrations were increased step-wise. During the experimental time, the catalysts also deactivated appreciably; this deactivation effect over time was corrected for by using pre-determined deactivation rates, which were measured by monitoring the time-dependent catalytic activity of individual particles without changing reaction condition. AR reaction condition: 0.2 μM AR, 60 mM H_2O_2, and various acetate concentrations, in 100 mM pH 7.1 phosphate buffer. Rz reaction condition: 0.2 μM Rz, 10 mM NH_2OH, various concentrations of NO_2^-, in 100 mM pH 7.1 phosphate buffer. Red lines are fits with the saturation equation Eq. 5.2. with $K_{1/2}$ (acetate) = 1.1 ± 0.3 μM; $K_{1/2}$ (nitrite) = 0.47 ± 0.09 μM. **The results further support that acetate and nitrite can act as promoters of the respective surface catalytic reactions on the Au nanorods, because the single-molecule fluorescence imaging specifically detect reaction products on individual nanorods.**

5.15. Other possible mechanisms of intraparticle catalytic communication and the many rationales against them.

5.15.1. Reaction heat dissipation should not be the mechanism

Another potential mechanism for intraparticle catalytic communication is the dissipation of heat generated in the catalytic reactions. But this mechanism would not involve the movement of charged species, and thus should *not* be the operating mechanism. We here discuss additional arguments against this possibility.

In this mechanism, the reaction heat could dissipate from one site to affect reactions at surrounding sites. From standard formation enthalpies, both the deacetylation of amplex red and the deoxygenation of resazurin are estimated to be exothermic reactions ($\Delta_r H°$ = –471.6 kJ mol^{-1} and –399.8 kJ mol^{-1}, respectively; see below for the details for the estimations; since we do not know for sure all the reaction products of the disproportionation reaction, we do not treat it here).

To probe if this heat dissipation could be relevant, we simulated the spatial and temporal profile of temperature on a nanorod using the 1-D thermal diffusion equation[51]:

$$\frac{\partial T}{\partial t} = \alpha \frac{\partial^2 T}{\partial x^2} = \frac{k}{\rho c_p} \frac{\partial^2 T}{\partial x^2} \qquad \text{Eq. 5.10}$$

where α is the thermal diffusivity of the material, k is its thermal conductivity, ρ is its density, and c_p is its specific heat (Table 5.1). Just for illustration, we assumed that a single reaction at one site would cause a local temperature jump (ΔT) of 5 K in a 100-nm-long segment on a 20-nm-diameter nanorod. The minimum energy (ΔE) needed to cause such a temperature jump is:

$$\Delta E = c_p \rho V \Delta T \qquad \text{Eq. 5.11}$$

where V is the volume of the material the heat is released on. For a 20-nm diameter 100-nm long cylinder made of gold, ΔE would be about 3.9×10^{-16} J, which is equivalent to the amount of heat released for about ~820 $H_2(g)$ molecules to react with $O_2(g)$ to form $H_2O(l)$, a highly exothermic reaction ($\Delta H°$ is –286 kJ mol^{-1} for the reaction $H_2(g) + {}^1/_2O_2(g) = H_2O(l)$)[41]. This amount of heat is clearly much higher than that is possibly released from a single reaction of deacetylation of amplex red or deoxygenation of resazurin studied here. Therefore, a 5 K temperature jump represents a highly over-estimated case.

Using the thermal diffusion equation (Eq. 5.10), we simulated the time-dependent temperature profile along one dimension (i.e., along the length of a nanorod) after a local 5 K temperature jump above room temperature (293 K). With thermal parameters for gold (Table 5.1), the simulation shows that within about 1 ns, the initial temperature gradient from the local temperature jump is already dissipated, i.e., no significant temperature gradient is present along the length of nanorod (Figure 5.27a). As our Au nanorods are coated with mesoporous silica and our experiments were done in an aqueous solution, we further did simulations using the thermal parameters for silica and water. The simulations show that for both these cases, the initial temperature gradient disappears in a time scale shorter than 1 μs because of heat dissipation (Figure 5.27b and c). These timescales for heat dissipation are orders of magnitude faster than the temporal memory (10^1 to 10^2 of seconds) of the intraparticle catalytic communications of Au nanorods and nanoplates. We thus further conclude that reaction heat dissipation is likely not the reason for the long-range intraparticle catalytic communication within single Au nanocatalysts.

Table 5.1. Parameters for Heat Dissipation Simulations*

Materials	Thermal Conductivity k (W m^{-1} K^{-1})	Density ρ (kg m^{-3})	Specific Heat c_p (J kg^{-1} K^{-1})
Water	0.58	1000	4.18×10^3
Silica	1.3	2648	703
Gold	310	19.30×10^3	0.129×10^3

* all from reference[41]

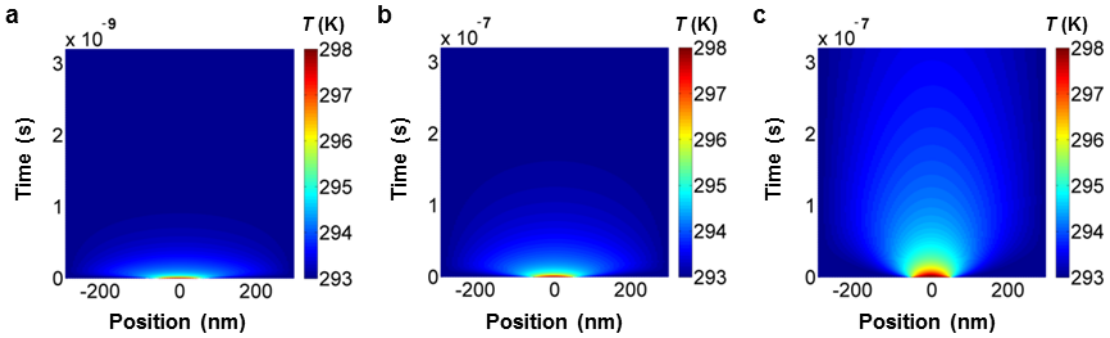

Figure 5.27. Simulations of time-dependent 1-dimensional temperature profile after a local 5 K temperature jump at position 0, using thermal parameters for (**a**) gold, (**b**) silica, and (**c**) water. Parameters are listed in Table 5.1.

We used the standard formation enthalpies to estimate the reaction enthalpies for the deacetylation reaction of AR and the deoxygenation reaction of Rz, according to the following balanced chemical equations (see also Figure 4.1b in the Chapter 3):

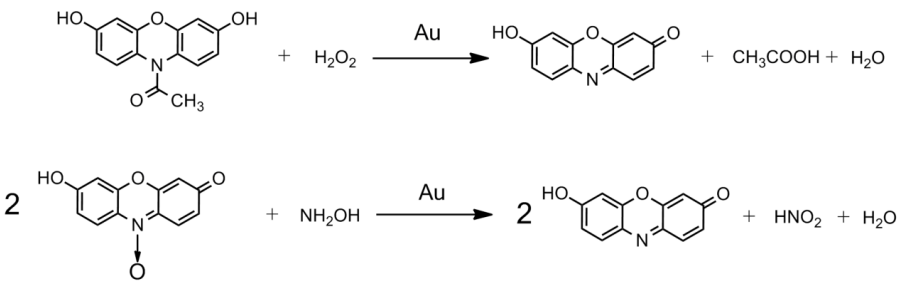

We used all neutral species in the above equations, rather than ions, as approximations. The

standard formation enthalpies of the following species are taken from the CRC Handbook of Chemistry and Physics: NH_2OH (s), −114.2 kJ mol^{-1}; HNO_2 (*l*), −174.1 kJ mol^{-1}; H_2O_2 (*l*), −187.8 kJ mol^{-1}; CH_3COOH (*l*), −484.3 kJ mol^{-1}; H_2O (*l*), −285.8 kJ mol^{-1}.

The standard formation enthalpies for resazurin, resorufin, and amplex red are not available. Using the standard formation enthalpies of the gaseous atoms of C (716.7 kJ mol^{-1}), N (472.7 kJ mol^{-1}), O (249.2 kJ mol^{-1}), and H (218.0 kJ mol^{-1}), and the mean bond dissociation energies for C=C (612 kJ mol^{-1}), C–C (348 kJ mol^{-1}), C–H (412 kJ mol^{-1}), C–O (360 kJ mol^{-1}), C=O (743 kJ mol^{-1}), N–O (157 kJ mol^{-1}), N–C (305 kJ mol^{-1}), N=C (613 kJ mol^{-1}), and O–H (463 kJ mol^{-1}) bonds[52], we estimated the standard formation enthalpies to be: resazurin, 448.9 kJ mol^{-1}; resorufin, 174.7 kJ mol^{-1}; amplex red, 61.3 kJ mol^{-1}; all corresponding to their gaseous states. Using these known and estimated standard formation enthalpies, the estimated standard reaction enthalpies are $\Delta_r H°$ = –471.6 kJ mol^{-1} and −399.8 kJ mol^{-1}, for the deacetylation reaction of amplex red and the deoxygenation reaction of resazurin, respectively.

5.15.2. Surface restructuring dynamics should not be the mechanism

Nanoparticles, once their size is small enough, can have dynamic surface restructuring[53-55]. For colloidal Au and Pt nanoparticles of about 4–14 nm in diameter, the timescale of this dynamic restructuring is about tens to hundreds of seconds, with larger nanoparticles having slower restructuring[14,17,56]. This restructuring can be cooperative across a nanoparticle's surface[53-55,57], which could result in some correlation between reactions occurring at different locations on the same nanoparticle. Nevertheless, this restructuring is likely not the reason for the intraparticle catalytic communications observed here for the Pd

and Au nanocatalysts, which are much larger and whose surfaces are further stabilized by the mesoporous silica shell. The restructuring timescale for these nanorods and nanoplates would be much longer than hundreds of seconds, thus too different from the temporal memory (10^1 to 10^2 seconds) of their intraparticle catalytic communications. Moreover, this structural dynamics should not have a directional dependence on an external electric field and would not behave like being mediated by positively-charged species.

In Section 4.16.3 below, we present additional evidences that the Au surface structure of Au nanorods are likely stable over the timescale of hours, further supporting that surface restructuring dynamics should not be the mechanism.

5.15.3. Surface plasmon resonance of Au should not be the mechanism

The $mSiO_2$-coated Au_2 nanorods and nanoplates we studied here are both plasmonic particles, and their localized surface plasmon resonances (LSPR)[10,43-49] overlap with the wavelength of the laser (532 nm) that we used to induce the fluorescence of the catalytic product resorufin. In Section 5.12 earlier, we showed that the intraparticle catalytic communication distances and temporal memories of Au nanorods are essentially independent of laser power density in both catalytic reactions (Figure 5.23b-c and g-h). This independence supports that laser light, as well as LSPR, plays no significant roles in the observed catalytic communications.

5.16. Further discussions on the hole migration mechanism for intraparticle catalytic communication

5.16.1. Effective diffusion coefficient of hole migration for intraparticle catalytic communication

Our electric field dependence experiments showed that the intraparticle catalytic communications in Pd- and Au-based nanocatalysts all involve a movable positively-charged species, which we propose to be a surface localized hole (i.e., positive charge) that is generated during catalysis and that can hop diffusively on the surface of the nanocatalysts to affect reactions nearby, leading to intraparticle catalytic communication. The "localized" nature of this hole here could come from interactions with the $mSiO_2$ shell and that the Pd or Au surface might contain Pd_xO_y or Au_xO_y (i.e., not purely metallic palladium or gold) due to redox reactions in an aerobic environment. This type of hole migration can be over a long distance, depending on the conductivity of the materials and the presence of charge traps[58-60], and such charges can be long-lived[61], consistent with the long communication distance and temporal memory of our observed intraparticle catalytic communication. This hole migration mechanism is also related to the model proposed by Tachikawa et al. in accounting for the remote photoluminescence behavior on single semiconductor TiO_2 nanowires [62].

Using the intraparticle catalytic communication distances and temporal memories observed experimentally, we can compute the effective diffusion coefficients D_1 and D_2 for 1-D and 2-D diffusions, respectively, for the hole migration along the length of Pd and Au nanorods and across the top facet of Au nanoplates:

$$D_1 = \left\langle x^2 \right\rangle / 2t \qquad \text{Eq. 5.12}$$

$$D_2 = \left\langle x^2 \right\rangle / 4t \qquad \text{Eq. 5.13}$$

Here the communication distance x_0^{intra} is used for *x*, and communication temporal memory t_0^{intra} is used for *t*. The calculated D_1 and D_2 are *all* about 1×10^{-15} m^2 s^{-1} (Table 5.2). The similarity of the effective diffusion coefficients among two different metals, three different nanocatalysts, and three distinct reactions supports that they share a common mechanism for the intraparticle catalytic communications. These effective diffusion coefficients here are small compared with those for carrier migration in semiconductor nanostructures (10^{-10} to 10^{-7} m^2 s^{-1})[63,64]. Therefore, these holes are dominantly localized, trapped charges with low mobility.

Table 5.2. Parameters for the observed intraparticle and interparticle catalytic communications[*]

		Pd nanorods	Au nanorods		Au nanoplates
		Rz disproportion.	AR deacetyl.	Rz deoxygen.	Rz deoxygen.
Intra-particle	x_0^{intra} (nm)	225 ± 20 (242 ± 56) [b]	516 ± 160 (531 ± 175)	624 ± 180 (657 ± 139)	130 ± 22
	t_0^{intra} (s)	27.5 ± 2.4 (29.8 ± 9.4)	128 ± 32 (136 ± 41)	168 ± 36 (165 ± 32)	5.5 ± 0.7
	D_{eff} ($\times 10^{-15}$ m^2 s^{-1})	0.92 ± 0.08 (0.87 ± 0.22)	1.1 ± 0.4 (1.04 ± 0.37)	1.2 ± 0.4 (1.31 ± 0.29)	0.77 ± 0.17
	Amplitude	0.056 ± 0.002, 0.043 ± 0.002 [c] (0.041 ± 0.003)	0.049 ± 0.007, 0.053 ± 0.008 (0.062 ± 0.010)	0.213 ± 0.045, 0.183 ± 0.068 (0.237 ± 0.094)	0.078 ± 0.006, 0.081 ± 0.007
	Charge of messenger	positive	positive	positive	n/d

Inter-particle	x_0^{inter} (μm)	n/a	10.5 ± 3.3	9.3 ± 2.4	11.5 ± 0.7
	t_0^{inter} (s)	n/a	18.1 ± 3.8	7.7 ± 1.4	6.2 ± 0.6
	Amplitude	n/a	0.421 ± 0.003	0.037 ± 0.002	0.18 ± 0.06
	Charge of messenger	n/a	negative (CH_3COO^-)	negative (NO_2^-)	n/d
	$K_{1/2}$ of x_0^{inter} quenching by anion (μM)	n/a	0.99 ± 0.14	0.53 ± 0.12	n/d
	$K_{1/2}$ of activity promotion by anion (μM)	n/a	0.95 ± 0.15	0.46 ± 0.14	n/d
	Residual correlation	0.034 ± 0.006, 0.031 ± 0.007 [c]	0.032 ± 0.005, 0.034 ± 0.009	0.030 ± 0.004, 0.030 ± 0.008	0.081 ± 0.008, 0.080 ± 0.009

[*] Results are overall averages taking into account of all experiments, including solution flow manipulations, voltage manipulations, reactant concentration variations, and various batches of nanocatalyst samples. [b] Values in parentheses are from 2-D analysis of ρ_{τ_i,τ_j} as a function of both Δx_{ij} and $\overline{\Delta t_{ij}}$ as in Section 4.17. [c] Two sets of values here are from the exponential fits of one dimensional analyses of ρ_{τ_i,τ_j} vs. Δx and vs. $\overline{\Delta t_{ij}}$, respectively, as in Figure 4.2a and b (red).

5.16.2. The positively-charged species should not be conduction band charges

The positively charge species that mediate intraparticle catalytic communication have low mobility, as shown above, and thus should be dominantly localized, trapped hole. Therefore, these holes cannot be conduction band charges of the metal nanocatalyst, which would travel fast within the nanocatalyst and thus would not decay significantly over

intraparticle distance separations.

5.16.3. Hole migration likely occurs via hole hopping, rather than atom migration

The migration of the proposed surface localized hole should occur through hole hopping, but another possibility is through atom migration. The latter would involve a positively-charged surface atom (e.g., $Pd^{\delta+}$ oρ $Au^{\delta+}$) moving around on the surface, and it would need to move hundreds of nanometers (i.e., the intraparticle catalytic communication distance) over a period of 10^1 to 10^2 seconds (i.e., the intraparticle catalytic communication temporal memory). Here we provide evidence against this atom migration possibility.

In our previous study of Au nanorods in catalyzing the AR deacetylation[2], we showed that along the length of individual Au nanorods there exists an activity gradient: the center of the nanorod has the highest activity, which decays linearly toward the two ends, giving rise to a volcano activity profile along the length (Figure 5.28). This activity gradient is attributable to an underlying surface defect density gradient, which is formed during the seeded crystal growth of these 1-dimensional nanocrystals[2]. Here we further examined the time dependence of this activity gradient over the course of catalytic reactions. Figure 5.28 shows that the activity gradient along the length of individual Au nanorods persists over a period of 3 hours, indicating that the underlying surface defect density gradient is stable. Therefore, the mobility of the surface Au atoms is insignificant over the timescale of hours, much longer than the observed temporal memory of intraparticle catalytic communications. This stability is also consistent with our discussions on the timescale of surface restructuring in Section 5.15.2, which should be very slow in these mSiO_2-coated Au nanorods. Atom migration is thus likely not the physical process for the proposed charge migration.

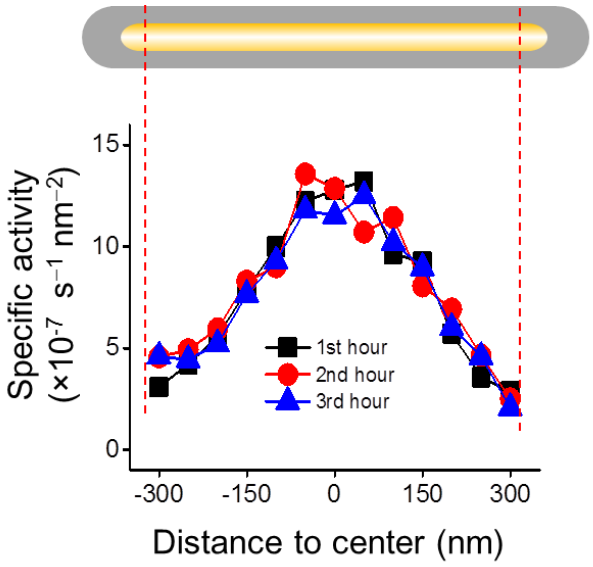

Figure 5.28. Specific activity along the length of individual $mSiO_2$-coated Au nanorods in catalyzing AR deacetylation during the 1st, 2nd, and 3rd hour of catalysis. The two ends of the nanorod are excluded in the analysis. Data are averaged over ~20 nanorods, all >400 nm in length to show the general trends. The specific activity shows linear gradients from the center toward the two ends, attributable to the underlying gradient of surface defect densities along the length, as we previously showed[2].

5.16.4. Proton is likely not the intra-particle catalytic messenger

Proton is positively charged and exists in aqueous solution. But proton is likely not the intra-particle catalytic messenger for the following reasons:

(1) Both the disproportionation reaction and the deacetylation reaction do not produce proton as a reaction product (Figure 4.1b, upper and middle), but the intra-particle catalytic communication involving a positively-charged species occur in these two catalytic reactions.

(2) The deoxygenation reaction may produce proton (Figure 4.1b, lower), but all reactions were done in buffered slightly basic solutions.

(3) If proton diffusion were to be the intraparticle communication mechanism on the surface of Pd-/Au- nanocatalysts within the $mSiO_2$ shell, proton, owing to its small size and mediation of H-bonds in water, should be able to diffuse out of the $mSiO_2$ shell and cause inter-particle communications, which, however, in mediated by a negatively-charged product species.

(4) Proton mobility μ_q in water at room temperature is ~3.62×10^{-3} cm^2 V^{-1} s^{-1},[65] corresponding to a diffusion coefficient D of 9.29×10^{-9} m^2 s^{-1}. Proton diffusion coefficient on a membrane was measured to vary between 1.5×10^{-8} m^2 s^{-1} and 2×10^{-7} m^2 s^{-1}.[66,67] And proton diffusion coefficient in silica hydrogel is ~2×10^{-8} m^2 s^{-1}.[68] All these are orders of magnitude larger than the effective diffusion coefficient of the intraparticle catalytic messenger at ~1×10^{-15} m^2 s^{-1} (Table 5.2).

5.16.5. Possible reasons for the non-operation of the molecular diffusion mechanism involving negatively-charged products for intra-particle catalytic communication

It is interesting to note that the molecular diffusion mechanism of negatively-charged products for the interparticle catalytic communications in Au-based nanocatalysts is not operative for intra-particle communication, even though one would normally expect that these products (i.e., acetate and nitrite), if they could diffuse between particles, should be able to diffuse within the particles. We conjecture that this is perhaps because the mesopores of the $mSiO_2$ shell are aligned radially (they were formed by base etching from outside), as suggested in the literature[69]. This conjecture is also supported by tracking the motion of the fluorescent product resorufin, which does not diffuse laterally on the nanocatalysts before desorbing and disappearing into the solution (Figure 5.5b).

5.16.6. Strength of catalytic communication

Regardless whether the underlying mechanism is due to a migrating hole (as for intraparticle cases) or a diffusing molecule (as for interparticle cases), these observed catalytic communications are not strong, as reflected by the small amplitudes of the decay profiles of ρ_{τ_i,τ_j}. The strength of this communication, i.e., amplitude of correlation, is expected to be dependent on a number of factors. For one, the catalytic messenger generated from one site has many possible places to migrate to. For another, the strength would depend on the promotion effect by the catalytic messenger on the reaction kinetics, and for the interparticle cases, the kinetic promotion even at saturation is merely ~15% (Figure 4.5g and Figure 5.25a and c).

5.17. 2-D analysis of ρ_{τ_i,τ_j} as a function of both Δx_{ij} and $\overline{\Delta t_{ij}}$ using a diffusive model for intraparticle catalytic communication

5.17.1. Formulation of 2-D diffusion model analysis

Assuming the motion of the catalytic messenger follows a diffusive model, we can formulate quantitatively the correlation coefficient ρ_{τ_i,τ_j} as a function of both distance separation Δx_{ij} and time delay $\overline{\Delta t_{ij}}$, utilizing the probability density function $P_t(x)$ of displacement length x for a specified diffusion time t and the probability density function $Q_x(t)$ of diffusion time t for a specified displacement length x.

In one-dimensional Brownian motion, the probability density function $P_t(x)$ of displacement length x (a scalar) for a specified diffusion time t is:

$$P_t(x) = \frac{1}{\sqrt{\pi D t}} \exp\left(-\frac{x^2}{4Dt}\right) \qquad \text{Eq. 5.14}$$

where D is the 1-dimensional diffusion constant. Experimentally, we observed that the correlation coefficient ρ_{τ_i,τ_j} (or ρ, to be simpler in writing) follows an exponential decay behavior with increasing time delay $\overline{\Delta t_{ij}}$ (or t, to be simpler in writing) between temporally subsequent reactions:

$$\rho(t;x) = A \cdot \exp\left(-\frac{t}{t_0}\right) + c \qquad \text{Eq. 5.15}$$

Here x could be any value from 0 to ∞ at any given time t; t_0 is the memory time of the catalytic communication; A the correlation amplitude, and c is a residual spurious correlation. If x is constrained to a certain distance away, i.e., $x \in (x_1, x_2)$, the probability of the catalytic messenger to reach that distance range needs to be considered and this probability is $\int_{x_1}^{x_2} P_t(x)\mathrm{d}x$. Under this constraint, the correlation coefficient needs to be modified as:

$$\rho(t; x \in (x_1, x_2)) = A\exp\left(-\frac{t}{t_0}\right)\int_{x_1}^{x_2} P_t(x)\mathrm{d}x + c = A\exp\left(-\frac{t}{t_0}\right)\left[\mathrm{Erf}\left(\frac{x_2}{\sqrt{4Dt}}\right) - \mathrm{Erf}\left(\frac{x_1}{\sqrt{4Dt}}\right)\right] + c \qquad \text{Eq. 5.16}$$

When $x_1 = 0$ and $x_2 = \infty$, i.e., without constraining x, the above equation returns to Eq. 5.15 above. Eq. 5.16 is used to fit data such as Figure 4.2b in Chapter 3.

For one-dimensional Brownian motion, the probability density function $Q_x(t)$ of diffusion time t for a specified displacement length x needs to be derived. From the probability density function $P_t(x)$, we can first deduce the probability $F(l,t)$ of

displacement length in the range from 0 to l at time t:

$$F(l,t) = \int_0^l P_t(x)\mathrm{d}x = \int_0^l \frac{1}{\sqrt{\pi Dt}} \exp\left(-\frac{x^2}{4Dt}\right)\mathrm{d}x = \mathrm{Erf}\left(\frac{l}{\sqrt{4Dt}}\right) \qquad \text{Eq. 5.17}$$

$F(l,t)$ is essentially the survival probability that the diffusing molecule is still within a distance l from the origin at time t. Let $Q_l(t)$ be the probability density function of diffusion time t to reach a certain distance (i.e., displacement length) l, $Q_l(t)\Delta t$ is then the probability for the diffusing molecule to be at the distance l away between t and $t + \Delta t$, which is equal to $F(l,t) - F(l,t+\Delta t)$, the difference in survival probability between t and $t + \Delta t$ at the distance l. Therefore,

$$Q_l(t) \cdot \Delta t = F(l,t) - F(l,t+\Delta t) \qquad \text{Eq. 5.18}$$

And thus,

$$Q_l(t) = -\frac{\partial}{\partial t} F(l,t) = -\frac{\partial}{\partial t} \mathrm{Erf}\left(\frac{l}{\sqrt{4Dt}}\right) = \frac{l}{\sqrt{4\pi Dt^3}} \exp\left(-\frac{l^2}{4Dt}\right) \qquad \text{Eq. 5.19}$$

Replacing the variable l by x, we have:

$$Q_x(t) = \frac{x}{\sqrt{4\pi Dt^3}} \exp\left(-\frac{x^2}{4Dt}\right) \qquad \text{Eq. 5.20}$$

Experimentally, we observed that the correlation coefficient ρ_{τ_i,τ_j} (or ρ, to be simpler in writing) follows an exponential decay behavior with increasing distance separation Δx (or x, to be simpler in writing) where the temporally subsequent reactions occur:

$$\rho(x;t) = A \cdot \exp\left(-\frac{x}{x_0}\right) + c \qquad \text{Eq. 5.21}$$

Here t could be any value from 0 to ∞ at any given distance separation x; x_0 is the

communication distance of the catalytic communication; A the correlation amplitude, and c is a residual spurious correlation. If t is constrained to a certain time range, i.e., $t \in (t_1, t_2)$, the probability of the catalytic messenger to spend this specific range of time diffusing needs to be considered and this probability is $\int_{t_1}^{t_2} Q_x(t)\mathrm{d}t$. Under this constraint, the correlation coefficient needs to be modified as:

$$\rho(x; t \in (t_1, t_2)) = A \cdot \exp(-\frac{x}{x_0}) \cdot \int_{t_1}^{t_2} Q_x(t)\mathrm{d}t + c = A \cdot \exp(-\frac{x}{x_0}) \cdot [\mathrm{Erf}(\frac{x}{\sqrt{4Dt_1}}) - \mathrm{Erf}(\frac{x}{\sqrt{4Dt_2}})] + c \qquad \text{Eq. 5.22}$$

When $t_1 = 0$ and $t_2 = \infty$, i.e., without constraining t, the above equation returns to Eq. 5.21 above. Eq. 5.22 is used to fit data as in Figure 4.2a in the Chapter 3.

5.17.2. Delayed maxima are not expected to be observable for inter-particle catalytic communications.

Both Eq. 5.16 and Eq. 5.22 predict a delayed maxima as a function of x or t, as we observed for the intraparticle catalytic communications (e.g., Figure 5.2a, b; green lines). These behaviors are not observed, and **are not expected to be observed, for the *inter*particle catalytic communications** because the messenger product molecules spend most of their diffusion times in the $mSiO_2$ shell, but most of their diffusion distances are in the solution; Section 5.10.5).

REFERENCES

1 Huang, X. & Zheng, N. One-pot, high-yield synthesis of 5-fold twinned pd nanowires and nanorods. *J. Am. Chem. Soc.* **131**, 4602–4603 (2009).

2 Zhou, X. *et al.* Quantitative super-resolution imaging uncovers reactivity patterns on single nanocatalysts. *Nat. Nanotechnol.* **7**, 237–241 (2012).

3 Botella, P., Corma, A. & Navarro, M. T. Single gold nanoparticles encapsulated in monodispersed regular spheres of mesostructured silica produced by pseudomorphic transformation. *Chemistry of Materials* **19**, 1979-1983 (2007).

4 Kundu, S. & Ravishankar, N. Rapid synthesis of hybrids and hollow pdo nanostructures by controlled in situ dissolution of a zno nanorod template: Insights into the formation mechanism and thermal stability. *Nanoscale* **8**, 1462-1469 (2016).

5 Jana, N. R., Gearheart, L. & Murphy, C. J. Wet chemical synthesis of high aspect ratio cylindrical gold nanorods. *J. Phys. Chem. B* **105**, 4065-4067 (2001).

6 Wang, Z. L., Mohamed, M. B., Link, S. & El-Sayed, M. A. Crystallographic facets and shapes of gold nanorods of different aspect ratios. *Surf. Sci.* **440**, L809-L814 (1999).

7 Johnson, C. J. *et al.* Growth and form of gold nanorods prepared by seed-mediated, surfactant-directed synthesis. *J. Mater. Chem.* **12**, 1765-1770 (2002).

8 Carbó-Argibay, E. *et al.* The crystalline structure of gold nanorods revisited: Evidence for higher-index lateral facets. *Angewandte Chemie (International ed. in English) FIELD Publication Date:2004* **49**, 9397-9400 (2010).

9 Katz-Boon, H. *et al.* Three-dimensional morphology and crystallography of gold nanorods. *Nano Lett.* **11**, 273–278 (2011).

10 Pérez-Juste, J., Pastoriza-Santos, I., Liz-Marzán, L. M. & Mulvaney, P. Gold nanorods:

Synthesis, characterization and applications. *Coord. Chem. Rev.* **249**, 1870-1901 (2005).

11 Gai, P. L. & Harmer, M. A. Surface atomic defect structures and growth of gold nanorods. *Nano Lett.* **2**, 771-774 (2002).

12 Andoy, N. M. *et al.* Single-molecule catalysis mapping quantifies site-specific activity and uncovers radial activity gradient on single 2d nanocrystals. *J. Am. Chem. Soc.* **135**, 1845–1852 (2013).

13 Shankar, S. S. *et al.* Biological synthesis of triangular gold nanoprisms. *Nature Mater.* **3**, 482-488 (2004).

14 Xu, W., Kong, J. S., Yeh, Y.-T. E. & Chen, P. Single-molecule nanocatalysis reveals heterogeneous reaction pathways and catalytic dynamics. *Nat. Mater.* **7**, 992-996 (2008).

15 Bueno, C. *et al.* The excited-state interaction of resazurin and resorufin with amines in aqueous solutions. Photophysics and photochemical reactions. *Photochem Photobiol* **76**, 385-390 (2002).

16 Balcerzyk, A. & Baldacchino, G. Implementation of laser induced fluorescence in a pulse radiolysis experiment--a new way to analyze resazurin-like reduction mechanisms. *Analyst* **139**, 1707-1712 (2014).

17 Han, K. S., Liu, G., Zhou, X., Medina, R. E. & Chen, P. How does a single pt nanocatalyst behave in two different reactions? A single-molecule study. *Nano Lett.* **12**, 1253-1259 (2012).

18 Miranda, K. M., Espey, M. G. & Wink, D. A. A rapid, simple spectrophotometric method for simultaneous detection of nitrate and nitrite. *Nitric Oxide* **5**, 62-71 (2001).

19 Beckwith, R., Cooper, J. & Margerum, D. Kinetics and mechanism of the oxidation of hydroxylamine by aqueous bromine. *Inorganic Chemistry* **33**, 5144-5150 (1994).

20 Tachikawa, T., Yonezawa, T. & Majima, T. Super-resolution mapping of reactive sites on titania-based nanoparticles with water-soluble fluorogenic probes. *ACS Nano* **7**, 263–275 (2012).

21 Roeffaers, M. B. J. *et al.* Super-resolution reactivity mapping of nanostructured catalyst

particles. *Angewandte Chemie (International ed. in English) FIELD Publication Date:2004* **48**, 9285-9289 (2009).

22 Zhang, Y. *et al.* Superresolution fluorescence mapping of single-nanoparticle catalysts reveals spatiotemporal variations in surface reactivity. *Proceedings of the National Academy of Sciences* **112**, 8959–8964 (2015).

23 Decan, M. R., Impellizzeri, S., Marin, M. L. & Scaiano, J. C. Copper nanoparticle heterogeneous catalytic 'click' cycloaddition confirmed by single-molecule spectroscopy. *Nat Commun* **5**, 4612 (2014).

24 Renault, C. *et al.* Observation of nanometer-sized electro-active defects in insulating layers by fluorescence microscopy and electrochemistry. *Anal Chem* **87**, 5730-5737 (2015).

25 Skaug, M. J., Mabry, J. & Schwartz, D. K. Intermittent molecular hopping at the solid-liquid interface. *Phys Rev Lett* **110**, 256101 (2013).

26 Cordes, T. & Blum, S. A. Opportunities and challenges in single-molecule and single-particle fluorescence microscopy for mechanistic studies of chemical reactions. *Nat Chem* **5**, 993-999 (2013).

27 Ha, J. W. *et al.* Super-resolution mapping of photogenerated electron and hole separation in single metal-semiconductor nanocatalysts. *J Am Chem Soc* **136**, 1398–1408 (2014).

28 Lu, H. P., Xun, L. & Xie, X. S. Single-molecule enzymatic dynamics. *Science* **282**, 1877-1882 (1998).

29 Betzig, E. *et al.* Imaging intracellular fluorescent proteins at nanometer resolution. *Science* **313**, 1642-1645 (2006).

30 Rust, M. J., Bates, M. & Zhuang, X. Sub-diffraction-limit imaging by stochastic optical reconstruction microscopy (storm). *Nature Meth.* **3**, 793-796 (2006).

31 Hess, S. T., Girirajan, T. P. K. & Mason, M. D. Ultra-high resolution imaging by fluorescence photoactivation localization microscopy. *Biophys. J.* **91**, 4258-4272 (2006).

32 Bates, M., Huang, B., Dempsey, G. T. & Zhuang, X. Multicolor super-resolution imaging with photo-switchable fluorescent probes. *Science* **317**, 1749-1753 (2007).

33 Shroff, H., Galbraith, C. G., Galbraith, J. A. & Betzig, E. Live-cell photoactivated localization microscopy of nanoscale adhesion dynamics. *Nature Methods* **5**, 417-423 (2008).

34 Lin, H. *et al.* Mapping of surface-enhanced fluorescence on metal nanoparticles using super-resolution photoactivation localization microscopy. *ChemPhysChem* **13**, 973-981 (2012).

35 Blythe, K. L., Titus, E. J. & Willets, K. A. Comparing the accuracy of reconstructed image size in super-resolution imaging of fluorophore-labeled gold nanorods using different fit models. *Journal of Physical Chemistry C* **119**, 19333-19343 (2015).

36 Wertz, E., Isaacoff, B. P., Flynn, J. D. & Biteen, J. S. Single-molecule super-resolution microscopy reveals how light couples to a plasmonic nanoantenna on the nanometer scale. *Nano Letters* **15**, 2662-2670 (2015).

37 Zhou, X., Choudhary, E., Andoy, N. M., Zou, N. & Chen, P. Scalable parallel screening of catalyst activity at the single-particle level and sub-diffraction resolution. *ACS Catal.* **3**, 1448-1453 (2013).

38 Thompson, R. E., Larson, D. R. & Webb, W. W. Precise nanometer localization analysis for individual fluorescent probes. *Biophys. J.* **82**, 2775-2783 (2002).

39 Yildiz, A. *et al.* Myosin v walks hand-over-hand: Single fluorophore imaging with 1.5-nm localization. *Science* **300**, 2061-2065 (2003).

40 Xu, W. *et al.* Single-molecule electrocatalysis by single-walled carbon nanotubes. *Nano Lett.* **9**, 3968–3973 (2009).

41 Lide, D. R. (CRC Press, Inc., Boca Raton, 1995).

42 Zhou, X. *et al.* Quantitative super-resolution imaging uncovers reactivity patterns on single nanocatalysts. *Nat Nano* **7**, 237-241 (2012).

43 Murphy, C. J. *et al.* Gold nanorod crystal growth: From seed-mediated synthesis to

nanoscale sculpting. *Curr. Opin. Coll. Interf. Sci.* **16**, 128-134 (2011).

44 Thomas, K. G., Barazzouk, S., Ipe, B. I., Joseph, S. T. S. & Kamat, P. V. Uniaxial plasmon coupling through longitudinal self-assembly of gold nanorods. *J. Phys. Chem. B* **108** (2004).

45 Shao, Y., Jin, Y. & Dong, S. Synthesis of gold nanoplates by aspartate reduction of gold chloride. *Chem. Comm.*, 1104–1105 (2004).

46 Tsuji, M., Hashimoto, M., Nishizawa, Y. & Tsuji, T. Preparation of gold nanoplates by a microwave-polyol method. *Chem. Lett.* **32**, 1114-1115 (2003).

47 Ah, C. S. *et al.* Size-controlled synthesis of machinable single crystalline gold nanoplates. *Chem. Mater.* **17**, 5558-5561 (2005).

48 Chu, H.-C., Kuo, C.-H. & Huang, M. H. Thermal aqueous solution approach for the synthesis of triangular and hexagonal gold nanoplates with three different size ranges. *Inorg. Chem.* **45**, 808-813 (2006).

49 Liu, B., Xie, J., Lee, J. Y., Ting, Y. P. & Chen, J. P. Optimization of high-yield biological synthesis of single-crystalline gold nanoplates. *J. Phys. Chem. B* **109**, 15256-15263 (2005).

50 Xu, W., Kong, J. S., Yeh, Y.-T. E. & Chen, P. Single-molecule nanocatalysis reveals heterogeneous reaction pathways and catalytic dynamics. *Nat Mater* **7**, 992-996 (2008).

51 Firoozabadi, A., Ghorayeb, K. & Shukla, K. Theoretical model of thermal diffusion factors in multicomponent mixtures. *AIChE Journal* **46**, 892-900 (2000).

52 Atkins, P. & de Paula, J. *Atkins' physical chemistry*. 8th edn, (W. H. Freeman and Company, 2006).

53 King, D. A. & Woodruff, D. P. *Phase transitions and adsorbate restructuring at metal surfaces*. (Elsevier Science, 1994).

54 Tao, F. *et al.* Reaction-driven restructuring of rh-pd and pt-pd core-shell nanoparticles. *Science* **322**, 932-934 (2008).

55 Newton, M. A. Dynamic adsorbate/reaction induced structural change of supported metal

nanoparticles: Heterogeneous catalysis and beyond. *Chem. Soc. Rev.* **37**, 2644-2657 (2008).

56 Zhou, X., Xu, W., Liu, G., Panda, D. & Chen, P. Size dependent catalytic activity and dynamics of gold nanoparticles at the single-molecule level. *J. Am. Chem. Soc.* **132**, 138-146 (2010).

57 Ochoa-Daza, M. A., Zhou, X., Chen, P. & Loring, R. F. Interpreting single turnover catalysis measurements with constrained mean dwell times. *J. Chem. Phys.* **135**, 174509 (2011).

58 Chernyak, L., Osinsky, A., Fuflyigin, V. & Schubert, E. F. Electron beam-induced increase of electron diffusion length in p-type gan and algan/gan superlattices. *Appl. Phys. Lett.* **77**, 875-877 (2000).

59 Gonzalez-Vazquez, J. P., Anta, J. A. & Bisquert, J. Determination of the electron diffusion length in dye-sensitized solar cells by random walk simulation: Compensation effects and voltage dependence. *J. Phys. Chem. C* **114** 8552-8558 (2010).

60 Bian, Z., Tachikawa, T., Kim, W., Choi, W. & Majima, T. Superior electron transport and photocatalytic abilities of metal-nanoparticle-loaded tio2 superstructures. *J. Phys. Chem. C* **116**, 25444–25453 (2012).

61 Jennings, J. R. & Peter, L. M. A reappraisal of the electron diffusion length in solid-state dye-sensitized solar cells. *J. Phys. Chem. C* **111**, 16100-16104 (2007).

62 Tachikawa, T. & Majima, T. Exploring the spatial distribution and transport behavior of charge carriers in a single titania nanowire. *J. Am. Chem. Soc.* **131**, 8485–8495 (2009).

63 He, C., Zhao, L., Zheng, Z. & Lu, F. Determination of electron diffusion coefficient and lifetime in dye-sensitized solar cells by electrochemical impedance spectroscopy at high fermi level conditions. *J. Phys. Chem. C* **112**, 18730-18733 (2008).

64 van de Lagemaat, J., Zhu, K., Benkstein, K. D. & Frank, A. J. Temporal evolution of the electron diffusion coefficient in electrolyte-filled mesoporous nanocrystalline tio_2 films. *Inorg. Chim. Acta* **361**, 620-626 (2008).

65 Agmon, N. *et al.* Protons and hydroxide ions in aqueous systems. *Chem Rev* **116**, 7642-7672

(2016).

66 Gabriel, B., Prats, M. & Teissie, J. Lateral proton conduction in mixed monolayers of phosphatidylethanolamine and cetyltrimethylammonium bromide. *Biochemistry* **30**, 9359-9364 (1991).

67 Teissie, J., Prats, M., Soucaille, P. & Tocanne, J. F. Evidence for conduction of protons along the interface between water and a polar lipid monolayer. *Proc Natl Acad Sci U S A* **82**, 3217-3221 (1985).

68 Baltacioğlu, H. & Balköse, D. Diffusion of protons in silica hydrogel. *Colloid and Polymer Science* **267**, 460-464 (1989).

69 Gorelikov, I. & Matsuura, N. Single-step coating of mesoporous silica on cetyltrimethyl ammonium bromide-capped nanoparticles. *Nano Lett* **8**, 369-373 (2008).